Fermilab FERMILAB-THESIS-1997-42

Copyright © 1997 by Daniel Patrick Cronin-Hennessy
All rights reserved

TESTS OF PERTURBATIVE QCD IN W + JETS EVENTS PRODUCED IN $\sqrt{s} = 1.8$ TEV $\overline{p}p$ COLLISIONS

by

Daniel Patrick Cronin-Hennessy

Department of Physics
Duke University

Date: _____

Approved:

_____
Thomas J. Phillips, Supervisor

_____

_____

_____

_____

Dissertation submitted in partial fulfillment of the
requirements for the degree of Doctor of Philosophy
in the Department of Physics
in the Graduate School of
Duke University

1997

ABSTRACT

(High Energy Physics)

TESTS OF PERTURBATIVE QCD IN W + JETS EVENTS PRODUCED IN $\sqrt{s} = 1.8$ TEV $\overline{p}p$ COLLISIONS

by

Daniel Patrick Cronin-Hennessy

Department of Physics
Duke University

Date: _____

Approved:

_____
Thomas J. Phillips, Supervisor

_____

_____

_____

_____

An abstract of a dissertation submitted in partial fulfillment of the requirements for the degree of Doctor of Philosophy in the Department of Physics in the Graduate School of Duke University

1997

Abstract

We have analysed 108 pb^{-1} of data from $\sqrt{s} = 1.8$ TeV $\overline{p}p$ collisions. The data were collected at the Collider Detector at Fermilab during the 1992-93 and 1994-95 runs. We have selected the W bosons in these data in order to test predictions of perturbative QCD. Standard model contributions to $W+$ jet events include top production, diboson production and direct single W boson production with associated hadronic jets. The largest contribution to the $W+$ jets is direct single W production. We isolated this contribution in order to measure the cross sections for direct single W boson production as a function of jet multiplicity, the jet energy spectra, and jet-jet correlations. The high luminosity during data collection has provided 51431 inclusive $W \rightarrow e\nu$ events which allow precision tests of perturbative QCD. The cross sections and hadronic jet properties predicted by perturbative QCD are compared to our data measurements. Leading order QCD calculations from VECBOS have been processed through the HERWIG fragmentation program and fully simulated with the CDF detector simulation program (QFL). HERWIG provides added gluon radiation which represent partial higher order corrections to the tree-level diagrams and we refer to this calculation as enhanced leading order. The theory calculation is sensitive to several scales: renormalization, factorization and the cut-off used for the fragmentation. We find that the theory predicts the main qualitative features of the data.

Lisa, your love, support, and wisdom have brought joy, success, and perspective to my accomplishment. Thank you.

Acknowledgements

A thesis in high energy particle particle physics is a product of many individuals and decades of work and progress. In acknowledging the direct contributions to this analysis I will inevitably leave out many individuals. I would like to thank all those who participated in the design and construction of the Fermilab accelerator and the Collider Detector at Fermilab (CDF). This analysis has also relied on previous CDF jet analyses and precision electroweak studies. These have provided much of the analysis groundwork and used here. Specifically, I have received many helpful hints and advice through participation in the electroweak, W mass and QCD groups.

More intimately connected to the analysis are my colleagues at Duke University. Their high quality and precision work has helped move the analysis to its conclusion. My advisor, Tom Phillips, has provided guidance throughout and has provided me with the greatest support when I needed it most. Al Goshaw's enthusiasm and patience are invaluable. Wolfgang Kowald is the quintessential skeptic, a trait which has demanded the best in our work presented in this thesis. Bill Robertson's door is always open and his answers to my questions always helpful. Pat Hoyt has always been supportive and provided perspective during my tenure as a graduate student. Thank you all.

On the frontlines with me were Susi Hauger and Jay Dittmann. My interaction with these two excellent physicists and friends has improved my work and made it even more enjoyable.

For as long as I can remember my family and my extended family have encouraged and supported my academic efforts in every way. Thanks mom for your love and support. Thanks Russell, Debi, Mary Alice and Aunt Alice for your help and advice over the years. My brothers and sisters are scattered about the U.S but still they are always here. Thanks Tommy, Davy, Gloria, Casey and Priscylla. Dad, a small part of your painful desire to know and understand has certainly found its way into me and continues to motivate my own pursuits.

Contents

Abstract **iv**

Acknowledgements **vi**

List of Figures **x**

List of Tables **xix**

Abbreviations and Symbols **xxii**

1 The Standard Model **1**

1.1 Motivation and Analysis Overview 1

1.2 The Constituents of Matter 4

1.3 The Fundamental Interactions 6

1.4 $W+$ Jet Production in $\overline{p}p$ Collisions 13

1.5 Chapter Summary 18

2 The Experiment **21**

2.1 Introduction 21

2.2 The Tevatron Collider 22

2.3 The Collider Detector at Fermilab 26

2.4 Chapter Summary 40

3 Identifying W Bosons and Counting Jets **41**

3.1 Introduction 41

3.2 Electron Selection 42

3.3 W Selection 48

3.4 Jet Selection 51

3.5 Chapter Summary 60

4 Backgrounds to $W \to e\nu + \geq n$ Jets **61**

4.1 Introduction 61

4.2 Top 63

4.3 QCD Backgrounds to $W + \geq n$ Jets 66

4.4 Single Boson Backgrounds 75

4.5 Jet Multiplicity Promotions 79

4.6 Chapter Summary 83

5 The Efficiency for Finding $W \to e\nu$ Events **84**

5.1 Introduction 84

5.2 Acceptance Calculation for $W + \geq n$ Jets 85

5.3 Electron-Jet Overlap Losses 90

5.4 ID Efficiency 92

5.5 Trigger Efficiency 95

5.6 Chapter Summary 95

6 Data Results **97**

6.1 Introduction 97

6.2 $W \to e\nu + \geq n$ Jet Cross Section Results 97

6.3 Determination of the Systematic and Statistical Errors 102

6.4 Comparison of W and Z Cross Sections 107

6.5 Chapter Summary 108

7 Comparison to Theory and Conclusions **111**

7.1 Introduction 111

7.2 Theory Implementation 111

7.3 Comparisons to Data 117

7.4 Conclusions 133

A Calculation of $P_{T\nu}$ **135**

A.1 Introduction 135

A.2 The Components of Missing Transverse Energy 136

A.3 Determination of the Unclustered-Energy Scale Factor 138

A.4 Summary and Conclusions 146

B The $\not\!\!E_t$ Modeling for Monte Carlo **153**

B.1 The $\not\!\!E_t$ Modeling 153

C The P_{TW} Correction for the 0 Jets Monte Carlo **162**

D List of Cross Section Systematics **164**

E CDF Author List **167**

Bibliography **173**

Biography **176**

List of Figures

1.1 leading order diagram of muon pair production from electron pair annihilation. The lines represent particle momenta and the vertices represent the coupling of the photon to the fermions. The coupling is proportional to the $\alpha^{1/2}$. The amplitude of the process is given from the square of the matrix element so that we say that the process is second order α (α^2). 9

1.2 The W boson coupling. The electron and neutrino are connected through the weak charged current, the W^- boson. 14

1.3 Decay of a W^- boson to the first generation of leptons. 14

1.4 Production of a W^- boson from the first generation of quarks. . . . 15

1.5 $W+$ 1 parton production. Four leading order diagrams representing the production of a W^+ boson from various initial state partons. a) quark and antiquark intial state b) quark and gluon initial state c) quark and antiquark initial state d) antiquark and gluon initial state. 16

2.1 Schematic of the Tevatron which shows the major elements used in accelerating protons and antiprotons. The Tevatron is actually the same diameter as the main ring but is shown as smaller in the diagram. 24

2.2 One quarter of the Collider Detector at Fermilab. The major detector elements are indicated. $B0$ (the center of the detector) is along the beam line to the far right. 27

2.3 VTX event display. The figure shows a reconstructed vertex in a W boson event. The left side shows the octants of two half modules with one offset in ϕ with respect to the other to achieve a stereo view. The beam line is perpendicular to the page for this figure. In the figure on the right the beam line is horizontal. We can see the track stubs in the VTX converging at a point along the beam line (a vertex). The vetrical direction has been expanded. 31

2.4 Transverse view of the CTC. The beam line is in the center and perpendicular to the page. The figure shows the wire hits due to charged particles ionizing the gas. The dotted box encloses a stiff (high momentum) electron track. This view is expanded in the side-box of the figure. In the expanded view we see the individual wires and wire layers of the CTC. For every hit on a wire there is a two-fold ambiguity in the direction to the charged particle. The ambiguity is resolved by matching segments across layers. 32

2.5 Map of the calorimetry coverage which shows the η-ϕ coverage of the separate calorimeters. The figure shows the sections from $\phi = 0°$ to $90°$ and η from 0.0 to 4.2 (East side). The small squares represent the tower segmentation of the calorimeters. 34

2.6 One wedge of the CEM. Shown are the basic components: lead-scintillator sandwich for absorbing and measuring electromagnetic energy, wavelength shifter and light guides to carry the output of the scintillator to the photomultipliers. The ten towers are numbered from 0 to 9 and each cover 0.11 units of η. The z axis in the figure indicates the direction of the proton beam. Local x ,tangent to the ϕ direction, is shown. The CES is embedded in the CEM where the maximum of an electron shower is expected to be. The CES (see figure below) measures the electron position in the x and z coordinates. 37

2.7 The Central Electromagnetic Strip chamber which provides a transverse profile of the electron's shower in the CEM. A CES module fits into one tower of the CEM and measures the electron's position in the x and z coordinates to within 2 mm (for electron of transverse energy 50 GeV). 38

2.8 Tower segmentation for one quarter of the forward EM calorimeter (FEM). The beam line (upper-left corner) is transverse to the page. Towers are 5° by 0.11 units of η. 39

3.1 Distributions of some of the quality variables which are used to isolate high E_T central electrons that result from W decay. The solid histograms show the variables before the cuts are applied. The dashed histograms show the variables after full electron selection. The variables plotted are the following: electron isolation (Iso), hadronic over electromagnetic energy (Had/EM), CTC and CES matching in *local* x (Δx) and along z (Δz), electron energy divided by electron momentum (E/P) and the vertex distribution (z_{vtx}). 50

3.2 The plot shows the E_T distribution for the the events stripped with a subset of the electron selection cuts, full electron selection and our final W sample which includes a missing transverse energy ($\not\!\!E_t$) of at least 30 GeV. 51

3.3 The plot shows the $\not\!\!E_t$ distribution for the inclusive electron sample. Noticeable is the W peak due to the escaped ν. 52

3.4 The left plot shows the electron E_T distribution for those events that pass the loose electron selection but fail tight electron cuts. The plot on the right is the electron E_T distribution for the events that pass the tight electron cuts but fail the $\not\!\!E_t$ cut or pass the Z cuts. 53

3.5 The upper plot shows the energy deposited into the calorimeter from a $W+$ 1 jet event. The electron is located at $\phi = 291$ and $\eta = 0.78$. The other tower cluster contains the jet's energy deposited in the electromagnetic calorimeter (dark shade) and the hadronic calorimeter (light shaded). The lower plot shows a view of the central tracking chamber. The beam line is perpendicular to the page. The track cluster associated with the calorimeter cluster is evident. The electron track is located in the dotted rectangle. A superimposed arrow indicates the direction of the missing transverse energy. 54

3.6 The E_T distribution for all jets in th W sample with a $E_T \geq 15\ GeV$. 58

4.1 Isolation vs $\not\!\!E_t$ for the QCD sample. The bottom plot shows the 3 regions (a,b,and c) which are used to calculate the QCD events in region d where W bosons dominate. The characteristic $\not\!\!E_t$ distribution of $W \rightarrow e\nu$ events is evident in the lego plot (top). The QCD events have a $\not\!\!E_t$ distribution that peaks near 0 in this plot. 69

4.2 The isolation of electron 1 versus isolation of electron 2 for events with at least two electrons. The events that show the inverse relation between electron isolations are events where the two electron clusters are closer than the cone used to define the isolation. We remove these events from the QCD sample because they do not contaminate the W sample. 71

4.3 A profile plot of isolation versus missing transverse energy. The vertical axis shows the average isolation for events with a particular $\not\!\!E_t$ (horizontal axis). The high missing energy events show the low isolation characteristic of W electrons but significant QCD contamination is evident up to our $\not\!\!E_t$ cut of 30 GeV. The isolation of the low missing energy events are not completely independent of missing energy. 72

4.4 The plots show the subsamples of events in the isolation-$\not\!\!E_t$ plane which are used to test the QCD calculation. The upper plot is the subsample of QCD events with low $\not\!\!E_t$ sample. The lower is the subsample with a poorly-isolated electron. Each sample is divided into 4 regions to allow a calculation of the events in region d which is compared to the number of events (N_d) observed in the region. These samples are chosen to be displaced from the W dominant region (indicated by empty box). . . 74

4.5 The η distribution of the second electron in a Monte Carlo simulation of $Z \rightarrow e^+e^-$events. The first electron is defined as the one that passes tight central electron cuts identical to the W selection. The solid line is the distribution for events which pass our Z removal cuts. We can see a loss of events near the η gaps in our detector. We have also plotted the η of the second electron (dashed) for events that fail our Z removal cuts and have a large $\not\!\!E_t$. The peaks in this distribution correlate with the dips of the other distribution. 77

5.1 Obliteration efficiency as calculated from W Monte Carlo (filled circles) and Z data (open circles). Statistical errors only. 92

6.1 $W + \geq n$ jets cross sections. The inclusive ($W+ \geq$0 jet) cross section is from a previous CDF measurement. 101

6.2 Cross section Systematics. 104

6.3 Statistical Errors. 106

6.4 The upper plot is the ratio of the statistical error to systematic error for our $W+$ jet cross sections. The $x-$axis is is the number of jets. The lower figure gives the percentage error for $W+$ jet cross sections. The shaded histogram represents the current analysis and the unshaded represents the same analysis with 20 times the events. The systematic uncertainties were held constant. 108

6.5 Comparison of $W \to e\nu$ and $Z \to e^+e^-$cross section vs jet multiplicity. The inset shows the ratio of the $W \to e\nu$ cross section to the $Z \to e^+e^-$cross section. The error bars represent statistical uncertainties only. 109

7.1 The variation of strong coupling (α_s,two-loop) with the renormalization scale. The value of α_s for the two renormalization scales that are used in the LO matrix element calculation are indicated by the arrows. 114

7.2 Contour plot of the deviation of the LO $W+$ 1 parton cross section as a function of the renormalization scale (horizontal axis) and the factorization scale(vertical axis). The vertical axis is the ratio of factorization to renormalization scale. The deviation is defined as the absolute value of the percentage difference from the cross section at $Q^2_{ren} = Q^2_{fac} = M_W$. The dotted line is cross section for $Q^2_{ren} = Q^2_{fac}$. The average value for our default choices for the renormalization scale are shown on this line. 115

7.3 Comparison of the parton P_T distributions for various $W+$ 1 parton VECBOS Monte Carlo samples. The plots shows (theory′-theory)/theory as a function of parton P_T. The default calculation uses $Q^2_{ren} = Q^2_{fac} = < P_t >^2$. This sample is compared to a sample derived from the high renormalization scale $Q^2_{ren} = M^2_W + P^2_{tW}$ (top), the high factorization scale $Q^2_{ren} = M^2_W + P^2_{tW}$ (middle) and an alternate pdf MRSA′ (bottom). 116

7.4 $W + \geq n$ jets cross sections compared to theory. The filled circles are the data measurements with the error bars representing the combined statistical and systematic uncertainties. The band indicates the variation of the predictions with the renormalization scale. The $W+ \geq 0$ jet prediction is from a born calculation of inclusive W production. . 119

7.5 The ratio of data to theory for the $W+ \geq$n jet cross sections. The horizontal axis is the jet multiplicity. The upper figure compares the ratio for a variation in the renormalization scale. The lower plot shows the results for a variation in the fragmentation scale. The $n=$ 4 point is unavailable for the lower fragmentation scale. 120

7.6 The upper plot shows data and theory comparisons for σ_n/σ_{n-1}. The band represents the variation with the renormalization scale. The error bars on the data represent the combined statistical and systematic uncertainty. The lower plot shows the ratio of data to theory of the quantity σ_n/σ_{n-1}. The horizontal axis for both plots is the jet multiplicity. 122

7.7 The plot compares the jet E_T distributions for the highest E_T jet found in W^+ events and W^- events. The vertical axis represents the fractional difference of events per bin of E_T. The samples are normalized in area to one another before a comparison is made. . . . 124

7.8 The plot compares the jet E_T distributions for the highest E_T jet found in W and Z events. The vertical axis represents the fractional difference of events per bin of E_T. The samples are normalized in area to one another before a comparison is made. 125

7.9 The jet E_T distribution for (a) the highest E_T jet in $W+\geq 1$ jet events, (b) the second highest E_T jet in $W+\geq 2$ jet events, (c) the third highest E_T jet in $W+\geq 3$ jet events, (d) the fourth highest E_T jet in $W+\geq 4$ jet events. The points represent the data and the curves represent the theory. The solid curve is for the lower renormalization scale and the dotted is for the higher renormalization scale. The curves were derived from fits to an analytic function that reproduced the theory well. . . 126

7.10 Comparison of jet E_T distributions between data and theory. The fractional difference ((data-theory)/theory) verses the E_T of the highest E_T jet in $W+\geq 1$ jet events (a) and second highest E_T jet in $W+\geq 2$ jet events (b). The theory is normalized to the data before comparison. 129

7.11 The fraction of $=1$ jet events in ≥ 1 jet events versus the E_T of the highest E_T jet. 130

7.12 E_T of highest E_T jet from HERWIG. The histogram shows the distribution with $Q^2_{frg}=M^2_W + P^2_{tW}$. To generate the points we ran with essentially no limit on the radiation ($Q^2_{frg} = 300^2$). 131

7.13 The plots on the left show the distributions for the invariant mass of the two highest E_T jets in $W+\geq 2$ jet events (top) and $W+\geq 3$ jet events (bottom). The plots on the right show the separation (ΔR_{jj}) in $\eta - \phi$ space for the two highest E_T jets in $W+\geq 2$ jet events (top) and $W+\geq 3$ jet events(bottom). $\Delta R_{jj} = (\Delta\phi^2 + \Delta\eta^2)^{1/2}$ 132

A.1 Shown above is a $Z \rightarrow e^+e^-$event. The length of a vector is proportional to the momentum. The bisector of the angle between the e^+e^- pair is labeled η. This axis is the projection axis for the determination of the unclustered-energy scale factor (K). The orthogonal direction is labeled ψ. 139

A.2 The upper plot shows the mean of the projection of the Z + recoil for different values of the unclustered-energy scale. The sample is balanced at a scale factor of 2.0. The lower plot shows the corresponding width for the upper plot (open circles) and the width of the projection along the orthogonal direction (ψ see figure A.1) 140

A.3 The average unclustered energy along the η direction versus the η component of the electrons(Z) in the event. The unclustered energy is corrected by a factor (2.0) determined from the components along the η direction. 141

A.4 The average unclustered energy along the ψ direction versus the ψ component of the electrons(Z) in the event. The unclustered energy is corrected by a factor (2.0) determined from the components along the η direction. 142

A.5 The average unclustered energy along the η direction versus the η component of the electrons(Z) in the event. The correction factor for the unclustered energy has been scaled by +/− 25% (upper plots) and +/− 50% (lower plots) 143

A.6 The average unclustered energy along the ψ direction versus the ψ component of the electrons(Z) in the event. The correction factor for the unclustered energy has been scaled by +/− 25% (upper plots) and +/− 50% (lower plots) 144

A.7 The scale factor determination for the Z Monte Carlo. The upper plot shows the mean of the projection of the Z + recoil for different values of the unclustered-energy scale. The lower plot shows the corresponding width for the upper plot (open circles) and the width of the projection along the orthogonal direction. 145

A.8 These plots are identical to figure A.7 except additional smearing was introduced into the Monte Carlo unclustered energy. 146

A.9 Shown above is the true neutrino transverse momentum distribution. The measured $\not{E}_t$ for the shaded bands in the region 20:25 (dashed histogram) and 40:45 (dotted histogram) GeV are shown on the same plot. The left side is the raw $\not{E}_t$ vector the right side is the corrected $\not{E}_t$ 147

A.10 Shown together are the true and measured (uncorrected $\not{E}_t$) neutrino transverse momentum distributions. The inset shows the average uncorrected $\not{E}_t$ for a given P_T of the neutrino. 148

A.11 Shown together are the true and measured (corrected $\not{E}_t$) neutrino transverse momentum distributions. The inset shows the average corrected $\not{E}_t$ for a given P_T of the neutrino. 149

A.12 The average corrected $\not{E}_t$ for a given P_T of the neutrino. The correction factor for the unclustered energy has been scaled by approximately $+/-$ 25% (upper plots) and $+/-$ 50% (lower plots). The crosses are for the default correction factor. 150

A.13 The correction factor for unclustered energy (crosses) versus the jet energy cut (GeV). The line ($\sim$ 1.6) indicates the correction factor which results from treating all non-electron energy as unclustered (no jets). Also shown is the average correction factor (diamonds) for jets at the energy of the jet cut. 151

A.14 The difference of true and measured neutrino transverse momentum for two different jet definitions ($\geq$ 10 and 20 GeV). The upper plot is for 0 jet events and the lower plot is for events with at least one jet. . 152

B.1 The left side of the figure shows the x component of energy for electrons (top), jets (2nd from top), and unclustered energy (third from top). The right side is the y component of energy. The bottom plot is the unclustered energy again but with the addition of energy from extra interactions which does not contaminate (significantly) the other two types of energy. The electron energy (data) was corrected for extra interactions which promoted a zero jet event to the 1 jet channel. . . 155

B.2 Plot showing the Z data divided into events with no extra class 12 vertex (left) and events with at least 1 extra class 12 vertex (right). . 156

B.3 Ignoring the energy in the second electron cluster we reconstruct the leg with the $\not\!\!E_t$ and first Z leg. The comparison is between Monte Carlo and data. The lower plot includes the simulation of extra-interaction energy in the Monte Carlo. 157

B.4 $\not\!\!E_t$ in Z events. The shaded histogram is Monte Carlo $\not\!\!E_t$ for Z events. The crosses are for actual Z data. The lower plots includes the simulation of energy from extra interactions in the Monte Carlo. The plots on the right are the same as the left-side plots but on a log scale. . . 158

B.5 The magnitude of the energy from interactions which occur in the same crossing as the W + jets event. The distribution was determined with our luminosity-weighted minimum-bias sample. 159

B.6 The percentage change in the fraction of events above a particular transverse energy for the reconstructed Z leg with and without extra-interaction energy. A negative value indicates a loss of efficiency due to the extra energy. 160

C.1 The W data P_T distribution compared to our Monte Carlo "pseudo-0 jet" sample. The upper plot is the measured distribution (after QFL) for the original Monte Carlo. The lower plot includes a correction to the Monte Carlo after unfolding the data. The data are the same in both. 163

List of Tables

0.1 List of abbreviations used in the analysis. xxii

1.1 Standard model quarks and leptons. 5

2.1 The abbreviations and names of the CDF elements. 28

3.1 List of quality cuts for $W \to e\nu$ selection. 49

3.2 Jet Multiplicities Associated with W Production 59

4.1 The branching fractions for final states from $t\bar{t}$ decay. The final states with 4 jets are contributed primarily from the decays listed in the upper right and lower left corners. 64

4.2 Results of top background calculation. The first column lists the number of $W+ \geq n$ jet events selected from the 42000 top events generated. The second column gives the expected contribution to our data samples from top pair production and decay. The first error is statistical and the second is the systematic which is the sum of the top mass uncertainty, the luminosity uncertainty, and the theoretical uncertainty on the top cross section. 66

4.3 Number of events and the ratio ($\frac{N_a}{N_b}$) for the two control samples used in the QCD background calculation. 72

4.4 Number of events with a poorly-isolated electron and high $\not\!\!E_t$ (region c) in the QCD sample. 73

4.5 Results for the tests of the QCD background calculation. The predicted number of events in region 4 and the observed number of events are compared. The first column lists the results for the low $\not\!\!E_t$ sample and the second column lists the results for the poor isolation sample. Both samples are essentially free of W contamination. 73

4.6 Final results for QCD background. The first column is the number of W events selected with at least n jets. The second column presents the expected contamination of the W sample from QCD background. Statistical and systematic errors are shown. 75

4.7 Expected background for $W \to \tau\nu$ and $Z \to e^+e^-$. Fractions are number of background over number of $W \to e\nu$ 79

4.8 The table shows the probabilities for obtaining a single jet, 2 jets, 3 jets and 4 jets from an extra interaction. The first column shows the number of events found with m jets in the minimum bias sample. We use the number of vertices (40117) found in the minimum-bias sample and the number of extra vertices (41188) found in the W sample to calculate the probabilities in the second column (equation 4.7). 81

4.9 Summary of backgrounds to single $W+ \geq$ jet samples. 83

5.1 The name and description of losses to the $W \to e\nu$ sample due to the selection criteria. 84

5.2 Number of events with n jets reconstructed from $W + n$ parton Monte Carlo 86

5.3 Number of events passing each acceptance cut for our 0 to 4 jets samples. 87

5.4 Z removal efficiency for W + jets 88

5.5 Acceptances for variations in renormalization scale and jet energy scale. 89

5.6 Geometric and kinematic acceptances for W + jets. The last column shows the total acceptance with the statistical error and the systematic error respectively. 89

5.7 Electron-Jet Separation Efficiency for W + jets 91

5.8 ID efficiency for electrons as a function of the number of jets. 94

5.9 Trigger efficiency for electrons as a function of the number of jets. . . 96

5.10 Summary of $W+$ jet efficiencies. 96

6.1 Candidates, total background, total W efficiency (exclusive), and the relative cross sections for the $W+$ jet samples. 99

6.2 $W+\ \geq n$ jet Cross Sections. The first error listed is the combined statistical error which includes the statistical error on the number of events and the statistical error on the efficiency and background calculations. The second error is a common systematic error of 4.8% from the input inclusive W cross section. The third error is the systematic which is dominated by jet counting systematics (see next section). For this table we list the maximum of the plus and minus systematic. The last error is the total error. 100

6.3 List of systematic errors for $W+$ jets analysis. 103

7.1 Enhanced LO $W+\ \geq n$ jet cross section predictions. The results are presented for n=1 to 4 with statistical errors shown. The determination of the cross section counted jets with a $E_T \geq 15.0\ GeV$ and an $|\eta_{det}| \leq 2.4$ after a full detector simulation of the jets had been performed. 117

B.1 Comparison of acceptances for $W+$ jets events with and without extra interactions. 161

Abbreviations and Symbols

Table 0.1: List of abbreviations used in the analysis.

Abbr	Full Name
CMX	Central Muon eXtension
CTC	Central Tracking Chamber
CMU	Central MUon
CDT	Central Drift Tube array
CMP	Central Muon uPgrade
CES	Central Electromagnetic Strip chamber
CEM	Central ElectroMagnetic
CHA	Central HAdronic
EW	electroweak
EM	electromagnetic
EI	extra interactions
FMU	Forward MUon
FEM	Forward ElectroMagnetic
FHA	Forward HAdronic
ID	identification
LO	Leading Order
NLO	Next-to Leading Order
PHA	Plug HAdronic
PEM	Plug ElectroMagnetic
QCD	quantum chromodynamics
QED	quantum electrodynamics
SVX	Silicon VerteX detector
UE	underlying event
VTX	VerTeX detector
WHA	Wall HAdronic
pdf	parton distribution functions
GeV	Giga-electron volts (10^9)
TeV	Tera-electron volts (10^{12})
fb	femtobarns (10^{-15} barns)
pb	picobarns (10^{-12} barns)
mb	milibarns (10^{-3} barns)

Chapter 1

The Standard Model

1.1 Motivation and Analysis Overview

One can view much of the history of physics as a search for a single theory capable of explaining and predicting all observed physical phenomena. One of the most ambitious lines of investigation is the challenge of explaining the fundamental structure of matter. The idea that matter is decomposable into fundamental units is a hypothesis that has persisted for at least 2000 years because it is a testable hypothesis which has successfully survived continual experimental scrutiny. Though this particle picture of matter has survived, it has not been without repeated overhaul and refinement. One of the most significant and recent advances in our understanding is that a particle description of the world is fundamentally incomplete. Such a description must be complemented by a wave description as well. The mathematical expression of this idea is found in quantum mechanics. It is believed to be a requirement of nature that any successful fundamental theory is necessarily a quantum mechanical theory. Our current most successful fundamental quantum theory is known as the standard model.

The standard model unambiguously defines the most fundamental constituent of matter and the forces which govern these constituents. To date, there are no known serious experimental results contradicting the predictions of this theory; though, there are fundamental reasons for believing that this theory is incomplete. Most notable is the standard model's silence on a quantum mechanical description of gravity. In order to advance our understanding of the physical universe and to refine the theories that mathematically express this understanding, we must test the standard model at the

limits of its predictions. One means of achieving this is to directly probe the structure of matter. A seemingly crude but effective method of probing particle structure is by smashing particles together. The power of this procedure is best understood in a particle's wave nature. The fundamental wavelength of a moving particle decreases as its momentum increases. In an analogy with light, the resolving power of the particle probe increases as the wavelength decreases. From these two relations, we see that high energy particle collisions can reveal the fine structure of matter.

A reasonable level of structure at which to begin a study is the proton. The Tevatron Collider at Fermilab accelerates and collides the proton with its antiparticle at the world's highest center of mass energies, 1.8 trillion electron-volts (TeV). In these collisions the constituents of the proton, quarks and gluons, can interact with constituents of the antiproton. It is these hard interactions which we utilize to test the standard model. Specifically, we search for a relatively rare product, the W boson particle, that is produced from the hard interactions.

Though the production of a W boson occurs in only 1 of every 2 million $\overline{p}p$ collisions, it is relatively easy to find. The W decays quickly to other particles and its decay characteristics are well described by the electroweak sector of the standard model. The W decays 10.8% of the time to a final state with an electron plus a neutrino [1]. Electrons leave a distinctive signature in the detector. Neutrinos, on the other hand, easily escape the detector without a trace. The elusive neutrino leaves the electron conspicuously unbalanced from the detector's perspective. This dual electron plus missing energy signature identifies W production.

The description of W boson production relies on a less well understood sector of the standard model, quantum chromodynamics or QCD for short. QCD describes the strong interaction between partons (quarks and gluons). Parton collisions which produce a W can simultaneously produce other partons in association with the boson.

It is actually these $W+$ parton events which interests us. We measure the rate of production (cross section) of the partons as a function of the number of partons that are produced. We also measure the kinematic properties of the partons produced in association with the W boson. These measurements are used to test the predictions for cross sections and kinematic properties as described by QCD.

Simply put, extracting predictions from QCD is difficult. The theorist must use the perturbative approach to approximate QCD predictions. In this scheme, successively more precise calculations are done which are referred to as orders of the calculation. The first order calculation is called leading order (LO) and the next order is curiously referred to as next-to leading order (NLO). The success of the perturbative approach depends on the process that one calculates. The production of the massive W boson requires a large momentum transfer and this requirement satisfies the conditions for the perturbative approximations to be accurate.

Beyond measuring $W+$ parton production characteristics, the reliability of the QCD calculations is assessed in this dissertation. Currently NLO calculations are available for $W+$ 1 parton production. We choose to test the LO calculations which are available for $W+$ 1 parton through $W+$ 4 parton production. This choice allows a more comprehensive treatment of the W data that we analyze.

The discussion above has been inaccurate in at least one respect. The standard model states that we can not observe partons! This is experimentally verified continuously to the frustration of the experimentalist. The parton quickly converts to multiple hadrons [1] through processes referred to as fragmentation and hadronization. The hadrons initiated by the parent-parton, share the parent's momentum and generally travel in a direction close to its initial direction. The experimental signature of this cone-like stream of hadrons is referred to as a jet. Our analysis will reconstruct

[1] strongly interacting composite particles

the jets deposited in the detector.

In the next section we will refine these concepts in a more detailed overview of the standard model. Since it has taken more than two millennia to move from the conception of the *atom* to the discovery of the 6 quarks and 6 leptons that currently represent the fundamental particles of nature, it is fitting that we relate a small portion of the evidence for the standard model.

1.2 The Constituents of Matter

The standard model specifies the most fundamental constituents of matter and describes the interactions among these. The fundamental particles, quarks and leptons, are spin 1/2 particles (fermions) from which all matter is composed. Leptons interact via the gravitational, electromagnetic, and weak forces. There are 6 fundamental leptons divided into three generations. The first generation contains the familar stable electron and its associated neutral lepton (ν_e). There exists two other versions of the electron: the muon (μ) and the tauon (τ). The μ and τ have almost identical quantum numbers as the electron but are distinguished by their greater masses and unique lepton quantum numbers. The μ with its associated neutrino (ν_μ) form the second generation of leptons and the τ and ν_τ form the third generation. The three generations of leptons are listed in table 1.1. The charged leptons (e,μ,τ) participate in gravitational, electromagnetic and weak interactions while the chargeless neutrinos interact via the weak and gravitational interactions.

Parallel to the leptons, there exists 6 quarks. These are distinguished by their flavor: up (u), down (d), strange (s), charm (c), bottom (b) and top (t). The quarks are fractionally charged fermions which are the constituent particles of all observed composite particles (hadrons). Stable matter consist of members from the first generation of quarks, up and down.

Table 1.1: Standard model quarks and leptons.

generation			charge
1	2	3	Q
	quarks		
up	charm	top	2/3
down	strange	bottom	-1/3
	leptons		
ν_e	ν_μ	ν_τ	0
e^-	μ^-	τ^-	-1

Until 1995 the existence of the 5 lightest quarks (u, d, s, c, b) had been experimentally verified. The discovery of the sixth quark awaited the design of a collider which could reach the threshold energy of top quark production. A recent success of the standard model is the verification of the top quark produced in pairs $(t\overline{t})$ at Fermilab [2]. The discovery was possible with the Tevatron because the center of mass energy of the $\overline{p}p$ collisions are well above twice the top quark mass. The top quarks fleeting existence prevents it from forming bound states with other quarks. The top decays to a W boson and b quark which provides a unique and clean detector signature for its identification and study. The top mass ($176.8 \pm 6.5\ GeV/c^2$ [3]) is now the most accurately known of all quark masses. However, this level of precision introduces some uncertainty into the $W+$ jet analysis as we shall see in chapter 4.

Quarks can interact through the same forces as leptons (G,EM,Weak). They also participate in the strong interaction which is the force responsible for combining quarks into hadrons. Quarks were first proposed as the building blocks of hadrons with the introduction of the static quark model. This model described the hadrons as bound states of three quarks (baryons) or a quark-antiquark pair (mesons). An example pertinent to the current analysis is the quark content of the proton which is a baryon consisting of 2 up quarks and 1 down quark (uud). Angular momentum

sum rules for spin 1/2 particles allow only half integer spin composite particles from 3-quark bound states and integer spin composite particles from 2 quark bound states. Thus, baryons are defined by their 1/2 integer spin and mesons by their integer spin. These two quark configurations successfully accounted for the hundreds of hadrons produced in decades of high energy experiments, but some fundamental problems existed in this model. The static quark model provided no explanation of the force which glued the quarks together to form hadrons. No bare quarks had been observed in any collisions. Finally, the quantum mechanical wave function for some of the hadrons necessarily violated a fundamental quantum mechanical principle. These problems are resolved within the current standard model and specifically they are explained within the QCD sector of the theory.

With the specification of the quarks, leptons, and their associated antiparticles, we complete the list of 24 fundamental fermions of the standard model. The hundreds of individual hadrons produced in high energy collisions are reducible to the 6 fundamental quarks and their antiparticles.

1.3 The Fundamental Interactions

All interactions of particles are believed to be specified by the four known forces of nature: gravity, electromagnetism, weak and strong. The standard model provides a description of the electromagnetic, weak and strong forces. The electromagnetic and weak interactions are often spoke of together as the electroweak interaction. They are related through their couplings in a manner parallel to the electric and magnetic forces. Here we discuss the interactions separately.

1.3.1 Gravity

The standard model does not provide a mathematically consistent integration of the force of gravity in its description of the world. Currently untenable problems of providing a quantum description of the gravitational force have not been resolved. However this failing of the standard model does not pose problems for experiments in particle physics because gravity is by far the weakest of the four interactions. Therefore, it is safely neglected in our examination of the other fundamental interactions.

1.3.2 Electromagnetism

The electromagnetic interaction is described within the context of the standard model and was the first of the four interactions to be described as a quantum mechanical gauge invariant field theory known as quantum electrodynamics (QED). Physically, gauge invariance is expressed by the conservation of a charge in interactions. For the electromagnetic interaction it is the electric charge (Q) which is conserved. All charged particles interact through the electromagnetic force with a strength that is determined by their charge. An example of an electromagnetic interaction is the annihilation of the electron (e^-) with its antiparticle the positron (e^+). The final state of this interaction is constrained by charge conservation and will consist of any charged particle pair such as a muon pair ($\mu^+\mu^-$).

The gauge invariance required of QED is actually more restrictive than global conservation of charge. The theory must provide a connection between charges disappearing in one place and appearing in another[4]. The mediators of the electromagnetic interaction are photons. This idea is expressed in the Feynman diagram of figure 1.1. We read this diagram as an electron pair annihilating to a photon with the subsequent muon pair creation from the photon. Feynman diagrams such as figure 1.1 permit a method of expressing the various orders of the perturbative ap-

proximations that are used to calculate measurable quantities such as cross sections and decay rates. The horizontal axis in the diagram represents time and the vertical axis is the spatial dimension. The legs of the diagram represent the momenta of the particles and the vertices represent the coupling to the photon. Figure 1.1 shows one intermediate photon. It is possible that other diagrams can be written containing more photons and still represent the same process. For example, we could draw the photon as splitting to any pair and re-combining before the muon pair is produced. The beauty of QED is that the probability of such occurrences decreases with the number of photons emitted and absorbed. This is due to the small coupling ($\alpha \approx 1/137$) between photons and charged particles. The best first approximation to $e^+e^- \rightarrow \gamma \rightarrow \mu + \mu^-$, is therefore given by the diagrams with the fewest intermediate photons.

The mathematical evaluation of diagram 1.1 yields the leading order QED approximation of $e^+e^- \rightarrow \gamma \rightarrow \mu + \mu^-$. The technical details of the diagrams evaluation are outside the scope of this thesis; however, some aspects of the calculation need mentioning. The exact value used for α depends on an energy scale introduced into the calculation which is called the *renormalization scale*. The variation (or running) of α with the renormalization scale introduces some uncertainty into the perturbative calculation because the choice of scale for a particular process is somewhat arbitrary. Fortunately, the dependence on the renormalization scale drops out as higher order diagrams are added to the calculation. QED calculations, which have been performed beyond leading order, have yielded precise calculations in excellent agreement with experimental measurements [5].

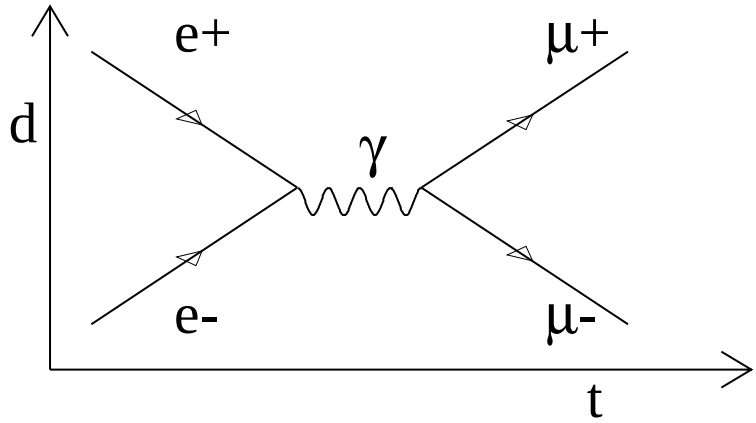

Figure 1.1: leading order diagram of muon pair production from electron pair annihilation. The lines represent particle momenta and the vertices represent the coupling of the photon to the fermions. The coupling is proportional to the $\alpha^{1/2}$. The amplitude of the process is given from the square of the matrix element so that we say that the process is second order α (α^2).

1.3.3 The Strong Interaction

The strong force binds the quarks into hadrons and its residual effects are responsible for binding the protons and neutrons into nuclei. Quantum chromodynamics (QCD) is the quantum field theory which describes the strong force. Parallel to QED, there is a conserved charge (color) and there are quanta which mediate the interaction. In contrast, the color charge is triple valued and there are an octet of mediators called gluons. The strong coupling (α_s) is relatively large, making perturbative QCD more difficult. Accurate perturbative QCD predictions are possible for processes involving large momentum transfers (small distance) because the coupling runs to small values as the momentum transfer increases.

An additional distinction from QED is that force mediators, gluons, carry color charge which means they can couple to one another. The gluon self-coupling leads to a linear form of the strong potential which increases as the distance increases. The linear behavior provides some intuition into the empirical fact that quarks have not been observed. The strong potential field energy grows linearly with the separation

of charges. As charges continue to separate it becomes energetically possible and favorable to create quark pairs from the field and reduce the charge separation. The quarks produced from this process must eventually form colorless, bound states. The only two stable colorless configurations of bound quark states are the 3-quark combination and the quark-antiquark bound state [6]. In a single stroke QCD provided 3 missing elements of the static quark model. QCD provided a binding force. This force provided the explanation why quarks remain hidden from observation. Finally, it provided a reason for the meson and baryon quark configurations.

The introduction of color also solved an apparent contradiction in the static quark model description of hadrons. This is most easily seen in the resonance Δ^{++} [7]. The quantum numbers of this particle are reproduced by 3 up quarks in the ground state ($l = 0$) with the spins aligned ($J = S = 3/2$). This configuration violates the Pauli exclusion principle because the interchange of any 2 of the three identical fermions yields the identical wave function. If each quark carries a different color then the wave function can be expressed in the required totally antisymmetric form.

It is interesting to note that some of the earliest experimental evidence supporting QCD was derived from the QED process described earlier (e^+e^- annihilation). QED calculations predict the production rate of quark pairs as easily as that of muon pairs. The only significant difference in the LO diagrams is that the quarks carry a fraction of the electric charge (e) so that their coupling to the photon is reduced. Aside from the quarks charge, the rate of quark pair production is determined by the number of final states available to the photon. Two factors determine the number of final states, one of which is the available energy to produce quarks with mass. Current e^+e^- colliders can run at energies well above twice the mass of all but the top quark. The second factor that increases the number of final states available to the photon is the color degree of freedom which will raise the production rate by three times.

Absolute measurements of the production rate are unnecessary since the rates can be compared to the rate of muon pair production which contains no color factor. The measurements agree with the inclusion of the color factor for quarks ([8]).

Since we can not directly observe bare quarks, the actual measurement of quark pair production involved analyzing $e^+e^- \rightarrow hadrons$. The detailed analysis of hadrons produced from e^+e^- annihilation provides more evidence in support of QCD. At high center of mass energies the hadrons are observed to cluster into 2 jets. This process is predicted by QCD and consistent with a parent-quark fragmenting to hadrons [9]. The tell-tale signs of quarks as progenitors of jets is due to the fact that the fragmentation of quarks is decoupled from the production of quarks. The basic idea is that quarks are produced, subsequently fragment to multiple partons and eventually collect into bound states (hadrons). We utilize these features in our $W+$ jet analysis. Since the hadronic final state carries the history (momentum) of its parent-parton, the jets that we reconstruct at the Collider Detector at Fermilab (CDF) can be corrected back to the original parton momentum.

The fragmentation of quarks poses more serious problems in the predictions of jets. The long-time-scale physics of fragmentation is in the realm of soft QCD. The calculations here are even more difficult than perturbative QCD which we use to predict the production of partons. Therefore, models of parton fragmentation are necessary.

The use of a fragmentation model introduces a second scale into our QCD predictions, the *fragmentation scale*. This scale sets an upper limit of particle radiation from the parent-parton that occurs during fragmentation. Although our $W+$ jet comparisons are insensitive to the micro-details of the fragmentation model, they are sensitive to the fragmentation scale. Since these models are currently our only theoretical connection between partons and jets, their reliability must be assessed.

1.3.4 The Weak Interaction

We have reserved the discussion of the weak interaction for last because of its central role in our analysis. As described earlier, we begin our analysis by identifying W bosons. The W boson is one of the mediators of the weak interaction. This boson couples upper generation members of fermions to the lower generation [2] members as shown in figure 1.2. In this diagram we see that the interaction involves a transfer of electric charge at the vertex. The weak interactions mediated by the W^- boson and its antiparticle (W^+) are referred to as the weak charged currents. There is also a weak neutral current mediated by the Z boson. The strength of the charged and neutral weak current couplings are related to the electron charge (e) by numerical factors. Additionally, the couplings of the Z boson are similar to that of the photon with the exception that the Z will also couple to neutrinos. These features hint at the electroweak unification mentioned earlier. Details of electroweak unification are found in references [11]. There is one prediction that arises from the unification of electromagnetic and weak forces that deserves mentioning. The theory predicts that the Z and W bosons will be massive. Furthermore, the theory predicts the values for the masses. The discovery of the Z and W bosons at their expected masses was another triumph for the standard model.

Observation of W Bosons

The $\overline{p}p$ collider that produced the first observed W bosons is located at CERN [12, 13]. A short diversion into the details of the discovery will serve to describe the techniques used to observe W bosons.

The identification of a W relies on the final state particles of its decay. One possible decay of the W^- is the decay to an electron and anti-neutrino. This is

[2] A more accurate description distinguishes left and right-handed fermions and the fact that the d, s, and b quarks are mixtures of weak eigenstates. See reference [10]

seen by making use of the rules for manipulating Feynman diagrams. A very useful feature of Feynman diagrams is that a particle can be replaced by its antiparticle and provided the direction is reversed the physics is the same. Applying this operation to the neutrino in figure 1.2, we obtain the decay $W^- \rightarrow e^-\overline{\nu}$ which is shown explicitly in figure 1.3. The W can decay into other leptons ($\mu\nu$ and $\tau\nu$) or into quarks ($W \rightarrow q\overline{q'} \rightarrow hadrons$). The hadronic decay mode is difficult to see above the enormous background process of direct QCD multijet production. The τ lepton decays quickly so that W identification is complicated here also. The μ lepton decays eventually but lives long enough to leave a direct indication of its presence in the detector. The stable electron provides another distinctive signal for identifying W's.

The UA-1 and UA-2 detector collaborations used the lepton decay modes to search for the W boson but we focus only on the electron mode in our discussion. The discovery of the W relied on a sample of events containing an electron with a large component of energy transverse to the beamline. The large energy of the electron is due to the mass energy of the W boson. The electrons were distinguished from jets with the use of a segmented calorimeter. The energetic neutrinos in these events are inferred from a large imbalance of calorimeter energy transverse to the proton beam. The UA-1 collaboration reported 5 clean high energy electron and neutrino events in 1983. The mass of the W boson was measured from the transverse momenta and was found to be $81 \pm 5\ GeV$, in line with existing predictions.

1.4 $W+$ Jet Production in $\overline{p}p$ Collisions

One possible production diagram for W bosons is represented in figure 1.4. In this diagram, $\overline{u}$ and d quarks from the first generation produce a W^- boson. In $\overline{p}p$ collisions, the quarks are provided by the proton and antiproton. The production of partons in association with a W boson is predicted by the QCD sector of the standard model.

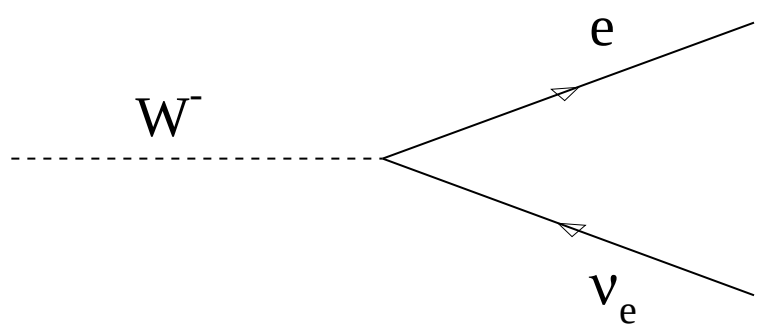

Figure 1.2: The W boson coupling. The electron and neutrino are connected through the weak charged current, the W^- boson.

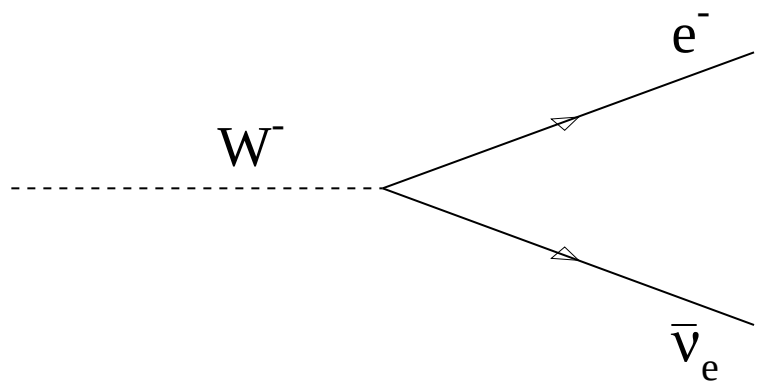

Figure 1.3: Decay of a W^- boson to the first generation of leptons.

QCD allows for the initial state quark in W production to couple to a gluon via the strong interaction. The first diagram of figure 1.5 represents $W+$ 1 parton production. Contained within this diagram is the W production vertex ($q\overline{q} \rightarrow W$) and additionally we see a gluon in the final state. We refer to this type of $W+$ parton production as direct single $W+$ parton production. The essential element for defining the W production as direct and single is the $q\overline{q} \rightarrow W$ part of the diagram. This name distinguishes this process from other sources of W's in $\overline{p}p$ collisions such as top quark decay. Top quark decay contains essentially the same W vertex; however, there is

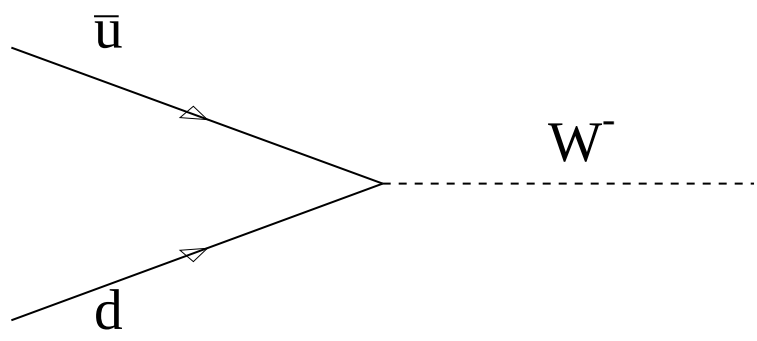

Figure 1.4: Production of a W^- boson from the first generation of quarks.

only one quark in the initial state ($t \to W\ b$).

The first diagram in figure 1.5 is only one example of the leading order contribution to direct single W+1 parton production. Other leading order diagrams are listed in figure 1.5. These represent some of the various initial state partons which can result in a W and parton. The second diagram shows a gluon in the initial state. The gluon can produce a quark pair where one is used in W production and the other becomes a final state jet. Diagrams containing an initial state gluon must also be calculated for a leading order prediction of $W+$ 1 parton production. This is so because gluons mediate the force between quarks so that they are available as proton constituents.

The full complement of the proton actually includes three types of constituents: valence quarks, gluons and sea quarks. The quarks that determine the proton's quantum numbers are called the valence quarks. The valence quarks of the proton are the uud quarks described earlier. We have just described the source of gluons. Finally, there are sea quarks which are virtual quark pairs appearing as intermediate components of the gluon field.

The proton's momentum is shared among its various constituents. The fraction of the momentum that a constituent carries must be known in order to calculate

W production rates. We use parton distribution functions for this purpose. These functions give the probability that a particular constituent of the proton carries a momentum fraction (x) of the proton's momentum. These functions are derived empirically from the world's collision data. They must be evaluated at an energy scale appropriate for W production in 1.8 TeV $\overline{p}p$ collisions. The scale at which the parton distribution function is evaluated is called the *factorization scale*. The description of the factorization scale as it appears in LO calculations specifies the final scale that we study in the $W+$ jet analysis.

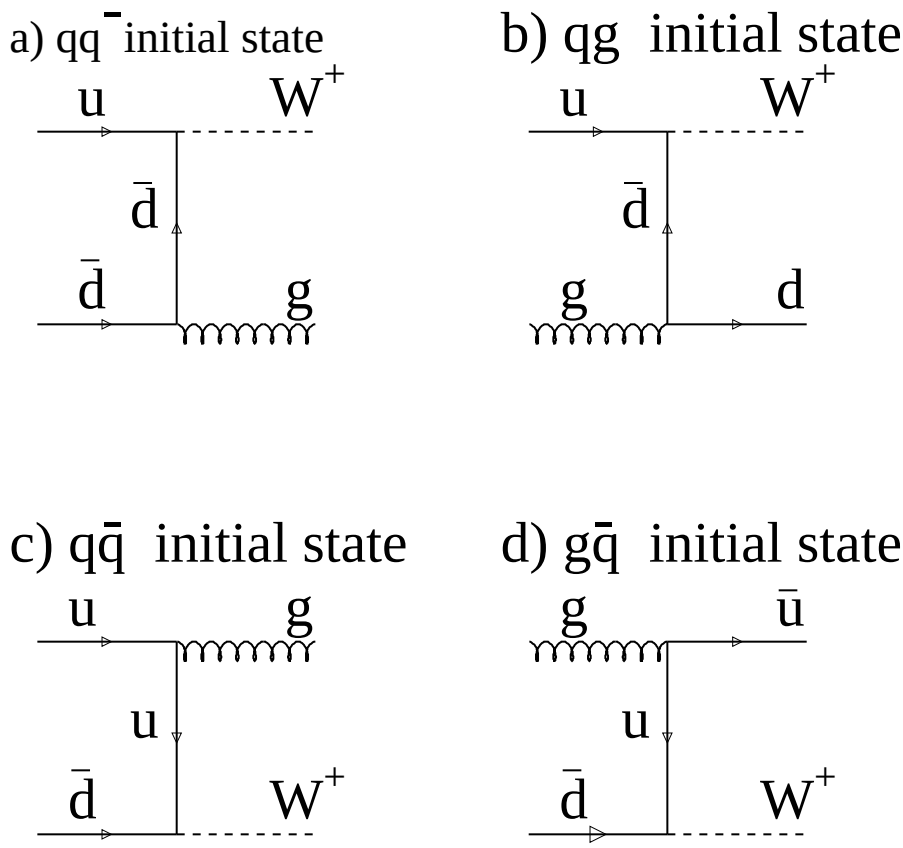

Figure 1.5: $W+$ 1 parton production. Four leading order diagrams representing the production of a W^+ boson from various initial state partons. a) quark and antiquark intial state b) quark and gluon initial state c) quark and antiquark initial state d) antiquark and gluon initial state.

A study of heavy boson plus jets events provides a clean test of perturbative QCD

for several reasons. As mentioned earlier the massive boson requires a large momentum transfer which makes this process suitable for perturbative QCD. Additionally, the production rates at sufficiently high energies provides high statistics data for a precision analysis. Finally the unique decay characteristics of the W allow us to select highly pure samples. Precision electroweak analyses have measured W boson production and decay properties. CDF's published results for the W boson include the W mass [**?**], measurement, the inclusive W cross section measurement [35] and the ratio of the W and Z cross sections [36]. These studies analyzed 20 pb^{-1} of and provided precision tests for the predictions of the standard model. These electroweak analysis developed standard CDF techniques for analyzing the W through its $W \rightarrow e\nu$ decay. This thesis describes the extension of of these techniques to the analysis of W bosons produced in association with jets.

There are several previous CDF measurements for the production characteristics of heavy bosons produced in association with jets. A study published [**?**] in 1993 measured the cross sections of $W \rightarrow e\nu + n$ jets and $W \rightarrow \mu\nu + n$ jets with n=0-4. The jet production rates were corrected back to parton production rates and compared with LO cross section calculations at two renormalization scales ($\sqrt{< P_t >^2}$ and M_W). The data are in good agreement with the theory and favored the higher renormalization scale. The angular and transverse energy spectra of jets in $W+$ 1 and 2 jet events were also compared to the QCD predictions. No significant deviations were found within the statistical uncertainties.

From the feynman diagrams of figure 1.5 we see that the the production of W + 1 parton events can proceed through the exchange of gluon or a quark. Since the spin of gluon is 1 and that of a quark is 1/2 the two exchanges produce different W angular distributions ($\cos\theta^*$) as measured from the W + parton center-of-mass. The quark exchange dominates $W+$ jet production at the Tevatron's energy. A 1994

CDF analysis [?] showed that the $\cos\theta^*$ distribution are in agreement with the QCD predictions at LO QCD and NLO QCD.

A more recent CDF analysis (1994 [33]) measured the production rate and kinematic properties of jets produced in association with the Z boson. This analysis used the $Z \to e^+e^-$ decay to select Z bosons. The production rate of $Z \to e^+e^-$ events is a factor of 10 below $W \to e\nu$; however, the analysis utilized 6708 $Z \to e^+e^-$ events from 108 pb^{-1} of luminosity collected over the 1992-93 and 1994-95 Tevatron runs. The $Z+$ n jet cross sections were measured for n=1-4. The data were compared to enhanced LO QCD [3] predictions for n = 1-3. The data and theory were in agreement within the inherent LO uncertainties. The jet angular and transverse energy distributions were also used to test the theory. The angular separation of two jets in $Z+ \geq 2$ jet events are of particular interest because the rate of collinear jets is sensitive to the fragmentation scale used in the parton fragmentation model. The data for this distribution is best reproduced in the theory by not limiting the added radiation from initial and final state partons.

The current analysis of $W+$ jets extends the work from these analyses described above. We have 51431 W events. Of these 11444 W events have at least one reconstructed jet, a number comparable to the total number of W events used in the 1992-93 analyses. We test the enhanced LO QCD predictions for cross sections and jet kinematic properties through the 4 jet channel.

1.5 Chapter Summary

We have reviewed from an interpretive perspective the fundamental ideas of the standard model. The list below summarizes those features of the standard model that allow reliable predictions for $W+$ jet events produced in $\sqrt{s}$= 1.8 TeV $\overline{p}p$ collisions.

[3] see chapter 7 for a description of the enhanced LO calcualtion

1. W **decay:** The W boson's decay properties are well predicted by the electroweak sector of the standard model.

2. **factorization:** The small coupling of the strong force at very small distance scales allow the proton constituents to be treated as quasi-free particles. This feature allows us to calculate the hard parton interactions without considering the inter-parton coupling of the constituents. The details of the proton structure do enter the predictions in the form of parton distribution functions. The scale at which we evaluate the proton structure is called the factorization scale and determines the level at which the quarks and gluons participate in W production.

3. **perturbation:** The perturbative approximations of QCD can provide accurate predictions for strong interactions. The calculations introduce the renormalization scale. The value of the scale is determined by physics process under study.

4. **fragmentation:** Parton production and parton fragmentation are decoupled. The conversion of a final state partons into multiple hadrons results in a jet of hadrons. Jets can be corrected back to the parton level which allows tests of perturbative QCD. The modelling of fragmentation in the theory introduces a third scale, fragmentation, into the predictions.

The following list presents the experimental advantages of the $W+$ jets analysis.

1. W **production:** Identifying W bosons and high E_T jets selects processes involving large momentum transfers suitable for the perturbative approximation.

2. W **decay:** The final states of W decay that contain an electron and neutrino (10%) allow the collection of a highly pure sample of W bosons.

3. **direct single W's:** Direct single W production in association with jets is the dominant source of real W production. The analysis of these events provides a sufficient number of $W+$ 4 jet events to study QCD at leading order up to the 4th order of α_s.

The next five chapters describe in detail the experimental aspects of the $W+$ jet analysis. In chapter 7 we return to the theory to discuss its implementation. The data and theory are then compared.

Chapter 2

The Experiment

2.1 Introduction

The Collider Detector at Fermilab (CDF) is a multi-purpose and multi-element detector designed for precision energy, momentum, and position measurements of particles produced in $\sqrt{s} = 1.8\ TeV\ \overline{p}p$ collisions. The focus of the discussion will be those elements useful in identifying the final state particles of $W \rightarrow e\nu$ + jet events. The principle detectors used in analyzing these events are the vertex detector (VTX), the central tracking chamber (CTC) and the full set of hadronic and electromagnetic calorimeters (table 2.1). The VTX allows us to reconstruct the position along the beam line where a W boson is produced. The CTC precisely measures a particle's trajectory over a 1.4 meter radius from the beam line. The track curvature as measured by the CTC along with the known solenoidal magnetic field determine the electron's momentum. The most accurate measurement of a W electron's energy is derived from the central electromagnetic calorimeter (CEM). The CEM and CTC together provide several discrimination tests that are used to separate electrons from other physics objects such as photons and jets. The description of CDF will be limited to the basic operating principles of each detector, the geometric coverage of the various detectors, and the resolution for their particular measurements.

CDF is designed to collect data in the high-energy and high particle intensity environment produced by the Tevatron. The Tevatron synchrotron accelerator provides the world's highest energy $\overline{p}p$ collisions. Although many of the details of the Tevatron are irrelevant for the $W+$ jet analysis, some aspects of the collisions do present challenges. We briefly describe proton and antiproton production and the

methods used to accelerate these particles to relativistic energies.

2.2 The Tevatron Collider

Color confinement prevents us from isolating individual quarks in order to accelerate and collide them. As described in chapter 1, the quark model states that these fundamental constituents of matter exist in pairs as mesons or in triplets as baryons. Therefore we need to collide hadrons in order to observe parton interactions. The accelerators at Fermilab are capable of accelerating protons and antiprotons to 900 GeV. The Fermilab accelerator complex is shown in the diagram of figure 2.1. The major components are shown and include the linac, booster, main ring and Tevatron.

The Tevatron is a synchrotron accelerator. Synchrotrons use magnetic dipoles to steer particles in circular orbits. RF oscillations are used to accelerate the particles. As the relativistic particle's momentum increases the dipole magnetic fields are synchronously increased to maintain a constant orbital frequency and a nearly constant orbital radius. For proton acceleration the limit of the proton's energy is determined by strength of the magnetic dipoles. The progenitor of synchrotrons was the cyclotron built at the Radiation Laboratory at Berkeley [14] in 1931. It measured a few inches across and reached an energy of 80 KeV. The Tevatron synchrotron has a radius of 1 km and uses superconducting dipole magnets to maintain the proton's orbit. The Tevatron accelerates protons to 900 GeV.

A very useful feature of synchrotrons is that the particle can be replaced by its antiparticle and provided the direction is reversed the physics is the same. The Tevatron can simultaneously accelerate protons and antiprotons in opposite directions thus providing 1.8 TeV center-of-mass system (CMS) collision energy.

The creation of a beam of protons begins by negatively charging a hydrogen atom. The H^- ion is accelerated by a linear accelerator to an energy of 400 MeV and injected

into the booster. During injection the H^- ions are stripped of their electrons leaving bare protons in the booster which are raised to an energy of 8 GeV. The protons are transferred to the main ring and are ramped to an energy of 150 GeV in preparation for their transfer to the Tevatron. The Tevatron is located directly below the main ring. Although the Tevatron has the same radius as the main ring it is capable of much higher proton energy since it is fitted with superconducting dipoles. Within the Tevatron the protons reach their final energy of 900 GeV.

Antiprotons are not abundant and must be created as needed. Antiproton production is achieved by colliding protons from the main ring into a nickel target. Antiprotons that are produced in the collisions are collected in the accumulator. After enough antiprotons are accumulated they are injected into the main ring and then into the Tevatron. The oppositely rotating beams are steered into one another at two locations along the Tevatron's circle one of which is $B0$. $B0$ marks the center of the Collider Detector at Fermilab.

Protons and antiprotons inside the Tevatron exist in bunches which means they are localized around specific points along the circumference. There are 6 bunches of protons and 6 bunches of antiprotons so that a crossing of a proton and antiproton bunch occurs every 3.5 microseconds. The bunches have an extension along the beam line on the order of a meter. Since a proton and antiproton can collide anywhere along the the overlap of proton and antiproton bunches, the $\overline{p}p$ collisions are spread about $B0$ in a distribution. The distribution of $\overline{p}p$ collisions is approximately gaussian with a width of $\approx 30\ cm$. Precise determination of the position ($vertex$) of the $\overline{p}p$ collisions allows accurate measurement of the component of energy transverse to the beam line.

The proton bunch typically contains about 10^{11} protons and an antiproton bunch contains about a tenth of this number. The achievement of many particles per bunch and other accelerator improvements has resulted in a significant probability that more

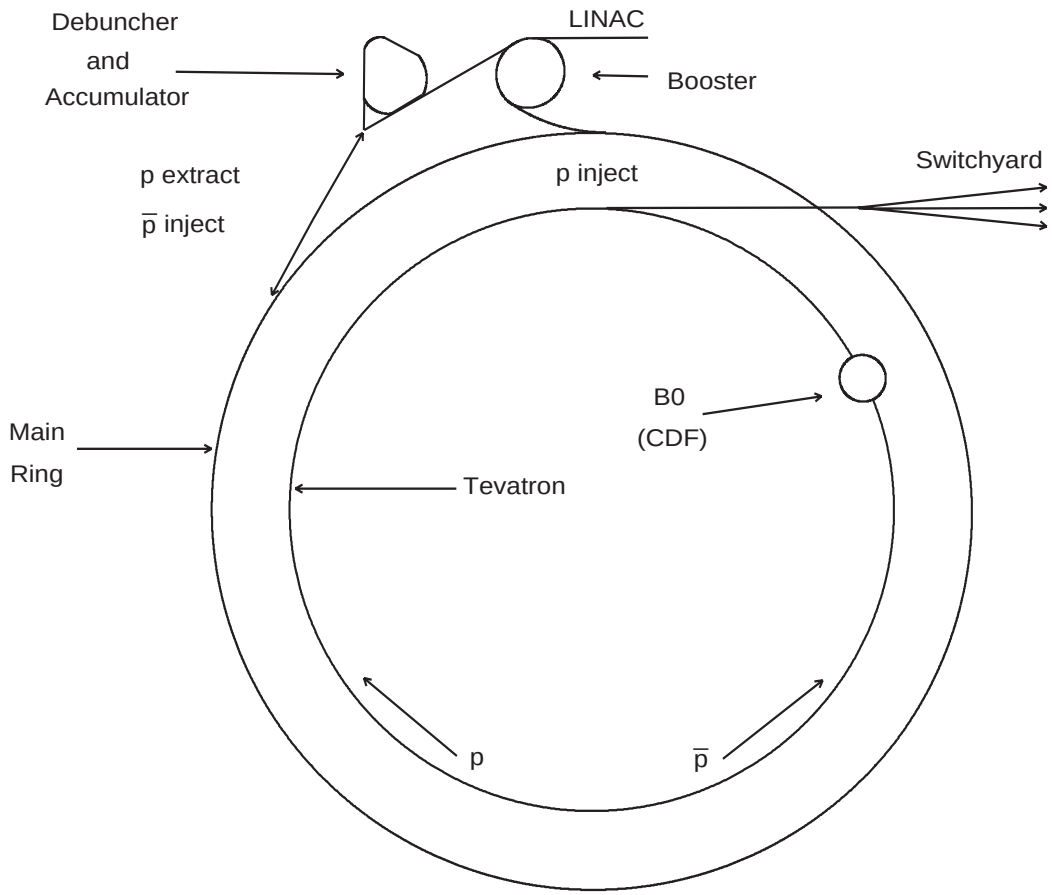

Figure 2.1: Schematic of the Tevatron which shows the major elements used in accelerating protons and antiprotons. The Tevatron is actually the same diameter as the main ring but is shown as smaller in the diagram.

than one $\overline{p}p$ pair collide in a proton-antiproton bunch crossing. We refer to events with more than one $\overline{p}p$ collision as *multiple interaction* events. The probability that more than one hard collision occurs is small; therefore, the typical contamination from interactions that occur simultaneously with a W interaction is generally low-energy. These extra interactions can have an impact on the determination of jet and neutrino energy; therefore, we must use the detectors ability to identify these interactions to subtract their contribution.

The probability that a W is produced in a crossing of proton and antiproton

beams depends on two factors. The first factor is simply the production cross section of the process at the energy of the collision. The cross section is determined by nature and we measure this quantity for W's produced with jets. The second factor depends on the characteristics of the $\overline{p}p$ beams. The number of particles per bunch, the number of bunches, and the width of the beam can be optimized to enhance the probability of a $\overline{p}p$ collision. These features are not fundamentally important except that they provide us with high statistics data. The *luminosity* is a measure of the beam characteristics and it is defined with respect to a known cross section.

$$L = \frac{N_{BBC}}{\sigma_{BBC}} \tag{2.1}$$

The subscript in equation 2.1 refers to a detector at CDF which measures $\overline{p}p$ scattering at low angle to the beam. The number of these scatterings (N_{bbc}) after an efficiency correction [1] is used with the known cross section (σ_{bbc}= 51.15 mb) to define the luminosity. The luminosity as a function of time is called the instantaneous luminosity and this quantity determines the probability of the multiple interactions described above.

The last feature of $\overline{p}p$ interactions that we discuss before moving on to the detector is called the *underlying event*. We have so far ignored the fact the protons and antiprotons contain additional partons which do not play a role in the hard interaction. These particles will manifest themselves in the detector as low energy depositions. Their contribution to jet energy measurements and missing transverse energy determination are accounted for in the analysis of $W+$ jet events (chapter 3).

[1] Multiple interactions will only register as one event

2.3 The Collider Detector at Fermilab

2.3.1 Overview of The Collider Detector at Fermilab

The coordinate system at CDF is defined with respect to the proton beam direction (figure 2.2). The positive z direction is the proton beam direction. ϕ is the azimuthal angle and is measured with respect to the beam axis with the proton beam defining the sense. The polar angle θ is the angle from the proton beam. The radius R is the perpendicular distance to the beam line. The transverse component of energy and momentum of a particle is the projection into the plane transverse to the beam line.

Two fundamental symmetries utilized in the detector design are the ϕ symmetry and θ symmetry. The equal energy and momentum of the proton and antiproton beams is reflected in the detector's symmetry about $\theta = 90°$. An alternative variable to θ is the *pseudorapidity* which is defined by

$$\eta = -\log\left(\tan\left(\theta/2\right)\right)$$

The pseudorapidity is the massless approximation of the rapidity which is a natural variable for particles at relativistic energies since it is additive under lorentz boosts. The pseudorapidity is equal to zero at a θ of 90°. Positive η is in the proton direction (east side of the detector).

Since the detector is symmetric in ϕ and η we show only one quarter of the detector's cross section which is presented in figure 2.2. The center of the detector ($B0$) is near the lower right hand corner of figure 2.2. Protons travel from right to left along the beam line which is indicated as a dark bar along the bottom of the figure. Moving in the transverse direction from $B0$ we first encounter the silicon vertex detector (SVX). The SVX is designed to locate decays of long-lived particles such as B mesons. We use the SVX for identifying (or *tagging*) events containing b quarks. B-tagging is useful in cross checking the *top* quark production estimates since

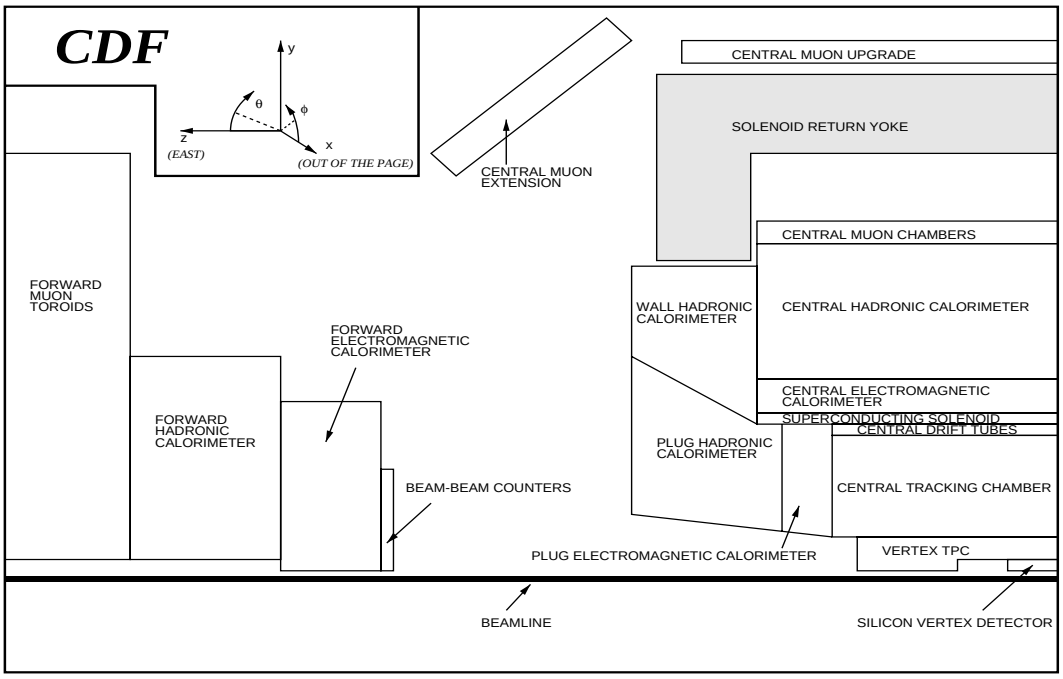

Figure 2.2: One quarter of the Collider Detector at Fermilab. The major detector elements are indicated. $B0$ (the center of the detector) is along the beam line to the far right.

top quarks decay almost exclusively to a final state containing a b quark. The SVX fits inside a larger vertex detector, the primary vertex detector (VTX). The VTX is a time-projection chamber used to reconstruct the z position of $\overline{p}p$ interactions along the beam line. Outside the VTX is a large central tracking chamber (CTC) used for 3-D tracking. The paths of charged particles inside the CTC are helical due to a 1.4 T solenoid surrounding the CTC. The track curvature permits accurate momentum measurement of charged particles.

The tracking detectors discussed in the preceding paragraph are designed to obtain measurements with minimal interference to the particles energy. The massive solenoid obviously spoils this scheme but is nicely positioned as the first stage of the calorimetry. The calorimeters achieve energy measurements of particles by absorbtion. Those calorimeters designed to contain electromagnetic energy such as electron

Table 2.1: The abbreviations and names of the CDF elements.

Detector		Name
Tracking	SVX	Silicon VerteX detector
	VTX	VerTeX detector
	CTC	Central Tracking Chamber
	CDT	Central Drift Tube array
	CES	Central Electromagnetic Strip chamber
Calorimetry	CEM	Central ElectroMagnetic
	CHA	Central HAdronic
	WHA	Wall HAdronic
	PEM	Plug ElectroMagnetic
	PHA	Plug HAdronic
	FEM	Forward ElectroMagnetic
	FHA	Forward HAdronic
Muon Detectors	CMU	Central MUon
(Tracking)	CMP	Central Muon uPgrade
	CMX	Central Muon eXtension
	FMU	Forward MUon

energy are placed in front of the hadronic calorimeter. As will be discussed below, this arrangement allows reliable electromagnetic energy identification and accurate electromagnetic energy measurements. The combined calorimetry at CDF has 2π ϕ coverage and extends to η of $\pm$ 4.2 (2° from the beam line).

The muon systems are located outside the calorimetry. The muon detectors include the central muon detector (CMU), the central muon upgrade detector (CMP), and the central muon extension (CMX). These systems consist of streamer chambers which signal the presence of charged particles. Muons pass through the calorimetry depositing only a small amount of energy. A track stub in the muon chambers matching with the ionizing energy in the calorimetry identifies a muon candidate. The muon systems are not utilized in the $W+$ jet analysis since we analyze only the $W \rightarrow e\nu$ decays.

The elements of the CDF detector critical to the $W+$ jet analysis are the VTX,

CTC and the calorimeters. We discuss these detectors in some detail in the following paragraphs but a full description of the detectors components can be found in [15].

2.3.2 The Tracking Chambers

The tracking chambers that we discuss are designed to measure the path of a charged particle as it traverses the detector volume inside the solenoid. Charged particles leave a trail of ionized gas. The freed electrons are accelerated by large electric fields and their collisions with the gas liberate more electrons. The sequence then repeats and eventually results in an avalanche of electrons which are collected on the sense wires of the chamber. The time delay (drift-time) between the initial ionization and the "hit" on the sense wire is converted to a distance and provides one point in a particle's trajectory. A variety of wire orientations and chamber segmentation can be used to optimize the track measurements in specific planes of projection. We discuss the configurations of the VTX and CTC.

The Vertex Detector (VTX)

As mentioned earlier the $\overline{p}p$ collisions are spread over a gaussian distribution of width 30 cm. The purpose of the VTX is to identify the z position of the collision (vertex) so that we may calculate $\sin(\theta)$ of energy deposited in the calorimetry. This allows the measurement of the transverse component of energy ($E \cdot \sin(\theta)$). The VTX is also capable of reconstructing multiple vertices. In the current running conditions, knowledge of the number of interactions occurring in a single crossing of proton-antiproton bunches allows us to correct for the contamination of energy in the calorimetry due to extra interactions.

The VTX is a drift-time proportional chamber which achieves accurate vertex information because it is optimized for precision track measurements in the r–z plane.

Each chamber of the VTX is an annulus with a width (along z) of 5 cm. A chamber is divided in to 8 ϕ slices with the sense wires of one octant transverse to the beam line in a ladder configuration. The drift velocity of the gas is parallel to the beam line so that the drift-time is converted to a z position of the ionizing particle while the radial coordinate is determined by the radial position of a sense wire.

Each octant of a drift chamber samples the particles trajectory at 24 points[2]. Pattern recognition software collects the individual wire hits to reconstruct the track of the ionizing particle. Multiple tracks which converge to a common origin identify the vertex. Vertices are ranked according to the number of hits and number of track segments used in reconstruction. A class designation of 12 is the highest rank and requires that more than 180 hits are used in the vertex reconstruction. In the following chapters the term vertex refers only to *class 12* vertices unless the class is mentioned explicitly.

The VTX event display in figure 2.3 shows the reconstruction of vertices. The display shows the 48 individual chambers or *half modules*. Half modules are paired with each half at a slightly offset rotation so that the ϕ coordinate of a charged particle is isolated to a region smaller than 1/8 of a chamber. The resolution of a reconstructed vertex is approximately 2.0 mm [16].

The Central Tracking Chamber (CTC)

Precision tracking is provided by the the central tracking chamber (figure 2.4). We use the information provided by the CTC in several important ways. Three-dimensional tracking allows us to match the track from a W electron with the position of the electron's energy in the electromagnetic calorimeter. The electron's momentum is also derived from CTC tracking and is required to be consistent with the electron's

[2]modules which accomodate the SVX have only 16 sense wires

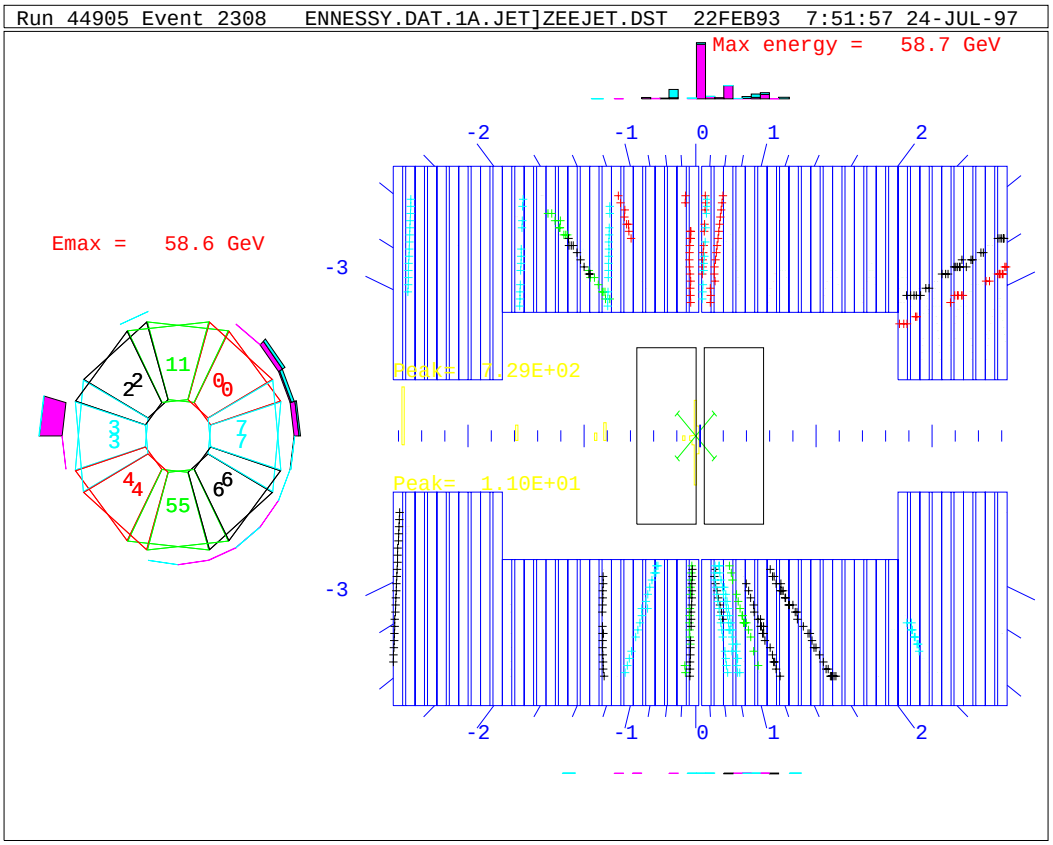

Figure 2.3: VTX event display. The figure shows a reconstructed vertex in a W boson event. The left side shows the octants of two half modules with one offset in ϕ with respect to the other to achieve a stereo view. The beam line is perpendicular to the page for this figure. In the figure on the right the beam line is horizontal. We can see the track stubs in the VTX converging at a point along the beam line (a vertex). The vetrical direction has been expanded.

energy in the calorimeter. Finally the CTC track provides a means of isolating the W event vertex from other vertices in the event via matching of VTX vertex and CTC electron track measurements.

The 84 cylindrical wire layers of the CTC run parallel to the beam line for a length of 3.2 meters. The CTC provides 84 individual wire hits out to a radius of 1.4 meters for use in track reconstruction. The gas drift direction is in the ϕ direction around the beam line. This configuration optimizes for track measurements in the plane transverse to the beam line.

The curvature of charged particle trajectories due to the 1.4 T solenoidal field is in the transverse plane so that the precision transverse tracking translates to precision transverse momentum measurements of charged particles. The resolution for momentum measurements is a function of the curvature of the track and thus of the transverse momentum of the particle:

$$\frac{\sigma P_T}{P_T} < .001 \cdot P_T$$

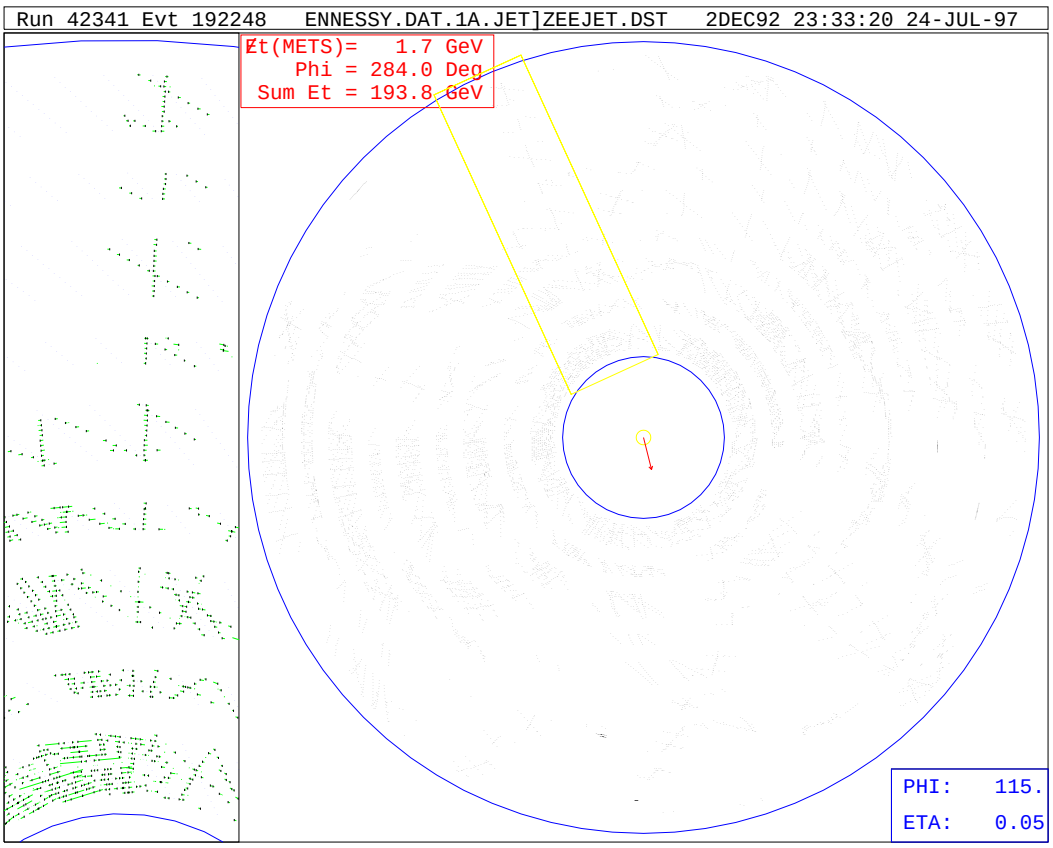

Figure 2.4: Transverse view of the CTC. The beam line is in the center and perpendicular to the page. The figure shows the wire hits due to charged particles ionizing the gas. The dotted box encloses a stiff (high momentum) electron track. This view is expanded in the side-box of the figure. In the expanded view we see the individual wires and wire layers of the CTC. For every hit on a wire there is a two-fold ambiguity in the direction to the charged particle. The ambiguity is resolved by matching segments across layers.

Three-dimensional tracking in the CTC is possible through stereo arrangement of the wires. The layers of wires are grouped into two types of *superlayers* (figure 2.4). Stereo (odd numbered) superlayers are alternatively tilted $\pm$ 3° which allows track reconstruction in the $r-z$ view. If we require a particle to cross all superlayers, then the η coverage of the CTC is between +1.2 and −1.2. The CTC has full ϕ coverage.

2.3.3 The Calorimeters

The calorimeters are used extensively in the $W+$ jet analysis. The central electromagnetic calorimeter provides electron position and energy measurements. The central, endwall and plug calorimeters are used for finding jets and determining jet energy. The complete set of calorimeters which includes the forward calorimeters are used to measure the imbalance of transverse energy (missing transverse energy $\not{E}_t$) in a W event. The segmentation and coverage of the CDF calorimetry is shown in figure 2.5.

The CDF calorimetry employs two important components: absorbing material and sampling material. The absorbing material is typically a heavy metal such as lead or iron which serves to promote electromagnetic or nuclear showers. The sampling layers are interleaved with the absorber and are designed to measure the shower activity at specific radii.

Central Electromagnetic Calorimeter (CEM)

The CEM is a metal-scintillator sandwich calorimeter which spans the η region from -1.1 to +1.1. Lead which has a high Z (shell electrons) is suitable for promoting electromagnetic showers which are initiated from high energy electrons. The high-energy Bremsstrahlung γ's produced in these interactions convert to electron-positron pairs so that the cycle can repeat until the energy of the parent electron is spent.

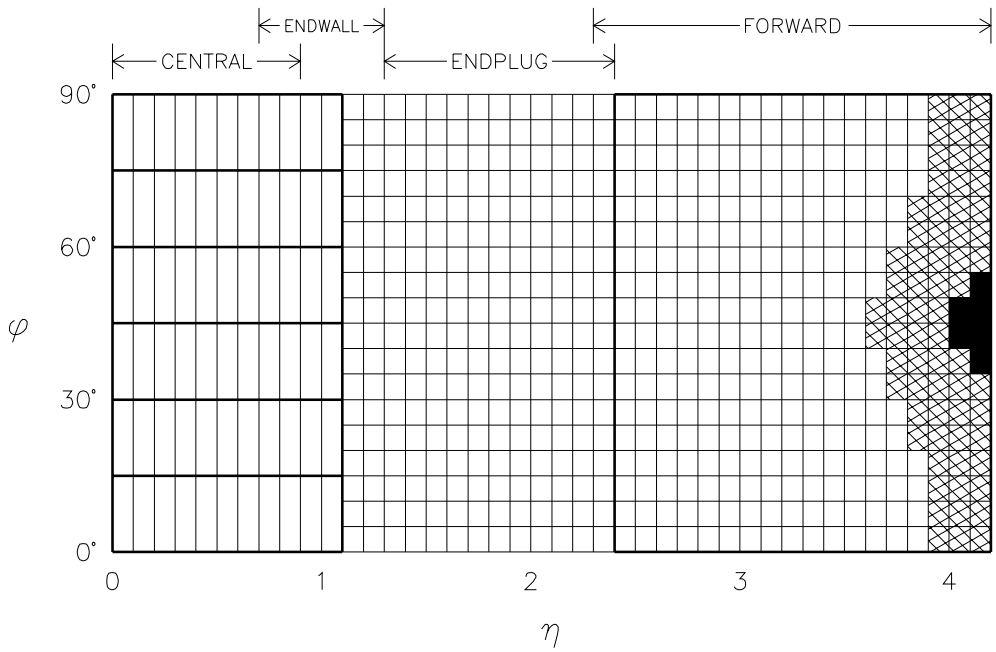

Figure 2.5: Map of the calorimetry coverage which shows the η-ϕ coverage of the separate calorimeters. The figure shows the sections from $\phi = 0°$ to $90°$ and η from 0.0 to 4.2 (East side). The small squares represent the tower segmentation of the calorimeters.

Layers of scintillator sample the shower at over 20 radial positions. The light output from the scintillator is measured by phototubes connected via light guides.

The cylindrical CEM is divided into 48 ϕ wedges. One *wedge* of the CEM covers 1/24 (15° in ϕ) of the circumference and a pseudorapidity range of 0.0 to +(-)1.1 on the East(West) sides of the detector. A wedge is divided into 10 equal units of pseudorapidity. Therefore the finest segmentation of the CEM is 15° by 0.11 units of pseudorapidity. This level of segmentation is known as a *tower*. The tower segmentation is maintained throughout the depth of the CEM which results in a projective tower geometry where all towers point back to the center of the detector. Figure 2.6 shows a wedge of the central calorimeter with the projective geometry evident.

The characteristics of electron energy deposited in the calorimeter towers are well understood and can be used to distinguish electron energy from other types of

energy. First, the energy from a high energy electron is generally contained within the electromagnetic calorimeter. The hadronic calorimeter towers that are directly behind the EM towers will contain only a small fraction of the electron's energy. The electron's energy is also typically very localized within the EM towers with most of the electron's energy confined to one EM tower or two if the electron hits near an edge of a tower. The lateral and vertical sharing of energy across towers provide useful discrimination tests for electrons.

Once we have isolated electrons from other detector energy, we use the CEM to measure the energy of the electron. The measurement of energy is essentially a counting measurement. The scintillator's light output is proportional to the number of particles created in the EM shower so that the error on the energy goes as the square root of the number of particles (energy). This means that the energy measurements of the CEM and momentum measurements of the CTC are complementary in that the momentum resolution gets poorer at higher momentum while the CEM's energy measurement improves. For the high energy electrons from W decay the CEM provides the best energy-momentum measurement since we can neglect mass at these energies. The CEM has the added advantage of being insensitive to γ's radiated off the electron (Bremsstrahlung) since the calorimetry integrates over a sufficiently large cone to capture this radiation much of the time. The energy resolution of the CEM is

$$\sigma(E)/E = \frac{.135}{\sqrt{E \cdot \sin\theta}}$$

where the units are GeV.

The position resolution of the CEM is much better than would be expected from the tower segmentation because within the CEM there is an embedded strip chamber as shown in 2.6. Charge collection of the orthogonal strips and wires of the strip

chamber (figure 2.7) provide a shape (or *strip profile*) of an EM shower at the expected shower maximum. The profile of an electron shower as determined by the CES provides variables for discriminating electrons from other objects. The shape of the charge deposition in the CES can be compared to expected shapes gathered from electron test beam data. The CES profile is also used to measure the position of the electron within a calorimeter tower with a position resolution of better than 2 mm. We quote the position of the electron within a tower using a local coordinate. *Local* X is defined as the distance from the center of a tower in the $R \cdot \hat{\phi}$ direction. The z direction (along the beam) is orthogonal to local x and is also determined from the CES profile. These coordinates are shown explicitly in figures 2.6 and 2.7.

The accurate position of the electron within a tower can be compared to the expected electron position as determined from the CTC track measurements. These track matching requirements are referred to as Δx and Δz. The CTC tracking information combined with the CEM measurements allow us to distinguish electrons from high energy photons since both leave similar calorimetry signatures but only the charged electron ionizes the tracking gas.

Central and Endwall Hadronic Calorimeters (CHA,WHA)

The central and endwall hadronic calorimeters (CHA and WHA) are steel-scintillator sandwich calorimeters. The showers of hadronic calorimeters are initiated from collisions of hadrons with the carbon and iron nuclei. The calorimeters consist of 48 steel-scintillator layers with a segmentation designed to match the CEM which is in front of the hadronic calorimeters. The coverage of the cylindrical CHA is 2π in ϕ and $\pm$ 0.88 in η. The endwall extends the η coverage to $\pm$ 1.32. The endwall calorimeter contains a conical hole centered around the beam line to accomodate the plug calorimeter.

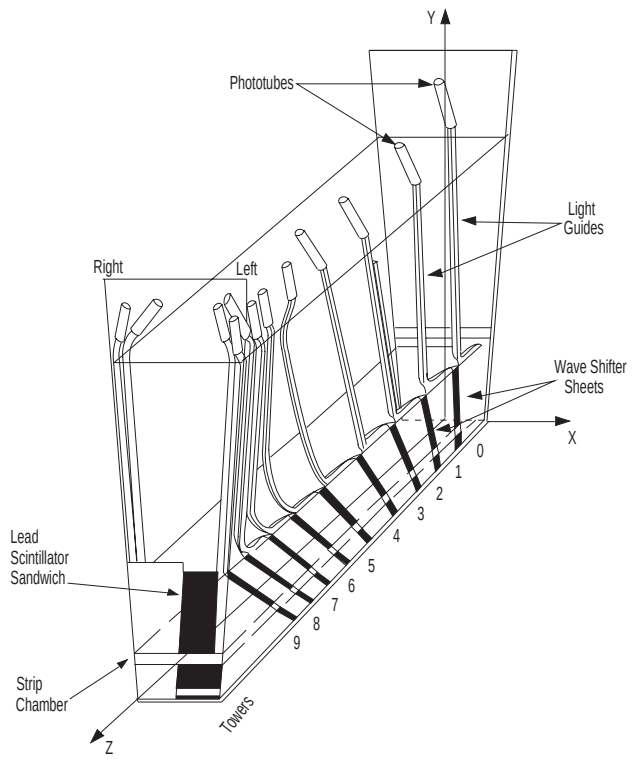

Figure 2.6: One wedge of the CEM. Shown are the basic components: lead-scintillator sandwich for absorbing and measuring electromagnetic energy, wavelength shifter and light guides to carry the output of the scintillator to the photomultipliers. The ten towers are numbered from 0 to 9 and each cover 0.11 units of η. The z axis in the figure indicates the direction of the proton beam. Local x ,tangent to the ϕ direction, is shown. The CES is embedded in the CEM where the maximum of an electron shower is expected to be. The CES (see figure below) measures the electron position in the x and z coordinates.

The designed energy resolution for the CHA and WHA is $\sigma(E)/E = \frac{.5}{\sqrt{E}}$. The fine segmentation (0.11 by 15°) of the calorimeter means that a jet will deposit energy over many towers. Energy from jets is also typically deposited in both the EM and the hadronic towers. Therefore the jet reconstruction and jet energy measurements use both sets of calorimeters. The matching segmentation of the EM and hadronic calorimeters makes a combined EM and hadronic energy measurement straightforward by defining a jet-tower as the EM tower plus its associated hadronic tower.

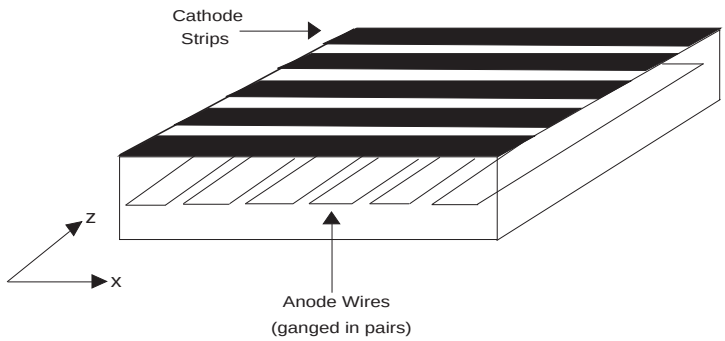

Figure 2.7: The Central Electromagnetic Strip chamber which provides a transverse profile of the electron's shower in the CEM. A CES module fits into one tower of the CEM and measures the electron's position in the x and z coordinates to within 2 mm (for electron of transverse energy 50 GeV).

The Plug and Forward Calorimetry

The remaining calorimeters at CDF use gas proportional tubes instead of scintillator to sample showers. The amount of charge collected on the wires is proportional to the the gas ionization which is in turn proportional to the energy of the initiating hadron. The advantage of proportional tubes is the ability for finer tower segmentation in the calorimeters which is necessary in the higher pseudorapidity regions. The segmentation of the gas calorimetry in pseudorapidity is 0.11 while the segmentation in ϕ is 5°. The plug and forward calorimeters consist of inner electromagnetic and outer hadronic calorimetry. The η coverage of the plug hadronic calorimeter is from 1.32 to 2.4 and from -1.32 to -2.4. The inner EM plug calorimeter covers a slightly larger range, +(-)1.1 to +(-)2.4. The forward calorimetry extends the coverage of the CDF calorimetry to $\pm$ 4.2 which is within 2° of the beam.

The front faces of the conical shaped plug and forward calorimeters are transverse to the beam direction. In figure 2.8 we show the segmentation for the forward electromagnetic calorimeter as seen by a particle approaching along the beam line. The segmentation of the plug calorimeters is qualitatively the same.

The plug calorimeters are used to identify jets in the $W+$ jet analysis. Reconstruc-

tion of jets is done only in the central, wall, and plug calorimeters where calibration of high energy jet clusters are well-understood. The absence of the forward jets in our analysis represents about a 5% decrease in the number of jets reconstructed. We do use the forward calorimetry to reconstruct the neutrino momentum. Although there are 2° holes in the forward calorimetry the transverse component of the escaping energy is typically small due to the $\sin(\theta)$ factor.

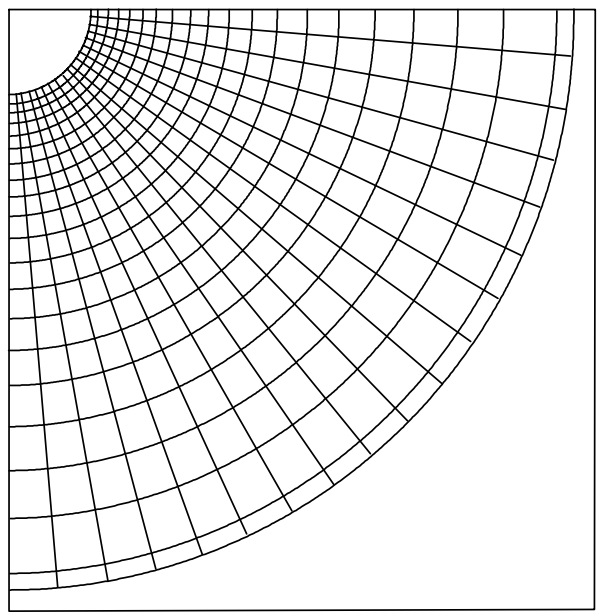

Figure 2.8: Tower segmentation for one quarter of the forward EM calorimeter (FEM). The beam line (upper-left corner) is transverse to the page. Towers are 5° by 0.11 units of η.

2.3.4 The Fiducial Coverage of the Calorimetry

The discussion of the CDF calorimeters presented the geometric coverage of the individual calorimeters. This coverage is to be distinguished from the fiducial coverage. The fiducial area of the calorimetry is the area where we obtain reliable measurements. The fiducial coverage is important in defining the acceptable regions for

electrons in the CEM. Some gaps exist in the CEM where wedges meet. The center gap is the junction of east and west sides ($\eta = 0.0$). Additional gaps include the ϕ gaps between adjacent wedges every 15°. We require that electrons are 3 cm from the edge of a wedge in order to obtain the best electron energy measurement. A few individual towers are excluded from the fiducial area because of known problems or because detector instrumentation shares the tower's space.

Jets are relatively extended objects so that confining a jet to reside in completely fiducial regions would be too restrictive. Instead we correct jet energy losses as a function of their position. These corrections are described in the next chapter.

2.4 Chapter Summary

In this chapter we have described the experimental apparatus used in the analysis of $W+$ jet events. W bosons are produced by 1.8 TeV center-of-mass collisions of proton-antiproton pairs. The CDF detector which collects the data from these collisions was described with emphasis on those detectors critical for identifying electrons, jets and neutrinos. The VTX vertex detector measures the z position of the $\overline{p}p$ collision along the beam. We use the vertex position to compute the transverse component of energies deposited in the calorimetry. The CTC tracking provides the momentum and position of the electrons in the analysis and aids in isolating the W vertex. This information is used in tandem with the central electromagnetic calorimeter measurements to isolate electrons from all other forms of calorimetry depositions. The central, wall, and plug calorimeters are used to reconstruct jets and measure their energy. The complete set of calorimeters at CDF provide the coverage necessary for identifying events with large missing transverse energy ($\not\!\!E_t$) used in the inference of an escaping neutrino.

Chapter 3

Identifying W Bosons and Counting Jets

3.1 Introduction

CDF excels at electron identification and precision electron energy measurement. We use this ability to select a clean sample of events containing high energy electrons. We describe both the kinematic selection of the electrons and the discrimination variables that are employed to distinguish electrons from other types of energy. The inclusive electron sample will contain those electrons which were produced from a W decaying to electron plus neutrino. A W sample can be extracted from the electron sample by the identification of the neutrino. The result of high energy electron and neutrino selection is a 94% pure sample of W bosons.

The W sample is divided into subsamples according to the number of jets produced with the boson. In contrast to the electron, the definition of a jet is more of an analysis decision. Jets produced with a W can have essentially any energy and the jet's pattern of energy deposition varies from jet to jet. However, if the jet energy is corrected to represent the energy of the parent-parton, a precise definition is a matter of the capabilities of the detector and the validity of the theoretical predictions at the minimum allowed jet energy. The analysis cuts used in defining a jet are presented in this chapter.

3.2 Electron Selection

3.2.1 Trigger Path

During active data collection in the period from 1992 to 1995 at the Collider Detector at Fermilab, there were about 5.5 trillion $\overline{p}p$ interactions in the detector's collision region, and only 2.5 million of these events were W bosons produced. Only 10% of these decayed to the desired final state($e\nu$).

In order to reduce the events recorded for analysis and enhance the fraction of recorded events with interesting physics, we employ a series of online triggers. A trigger is loosely defined as a set of cuts such as a minimum energy deposit in the calorimeter or minimum track momentum in the central tracking chamber which determines whether an event is saved for analysis or discarded. The $W+$ jet analysis uses a trigger path that is designed to identify events with a high transverse energy central ($\eta \leq 1.2$) electron. This sample contains $W \rightarrow e\nu$ decays along with a variety of other inclusive electron processes. The electron trigger data sample is used as the starting point for the offline analysis.

For most of run 1, the level-one triggers were the first of a series for filtering the hard scattering events from $\overline{p}p$ collisions[1]. An event need only pass one of the individual level-one triggers. A requirement of one level-one calorimeter trigger is that an event deposit a minimum transverse energy of 8 GeV in a central-electromagnetic calorimeter tower. It is this requirement on which the W boson selection relies most.

Events which pass the level-one triggers are evaluated at level-two. In our analysis, we require that an event pass the level-two combined central electron trigger. This trigger consists of 16 individual central electron triggers; however, our data sample depends predominately on the high E_T electron trigger. This requires a electromag-

[1]For part of run 1 a *level-zero* trigger was employed which required a beam-beam counter coincidence.

netic transverse energy of 16 GeV and a track of momentum 12 GeV. The fraction of hadronic energy in the associated hadronic towers is required to be small ($.125 \cdot E_T(\mathrm{EM})$) in order to suppress jets. The allowed η range for the energy deposition is ± 1.19.

Level-three is the last set of triggers to be applied. Level-three uses reconstructed data so that specific physics decisions can be made. There are level-three triggers designed to identify W bosons and Z bosons; however, we use the inclusive electron level-three trigger. Our choice allows us to select W and Z bosons from a common trigger sample so that the systematic errors in efficiencies and backgrounds are common. Additionally we gain efficiency with the inclusive electron trigger, which passes W's that do not pass the specific W triggers. The most important inclusive trigger we use has higher track momentum (13.0 GeV/c) and higher electromagnetic energy (18.0 GeV) requirements than level-two. This trigger also requires that the 3D track point to the calorimeter energy thus identifying electrons and rejecting events with incidental tracks in the event.

With our level-two and level-three requirements, the efficiency of identifying a $W \rightarrow e\nu$ decay where the electron has an $E_T \geq 20$ GeV in the central detector is greater than 99%. The purity of the sample is still too low to be useful for our W analysis; therefore, we need to employ a series of analysis cuts designed to enhance the component of electrons which come from $W \rightarrow e\nu$ decays.

3.2.2 Electron Quality Cuts

The electron trigger sample is reprocessed with offline reconstruction code. The reconstruction code utilizes the best calibration constants which are available only after a run has terminated. After reconstruction we apply the tight central electron selection cuts [17]. The list that follows details this selection.

Central: The allowed η range of the EM energy is $\pm$ 1.1 which is determined by the central electromagnetic calorimeter coverage. Limiting the pseudorapidity range of the electron allows precise electron energy measurements and low background contamination but this requirement costs about 45% of the $W \rightarrow e\nu$ events.

Fiducial: We restrict electrons to be in well-instrumented regions of the central electromagnetic calorimeters (CEM). The electron must be at least 3 cm from the edge of a wedge in order to obtain precise energy measurement. Towers with known problems are excluded from consideration. There are gaps due to the ϕ segmentation of the calorimeter and the CEM contains a gap where the east and west sides meet ($\eta = 0.0$). The percentage area of the CEM suitable for precision EM energy measurements is 75%.

High electron E_T: The corrected electron transverse energy is calculated offline for all known detector degradation. We apply an E_T cut of 20.0 GeV which is greater than the trigger requirement (18.0 GeV) to remove any threshold effects. About 15% of central electrons from W decay have a E_T less than 20.0 GeV.

The cuts described above represent geometric and kinematic cuts on the electron energy. The following cuts are predominately quality variables designed to discriminate between electron and non-electron energy depositions. The total efficiency of the remaining cuts is about 85% yet they reduce the number of events by about 90%.

Isolation (ISO): An effective electron quality cut we use is the requirement that the electromagnetic energy be physically separated from other energy in the detector. The isolation is defined as the ratio of all non-electron energy in a cone of 0.4 around the electron to the electron energy.

$$ISO = \frac{E_T(0.4) - E_T(electron)}{E_T(electron)}$$

A cone is defined by the center of the electron energy deposition and a maximum

radius ($R = (\Delta\eta^2 + \Delta\phi^2)^{1/2}$) in which we look for non-electron energy. Non-electron energy includes both hadronic and electromagnetic calorimetry energy that is not contained in the electron tower(s). The non-electron energy is required to be no more than 10% of the electron energy (ISO $\leq$ .1). The Isolation cut reduces the background from electron-like jets.

Hadron Fraction (Had/EM): To further suppress jet contamination we check the hadronic calorimeter towers that are behind the electromagnetic towers that contain the electron's energy. Leakage of the electrons energy into the hadronic towers is a function of the electrons energy. We limit the ratio of hadronic over electromagnetic energy by the formula

$$Had/EM = 0.055 + 0.00045 * E_{ele}$$

where the units for E_{ele} are in GeV.

L share: The electron's energy is generally spread over more than one tower. The L_{share} variable compares the expected and measured lateral leakage from the electron seed tower to the adjacent towers. The formula

$$L_{share} = 0.14 \sum \frac{E_i^{adj} - E_i^{prob}}{\sqrt{.14^2 \cdot E + (\Delta E_i^{prob})^2}}$$

defines the lateral sharing. The sum is over the two adjacent towers in the same wedge as the seed tower. E_i^{adj} and E_i^{prob} are the measured and expected energy in the adjacent towers. The denominator is the espected error for $E_i^{adj} - E_i^{prob}$ where $0.14 \cdot sqrt(E)$ is the error on the measured energy and ΔE_i^{prob} is the error on the expected energy. The energy units are GeV.

L_{share} is required to be less than 0.2.

High P_T: Electrons and photons have similar calorimetry signatures. A charged particle such as the electron however will ionize the tracking chamber gas allowing us

to distinguish an electron and photon. We require a track pointing to the EM energy deposit with a P_T of at least 13.0 GeV.

Strip Chamber Variables (χ^2_{str},Δx,Δz): The strip chamber (CES) embedded in the EM calorimeter provides a transverse profile of the electron shower at the expected shower maximum. The profile is compared to an expected electron profile shape which is determined from test beam data. The χ^2 of this shape comparison is used as a discrimination variable. The strip profile is also used to determine the position of the electron inside the calorimeter tower. The position resolution is 0.17 cm for a 50 GeV electron in the CES. CES position measurements are compared to those obtained from the track in the central tracking chamber. These are required to match within 1.5 cm in the $R \cdot \phi$ (Δx) direction and 3.0 cm in the z direction (Δz).

Energy Momentum Ratio (E/P): The ratio of energy and momentum of a relativistic electron is very close to one. We require the ratio of measured energy to measured momentum to be between 0.5 and 2.0. Figure 3.1 shows this ratio for our inclusive electron sample. The long tail on the high side is from low electron momentum measurements due to Bremsstrahlung of the electron.

Interaction Vertex (z_{vtx}): A W boson can be produced anywhere the proton and antiproton bunches overlap. Figure 3.1 shows the distribution in $z(cm)$ of the primary vertex. The 0 of the plot is the center of the detector. To keep the interaction inside the fiducial volume of the detector and to maintain the calorimeter's projective tower geometry we require the W boson interaction vertex to be within 60 cm of the center of the detector. Several vertices can be reconstructed for an event. To identify the W boson vertex we choose the vertex closest to the track of the electron from the W decay. In the rare event that no vertex is within 5 cm of the electron track we use the electron's track to determine the vertex.

Conversion Rejection: High energy photons converting to electron-positron

pairs can fake a W electron signal. We perform direct searches for evidence of photon conversion. Photon conversions can be directly reconstructed by identifying the decay vertex of a pair of oppositely charged tracks. Another effective method uses the VTX hit information. If the photon converts outside the radius of the vertex chamber there will be a deficit of wire hits in the VTX along the direction pointing to the CTC track. We require that the observed number of VTX hits be at least 20% of the expected number of hits when at least 8 wire hits are expected.

Z Boson Rejection: Z bosons which decay to electron-positron pairs will pass the electron selection as easily as electrons(positrons) from W boson decay. Therefore we must reject the $Z \rightarrow e^+e^-$ events by searching for them directly. Some care must be taken because we intend to identify jets in the W events and our Z identification should not strongly reject electron-jet combinations as being Z bosons thus biasing the sample against high jet multiplicity. The following Z identification cuts are applied to a second electron:

- Had/Em ≤ 0.125
- ISO(0.4) ≤ 0.1
- Central Detector: E_T (corrected) $\geq 20\ GeV$
- Plug Detector: E_T (corrected) $\geq 15\ GeV$
- Forward Detector: E_T (corrected) $\geq 10\ GeV$
- $76\ GeV/c^2 \leq M_{ee} \leq 106\ GeV/c^2$

M_{ee} is the electron-positron invariant mass.

Electron-Jet Separation ΔR_{ej}: Electron activity and high E_T jet activity are kept clearly separated in the analysis with an electron-jet separation requirement. We reject all events which have a jet centered at less than a radius R=0.52 in an η–ϕ cone around the electron.

Run Quality: Each run of the accelerator is required to meet a set of minimum quality conditions. The beam conditions must be stable and the integrated luminosity delivered must be greater than 1.0 nb^{-1}. All detectors must be operational and the solenoid ramped to the correct current. Temperatures, voltages, trigger rates and electronics are required to be within operational limits. Additionally, the validation group at CDF checks physics distributions for any anomalous behaviour that would indicate problems. We analyze only those runs which meet the run quality requirements for W,Z and top physics. We do analyze runs with known problems in the muon subsystems since we do not use these detectors.

The electron selection cuts are listed more concisely in table 3.1. We use a subset of the selection cuts to strip the electrons from the trigger sample and then the full selection to obtain our final electron sample. The loose and tight selection cuts are both listed in table 3.1 and the E_T distribution at both stages of selection are shown in figure 3.2. This plot shows the enhancement of the W electron E_T peak as additional W selection cuts are applied. Figure 3.4 shows the E_T distribution for those electrons which pass our initial selection and fail the final selection. The significant difference between the loose and tight cuts is that the isolation cut is applied as part of the tight selection. This cut strongly rejects electron-like jets from multijet events. The isolation variable will later be used to measure the residual contamination of the W sample by multijet events.

3.3 W Selection

So far we have used the final state electron of $W \rightarrow e\nu$ events to tag a W boson. Of the processes that contribute to the inclusive high E_T electron sample $W \rightarrow e\nu$ decay is unique for its single final state high E_T neutrino. The neutrino does not interact with the detector components therefore its presence must be determined indirectly

Table 3.1: List of quality cuts for $W \rightarrow e\nu$ selection.

CUT	loose	tight
Detector Region	Central	
fiducial volume	yes	
E_T(corrected)	$\geq 20\ GeV$	
ISO(0.4)	–	≤ 0.1
Had/Em	$\leq 0.055 + .00045E\ (GeV)$	
L_{shr}	≤ 0.2	
$P_T \geq$	$13\ GeV/c$	
$\lvert\Delta x\rvert$	≤ 3.0 cm	≤ 1.5 cm
$\lvert\Delta z\rvert$	≤ 5.0 cm	≤ 3.0 cm
χ^2_{str}	≤ 10.0	
E/p	≤ 3.0	≥ 0.5 and ≤ 2.0
$\lvert z\rvert$	–	≤ 60.0 cm
remove conversions	no	yes
require good run	no	yes

by considering energy-momentum constraints on the event. The momentum components of the final state particles transverse to the beam line should sum to zero because the initial state particles have essentially zero net transverse momentum. Since the neutrino deposits no energy in the detector the vector sum of the measured transverse energies will not sum to zero. We refer to this imbalance of transverse energy as missing transverse energy ($\not\!\!E_t$). We select high transverse energy neutrinos by requiring the $\not\!\!E_t$ to be large ($\geq 30\ GeV$). The details of the $\not\!\!E_t$ calculation along with Monte Carlo evaluations of the calculation are described in appendix A. Figure 3.3 shows the imbalance of transverse energy for our tight central electron sample and figure 3.2 shows the change in the electron E_T distribution after the $\not\!\!E_t$ cut is applied. Although $\not\!\!E_t$ requirement reduces the number of W bosons by 35% the purity of the final sample is 94%. We have 51431 events for our $W+$ jet analysis.

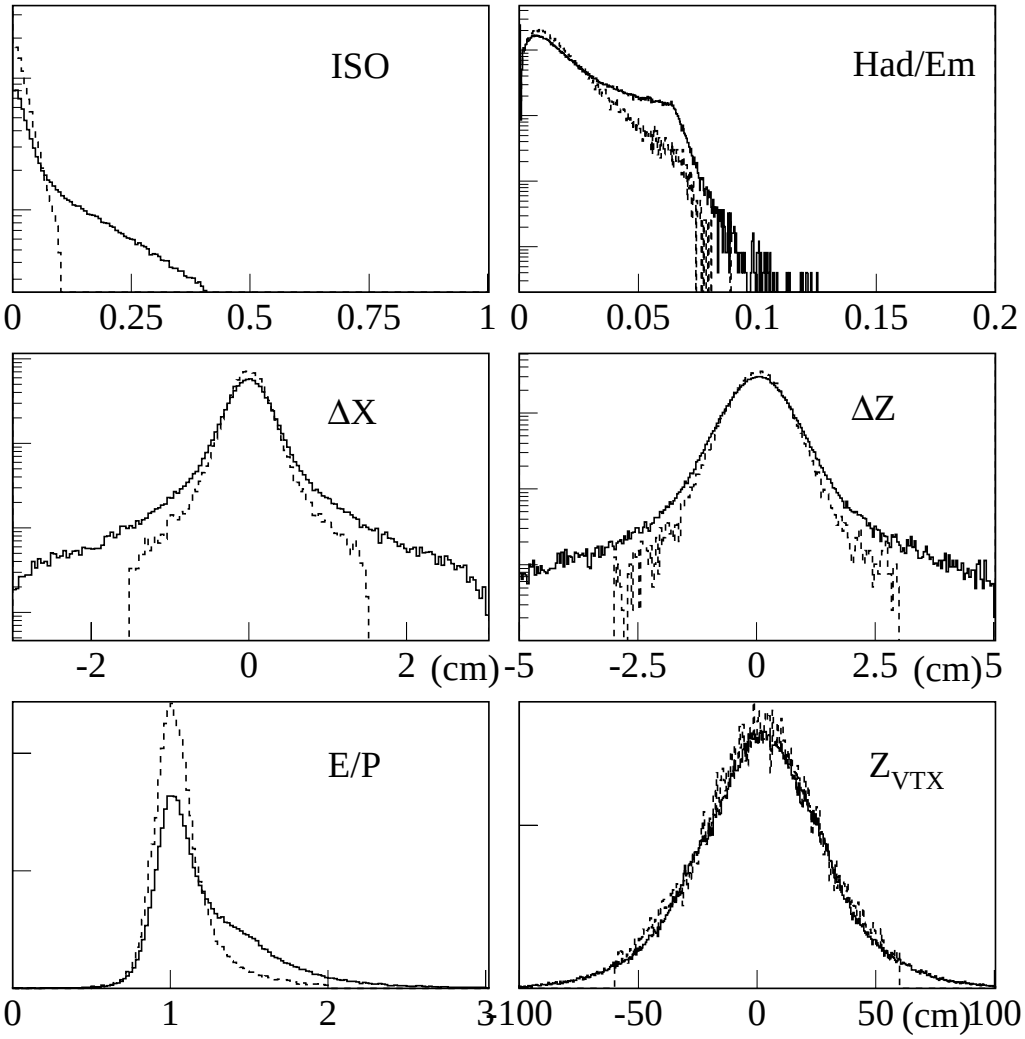

Figure 3.1: Distributions of some of the quality variables which are used to isolate high E_T central electrons that result from W decay. The solid histograms show the variables before the cuts are applied. The dashed histograms show the variables after full electron selection. The variables plotted are the following: electron isolation (Iso), hadronic over electromagnetic energy (Had/EM), CTC and CES matching in *local* x (Δx) and along z (Δz), electron energy divided by electron momentum (E/P) and the vertex distribution (z_{vtx}).

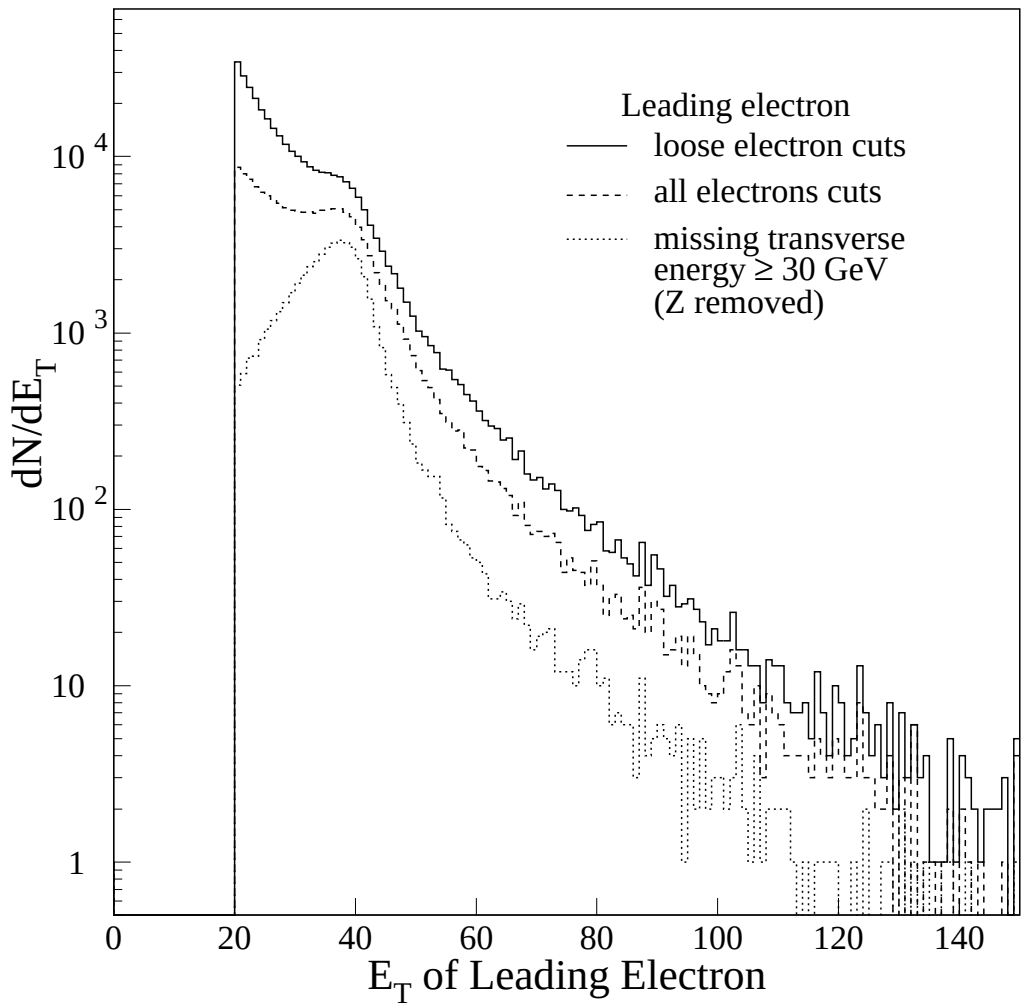

Figure 3.2: The plot shows the E_T distribution for the the events stripped with a subset of the electron selection cuts, full electron selection and our final W sample which includes a missing transverse energy ($\not\!\!E_t$) of at least 30 GeV.

3.4 Jet Selection

The cuts described above select a $W(e\nu)$ sample of 51431 events. We will divide this sample into subsamples according to the number of jets produced along with the W boson. The process of $W+$ jet production can be factored into two steps: (1) The production of $W+$ n partons where a parton is a gluon or quark, (2) the

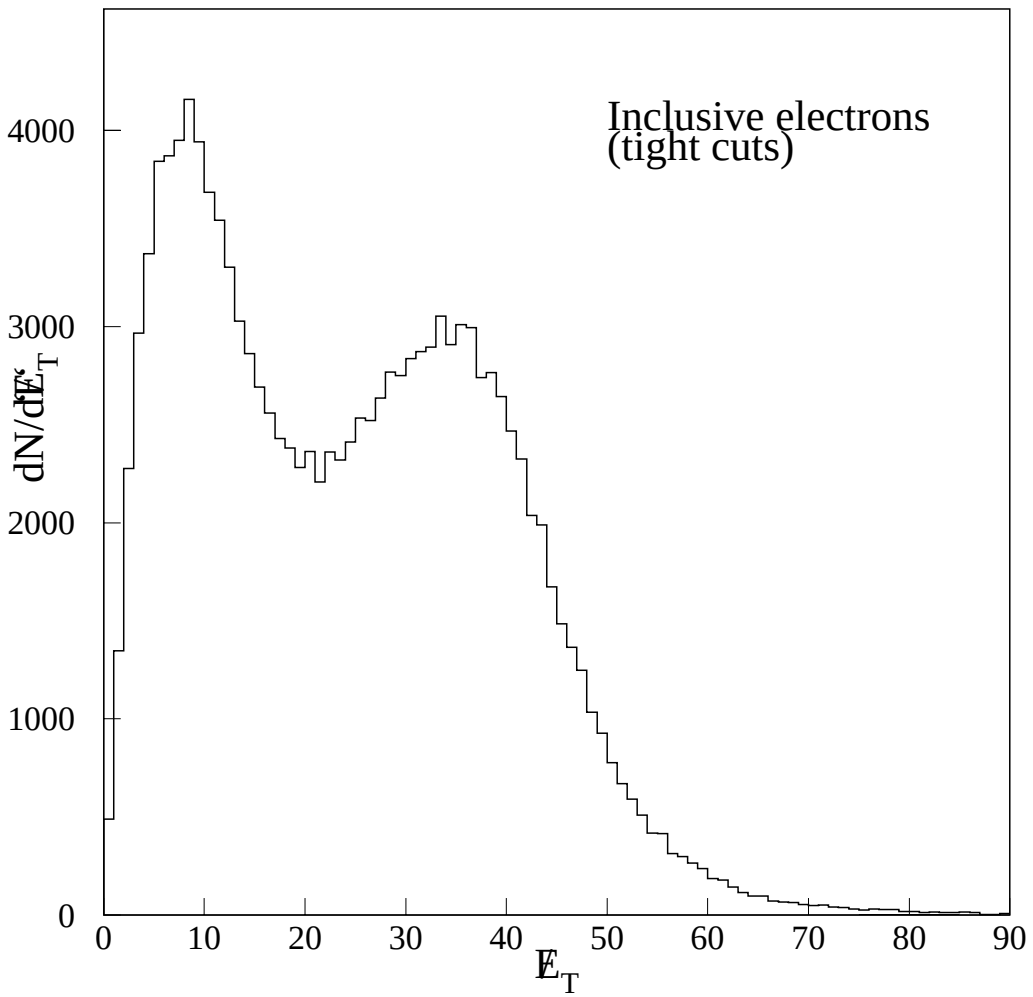

Figure 3.3: The plot shows the $\not\!\!E_t$ distribution for the inclusive electron sample. Noticeable is the W peak due to the escaped ν.

fragmentation and hadronization of the partons (quark/gluon $\rightarrow$ hadrons). The manifestation of high momentum parton production is therefore multiple hadrons in the detector which are generally clustered in a direction close to the direction of the parent-parton. The lego plot of figure 3.5 shows a hadronic cluster of energy in the calorimeter. The cylindrical calorimeter has been sliced at $\phi = 0$ and unfolded for this plot. The vertical axis represents the transverse energy per tower. The electron

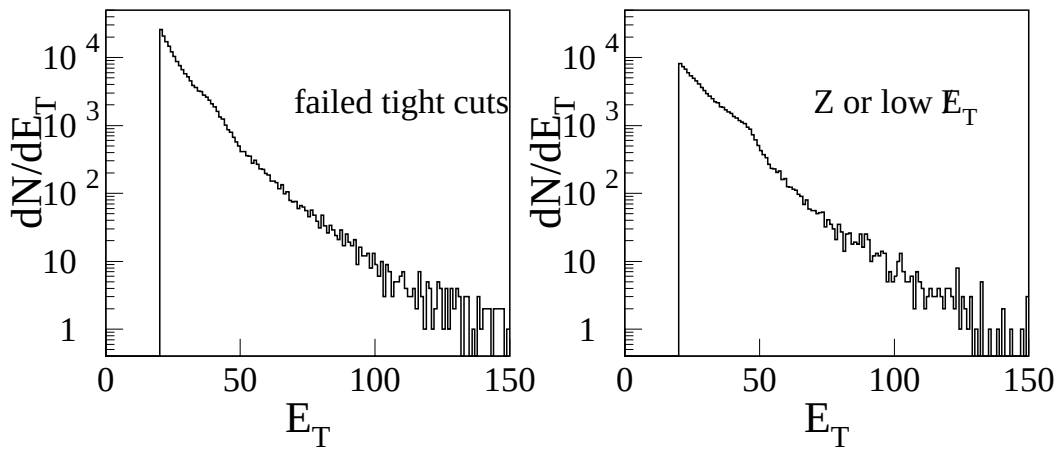

Figure 3.4: The left plot shows the electron E_T distribution for those events that pass the loose electron selection but fail tight electron cuts. The plot on the right is the electron E_T distribution for the events that pass the tight electron cuts but fail the $\not\!\!E_t$ cut or pass the Z cuts.

energy is shaded darker. The jet cluster is evident and we see that its calorimetry signature is distinct from that of the electron's. Since jet shapes and energies vary dramatically from jet to jet we must use a jet finding procedure capable of identifying all potential jet candidates.

3.4.1 Jet Clustering

We use a cone clustering algorithm for finding jets [18]. In this procedure we look for a seed tower around which to cluster. All calorimeter towers containing more than 1.0 GeV of transverse energy are seed towers. We search in a cone R=$(\Delta\phi^2 + \Delta\eta^2)^{1/2}$ around the seed tower and add any towers with an E_T more than 0.1 GeV. If the individual seed towers are closer than the cone radius they are merged. Thus several iterations are necessary before a stable set of clusters is found. On each iteration the centroids of the clusters are recalculated and used as the center of the cone for the next iteration.

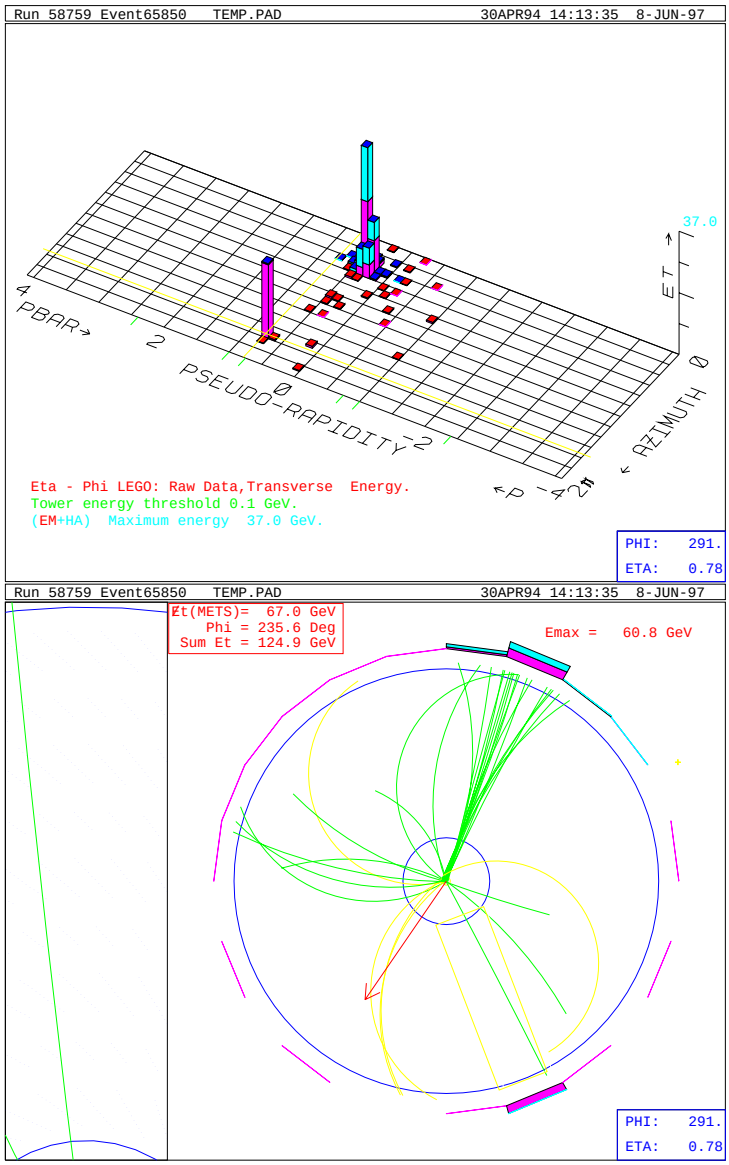

Figure 3.5: The upper plot shows the energy deposited into the calorimeter from a $W+$ 1 jet event. The electron is located at $\phi = 291$ and $\eta = 0.78$. The other tower cluster contains the jet's energy deposited in the electromagnetic calorimeter (dark shade) and the hadronic calorimeter (light shaded). The lower plot shows a view of the central tracking chamber. The beam line is perpendicular to the page. The track cluster associated with the calorimeter cluster is evident. The electron track is located in the dotted rectangle. A superimposed arrow indicates the direction of the missing transverse energy.

We use a cone radius of 0.4 for the clustering algorithm. This choice is small enough for counting jets and is less susceptible to energy contamination from outside the jet as we discuss later. We also make two modifications to the standard clustering

procedure. We remove the electron's energy from the towers before clustering, since the jet clustering procedure will identify electrons as jets. This electron suppression allows energy near the electron to be contained in the appropriate jet cluster. Secondly, we redefine the clustering vertex as the W boson vertex if a discrepancy exists so that all transverse energy in the event is calculated from the W vertex.

3.4.2 Jet Corrections

The above procedure defines a jet as the energy in a cluster of towers within a particular radius. To obtain the parent-parton energy we must correct this energy for several effects.

1. Correction for the energy response of the calorimeter.
2. Correction for energy deposited inside the 0.4 cone from sources other than the parent-parton.
3. Correction for parent-parton energy which radiates out of the 0.4 cone.

These corrections are standard CDF jet correction procedures which are fully described elsewhere ([19],[20],[21]). We give brief descriptions of these corrections in the following paragraphs.

The first correction listed above is designed to obtain the true energy inside the clustering radius. This is achieved in two steps. First, the energy of jets in the plug and forward calorimeters are scaled to give the energy as it would be measured in the central calorimeter. The correction is derived from a sample of jet events containing one well-measured central jet and a second jet which can be anywhere in the detector. The relative jet function ($R(P_T, \eta)$) that is derived from this sample, corrects the imbalance of the two jets as a function of the P_T and η of the second jet. After jet energy is scaled to the central detector it is corrected for the response

of the central detector. The result of these two steps is the true energy inside the 0.4 cone.

All energy inside the cone does not necessarily originate from the parent-parton. There are two contributions of cone energy contamination. First, underlying event energy from the spectator partons of the hard interaction is subtracted. The average contamination is 1.01 GeV. The second source of contamination of jet cone energy is energy deposited into the cone from interactions other than the W boson interaction. To obtain the contamination from interactions that occur in the same $\overline{p}p$ crossing as the W boson event we would like to have a sample selected from a completely unbiased trigger, alternatively known as a crossing trigger sample. A crossing trigger accepts all $\overline{p}p$ crossings as physics events and is representative of the extra interactions in W events since there is no significant selection bias for or against W events with extra interactions. The actual sample used to determine the contamination from extra interactions is a minimum-bias sample which is approximately a crossing trigger sample minus the zero interaction events. The energy in minimum-bias events is examined to see how much energy from these events would accidentally overlap with a jet cluster in a hard physics event. The method employed was the random cone method which randomly checked calorimeter towers of minimum-bias events to see the energy contained in a cone of 0.4. The amount of energy was parameterized by the number of reconstructed vertices in the event. The average contamination of 0.4 cones was found to be 0.297 GeV for each vertex [22]. For each vertex reconstructed in a W event in addition to the W vertex this amount of energy is subtracted from each jet in the event. The uncertainty that we assign to the extra interaction energy and the underlying event energy is 50% as determined by a detailed examination of the random cone method [21].

The description of the corrections thus far is expressed mathematically as

$$P_T{}' = A(R(P_T, \eta) \cdot P_T - n_{vtx} \cdot b) - 1.6 \cdot a$$

where

P_T = jet transverse energy

η = jet detector pseudorapidity

$R()$ = relative jet corrections

n_{vtx} = number of extra vertices

b = average energy contributed to jet cone per vertex.

$A()$ = absolute energy scale correction

a = average energy contributed from the primary interaction and extra interactions with no reconstructed vertex. The factor of 1.6 corrects for detector response since this energy is subtracted after the absolute correction.

The final correction to the jet increases the jet cone energy for energy that falls outside the 0.4 cone. This out–of–cone correction accounts for energy that radiates from the parent parton at a large angle. The correction is parameterized by the the jets transverse momentum because jets become narrower at large energies. The out–of–cone correction is given by

$$P_T{}'' = P_T{}' + a \cdot (1 - b \cdot \exp -c \cdot * P_T{}')$$

$$a = 22.999, b = 0.915, c = 0.00740$$

The combined corrections to the jets raise the measured cluster energy about 60% at E_T =15 GeV. The error on the jet energy is 5.0% [23] at E_T =15 GeV. This value excludes the contribution to the error due to the uncertainty on the underlying event and extra interaction energy. These uncertainties contribute 3.3% additional error to the jet energy.

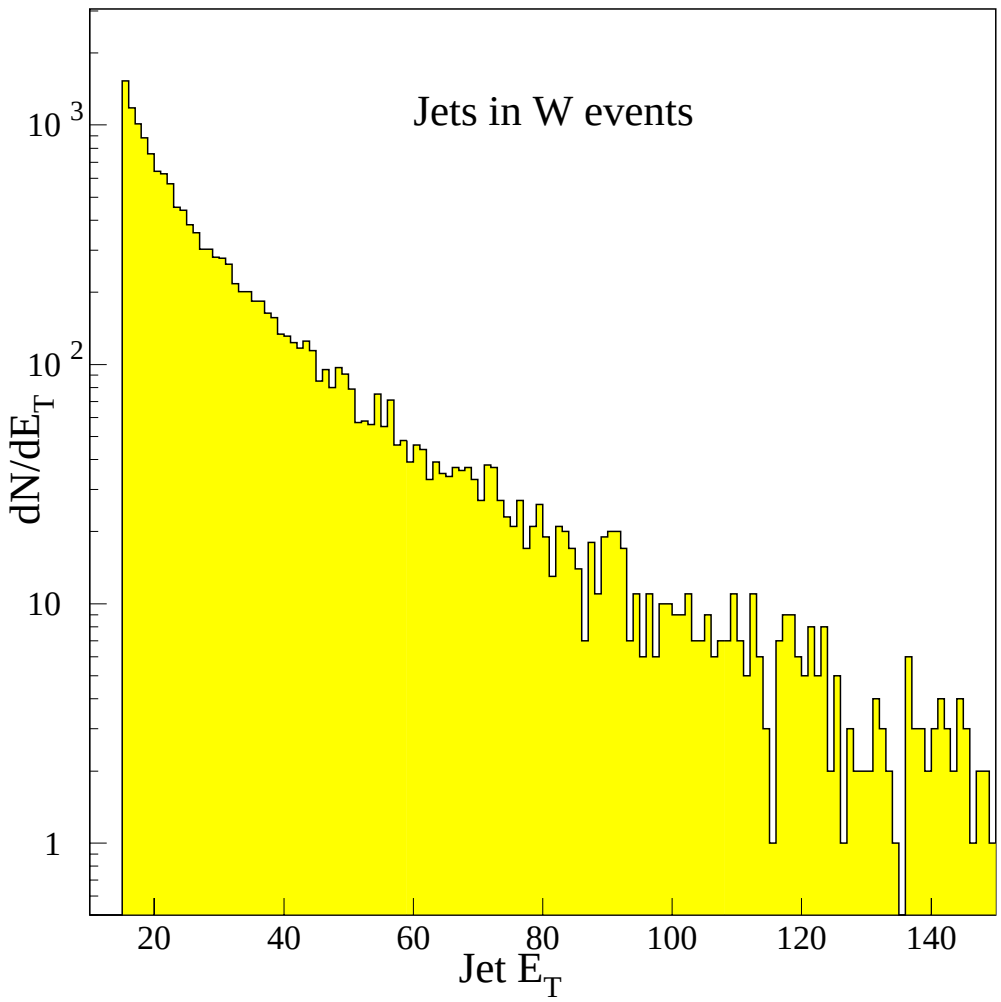

Figure 3.6: The E_T distribution for all jets in th W sample with a $E_T \geq 15\ GeV$.

3.4.3 Jet Counting

We count jets in W events using the following definition:

- jet $E_T \geq 15\ GeV$
- jet $|\eta_{det}| \leq 2.4$.

We first consider all clusters with a E_T above 12 GeV as potential jets. If two jets are within a radius of 0.52 ($1.3 \cdot \Delta R_{jet-jet}$) we merge these jets into one and recalculate their energy. The factor of 1.3 represents a jet separation resolution criteria. The η_{det} cut (2.4) is the jet η as measured from the center of the detector. This cut limits us to the region of the calorimeter where the energy corrections are best understood. The jet transverse energy cut is chosen to keep us in an energy region where the jet energy scale is well known. We find a total of 14472 jets in the W sample. The breakdown according to the number of jets in an event is give in table 3.2.

The error on the jet energy is the largest source of error in counting jets since the the E_T distribution of jets is a steeply falling distribution (figure 3.6). We present the error on the the $W+$ jet cross section measurements due to the error on counting jets in chapter 6. The jet counting uncertainties are derived from the 5% jet E_T uncertainty, 3.3% underlying event and extra interaction uncertainty, and the $\pm$ 0.2 uncertainty on the jet η_{det}. The energy errors are with respect to a jet at E_T =15 GeV.

Table 3.2: Jet Multiplicities Associated with W Production

Sample	N_W	Fraction
$W + 0$ jets	40287	0.7833
$W + 1$ jets	8548	0.1662
$W + 2$ jets	2016	0.0392
$W + 3$ jets	454	0.0088
$W + 4$ jets	105	0.0020
$W + 5$ jets	16	0.0003
$W + 6$ jets	5	0.0001
Total	51431	1.0000

3.5 Chapter Summary

We have selected W bosons from $\sqrt{s} = 1.8\ TeV\ \overline{p}p$ collisions. The $W \rightarrow e\nu$ decay of the boson provides high E_T electron and neutrino pair which is easily distinguished from other inclusive electron processes. We used EM energy depositions in the central calorimeter for defining an inclusive electron sample. Discrimination variables and other event quality cuts were used to enhance the purity of the W boson events. Events with a high E_T neutrino were selected from these by requiring a large imbalance of transverse energy. Our final W event sample consists 51431 events which is about 19% of the total $W \rightarrow e\nu$ events produced at CDF. The energy of hadronic clusters in the W boson events were corrected back to the parent parton through standard CDF jet correction procedures. We counted jets with $E_T \geq 15\ GeV$ and $|\eta_{detector}| \leq 2.4$. The W events were divided according to the number of jets produced with the W boson. Each sample will be corrected for background contamination and for the W boson efficiency in order to obtain the cross sections as function of the number of jets.

Chapter 4

Backgrounds to $W \rightarrow e\nu + \geq n$ Jets

4.1 Introduction

In chapter 3 we described the selection of $W \rightarrow e\nu$ events and defined a jet for the purposes of counting the number of jets in a W event. This chapter and the following will describe corrections to these raw numbers of $W+$ n jet candidates in order to obtain the production rates of direct single W's produced in association with n jets. As defined in chapter 1, direct single W production refers to a single W produced from a $q\overline{q}$ annihilation. Direct single W production dominates our $W+$ jet samples; however, other production processes will contribute a significant fraction of events to our samples.

The standard model predicts that the top quark will decay almost exclusively to a final state containing a W boson and a b quark. The final state of a top pair ($t\overline{t}$) decay in which one top decays to an $e\nu$ typically includes at least 2 jets and more likely 4 jets so that the contribution to our high multiplicity W samples is significant. Although top decay is a source of true W bosons we subtract its contribution from our data as though it were a background in order to make comparisons with predictions for direct single W production.

True background events are those events which do not contain a $W \rightarrow e\nu$ decay yet leave a $W \rightarrow e\nu$ signature in the detector. The list of significant backgrounds is multijet events, $W \rightarrow \tau\nu$ and $Z \rightarrow e^+e^-$. The largest of these contaminations is multijet events which refers to direct QCD production of jets. These events have a small probability that the jet will produce an electron signature and that the event will simultaneously contain a large imbalance of transverse energy. However,

since the production rate for multijets is much larger than W production even a small probability results in significant background rates. We use a sample of events enriched in QCD multijet events to estimate the contribution from this background.

The remaining backgrounds from $W \to \tau\nu$ decay and $Z \to e^+e^-$ decay contribute a small but significant number of events to our W candidate samples. $W \to \tau\nu$ events are produced at the same rate as $W \to e\nu$ and 18% of the τ leptons decay to a final state electron. This potentially serious background is strongly rejected by the high transverse energy requirements on the electron and neutrino. An electron from $Z \to e^+e^-$ decay passes our electron E_T requirement as easily as electrons from W decay so that we rely primarily on the $\not{E}_t$ requirement to reject these events. A $Z \to e^+e^-$ decay can achieve a large missing transverse energy if one of the leptons escapes the detector through an uninstrumented region. We use a detector simulation to obtain the fraction of $Z \to e^+e^-$ events for which one lepton passes the electron selection and the other escapes or is mis-measured enough to produce a large imbalance of transverse energy.

We subtract the backgrounds mentioned above from the total number of W events in our samples. We also correct for a special type of background which does not increase the total number of W's but does add to the number of jets in a W event. We refer to these backgrounds as *promotion* backgrounds because they promote a W event with n jets to a W event with $n + m$ jets. An example of a promotion is a jet produced by an extra interaction. Since we do not distinguish from which vertex a jet is produced we will count all jets as produced from the W interaction and correct our counts later. Although the probability for a promotion is very small the effect is enhanced by the fact that the higher jet multiplicity rates are being fed by the lower multiplicity channels which have much larger production rates.

4.2 Top

4.2.1 Source of Top Contribution

The $W+$ jet sample was used to establish the existence of the top quark at CDF [2]. Both top and its antiparticle from top pair production will decay to a W boson and a b quark. The top discovery analyses achieved a sample enriched in top events by identifying the leptonic decays of W's and further enriching the sample by identifying events which contain b quarks. Although, our W samples are not required to contain b quarks; the fraction of top events is expected to be significant in the subsamples with a high number of jets.

Since our W data selection requires an electron and neutrino, one of the W's from top pair decay is constrained to this decay mode. The other W is allowed to decay to any mode but it is the hadronic decay ($W \rightarrow q\overline{q'} \rightarrow$ hadrons) that introduces the largest contamination of our direct single W candidate sample. We refer to the mode in which the second W decays hadronically as the electron-jet mode. There are two reasons why the electron-jet mode produces the largest contamination. The branching ratio of the W to jets is 70% and the total number of jets in this mode is 4 jets which places these events in the subsamples of the $W+$ jet events where the direct single W production rate is small.

The total number of top pairs produced during data collection is roughly 600 where we have used the theoretical cross section of 5.53 pb [24]. The branching ratio to a final state with an electron, neutrino and 4 jets is 14.5% (table 4.1) which gives 87 $W+$ 4 jet events from top pair decay. The efficiency for finding a $W \rightarrow e\nu$ decay given our W selection cuts is approximately 20% (next chapter). Therefore a rough estimate of the contribution to the $W+ \geq 4$ jet sample is 17 out of 126 events. As we shall see later the other backgrounds to the $W+$ 4 jet sample total 46 events so

that the top contribution represents over 20% of the true $W \rightarrow e\nu$ events with 4 or more jets. An accurate calculation will include jet counting efficiencies as well the difference in the efficiency for finding W's produced from top.

Table 4.1: The branching fractions for final states from $t\overline{t}$ decay. The final states with 4 jets are contributed primarily from the decays listed in the upper right and lower left corners.

Decay of *top*		$\overline{t} \rightarrow W^- \overline{b}$			
		$e^-\nu\ \overline{b}$	$\mu^-\nu\ \overline{b}$	$\tau^-\nu\ \overline{b}$	$q\overline{q}\ \overline{b}$
$t \rightarrow W^+\ b$	$e^+\overline{\nu}\ b$	.012	.012	.012	.073
	$\mu^+\overline{\nu}\ b$	.012	.012	.012	.073
	$\tau^+\overline{\nu}\ b$	.012	.012	.012	.073
	$q\overline{q}\ b$	.073	.073	.073	.460

4.2.2 Top Calculation

Our official top contribution estimate is derived from a top Monte Carlo sample defined by

- the PYTHIA top event generator
- all decay modes allowed
- full detector simulation
- top mass of 170 GeV/c^2

PYTHIA [25] generates and decays top pairs for 1.8 TeV $\overline{p}p$ collisions. The W bosons from top decay are allowed to decay to any final state in order to obtain every possible background event. The complete list of final states are listed in table 4.1 with the branching ratios included.

The output from the generator is processed with a full detector simulation so that the efficiencies for finding W's and counting jets are modeled. A detector simulation

also models the effect of a second electron or a τ faking a jet when the second W decays leptonically. The output from the detector simulation is in an identical format as data and we process the Monte Carlo events with the identical executable that is used to identify W events in our data sample.

There are 42000 top events generated (N_{gen}) for our calculation [1]. Of these, 2596 events pass our W selection. The breakdown according to the number of jets reconstructed is presented in table 4.2.

In order to extract a top expectation for our W analysis we must know the top mass, the top cross section at the mass of the top and the luminosity of our data sample. The top sample was generated at a mass of 170 GeV. The latest top mass measurements at CDF [3] yield a value of $176.8 \pm 6.5\ GeV/c^2$. We correct our sample for the decrease in the cross section from a mass of 170 GeV/c^2 to 175 GeV/c^2. The luminosity of our top Monte Carlo is then calculated with

$$L_{gen} = \frac{N_{gen}}{\sigma_{t\bar{t}}\ (175)} = 7.6\ fb^{-1} \tag{4.1}$$

this value is used to scale the numbers in table 4.2 to our data luminosity of 108 pb^{-1}. The expected top contribution as a function of the number of jets is presented in table 4.2.

4.2.3 Top Systematic Error

The systematic error on our top expectation includes the uncertainty of $t\bar{t}$ production rate due to the error on the luminosity of our W data sample ($108 \pm 9\ pb^{-1}$), the theoretical error on the top cross section ($\sigma_{t\bar{t}}\ (175) = 5.53 + .07 - .39\ pb$) and the error on the top mass as measured at CDF ($176.8 \pm 6.5\ GeV/c^2$). The top cross

[1] We thank the top analysis group for providing this Monte Carlo sample

Table 4.2: Results of top background calculation. The first column lists the number of $W+ \geq n$ jet events selected from the 42000 top events generated. The second column gives the expected contribution to our data samples from top pair production and decay. The first error is statistical and the second is the systematic which is the sum of the top mass uncertainty, the luminosity uncertainty, and the theoretical uncertainty on the top cross section.

Sample	Number Selected	Background Expected (stat and syst)
≥ 0 jets	2596	$36.87 \pm 0.71 + 7.31 - 7.28$
≥ 1 jets	2595	$36.85 \pm 0.71 + 7.31 - 7.28$
≥ 2 jets	2548	$36.18 \pm 0.70 + 7.18 - 7.15$
≥ 3 jets	2173	$30.86 \pm 0.65 + 6.12 - 6.09$
≥ 4 jets	1481	$21.03 \pm 0.54 + 4.17 - 4.15$

section at masses of 170.3 and 183.3 GeV/c^2 are 6.35 pb^{-1} and 4.61 pb^{-1} respectively. This variation dominates the systematic errors in table 4.2.

4.3 QCD Backgrounds to $W + \geq n$ Jets

4.3.1 Sources of QCD Background

The backgrounds to $W \rightarrow e\nu$ come from any process which produces an electron-like energy deposition plus a large missing transverse energy. Multijet events, which we refer to as QCD background, can achieve this signature if one jet leaves an electron signature in the detector and the transverse energy in the event is not well measured. In fact, QCD background is the largest source of background to the $W+$ jet events. Furthermore the rate is dependent on the number of jets so that systematic errors in the background estimates do not completely cancel in the relative $W+$ n jet cross sections which we use to determine the absolute cross sections. To keep the error on our cross section due to background subtraction comparable to the statistical uncertainty of our $W+$ $n \geq 4$ jet sample, we need to know the QCD background to $\approx 35\%$.

Our identification of a W electron includes the use of both tracking and calorimetry information. To fake a W electron, a jet in a multijet event must leave a high P_T track in the CTC in addition to an electromagnetic energy deposition associated with this track. This dual tracking-calorimeter signature can be produced from hadron jets through several modes. Heavy flavor jets where charm or bottom quarks decay to real electrons can leave an electron signature in the detector. Gammas, converting to electron positron pairs, are a source of W background. Also included in the conversion electron sources are Dalitz pairs. Finally, π^0- $\pi^\pm$ overlaps and hadronic jets which shower early in the calorimeter can leave a well-isolated EM energy deposit with associated tracks.

In addition to producing an electron signal, the multijet background event must have a large missing transverse energy. Large missing transverse energy in a multijet event can be attributed to the escape of a jet through a crack or to the mismeasurement of an energy cluster.

4.3.2 Datasets for QCD Background Calculation

In order to obtain the QCD background we need to define a sample of events enriched in QCD multijets. In our selection of W events we used the electron isolation variable (chapter 5) to discriminate between electrons and jets. We also rejected a large amount of QCD background by requiring a large imbalance of transverse energy. Therefore to obtain a sample of QCD multijet events we remove these cuts from our W selection. Specifically, we select a QCD sample with the following criteria

- Apply all W selection cuts except:
  - Iso(0.4) ≤ 0.1
  - $\not\!\!E_t \geq 30\ GeV$

This sample contains 214046 events. Of course the W candidates are in this sample but they will be confined to one corner of the isolation-$\not\!\!E_t$ plane. A lego plot of isolation versus $\not\!\!E_t$ is shown in figure 4.1. From this figure we can easily distinguish the regions which are mostly W boson events (low isolation, high $\not\!\!E_t$) and mostly multijet events (everywhere else). The estimate of the QCD background will extrapolate from the multijet dominated regions to the W dominated regions.

Removing the isolation and $\not\!\!E_t$ cuts in the data selection also invites some contamination from electroweak processes such as $Z \rightarrow e^+e^-$and $W \rightarrow \tau\nu$ events. These will concentrate in the low isolation and low $\not\!\!E_t$ region of the isolation-$\not\!\!E_t$ plane. We employ a set of cuts to reject the electroweak contamination of these regions (described below).

4.3.3 Measurement of QCD Background

We use the isolation extrapolation method[26] to estimate the multijet background. The first step is to divide our QCD sample into 4 subsamples which are defined by their position in the isolation-$\not\!\!E_t$ plane (figure 4.1). We label the regions from a,b,c and d.

region a: $Iso < .1$; $\not\!\!E_t \ < 10$

region b: $Iso > .3$; $\not\!\!E_t \ < 10$

region c: $Iso > .3$; $\not\!\!E_t \ > 30$

region d: $Iso < .1$; $\not\!\!E_t \ > 30$

The number of events in each region is given in table 4.4. From the definitions of the regions above one sees that we have excluded intermediate regions from consideration. This exclusion is to insure that regions a, b and c are pure multijet and not

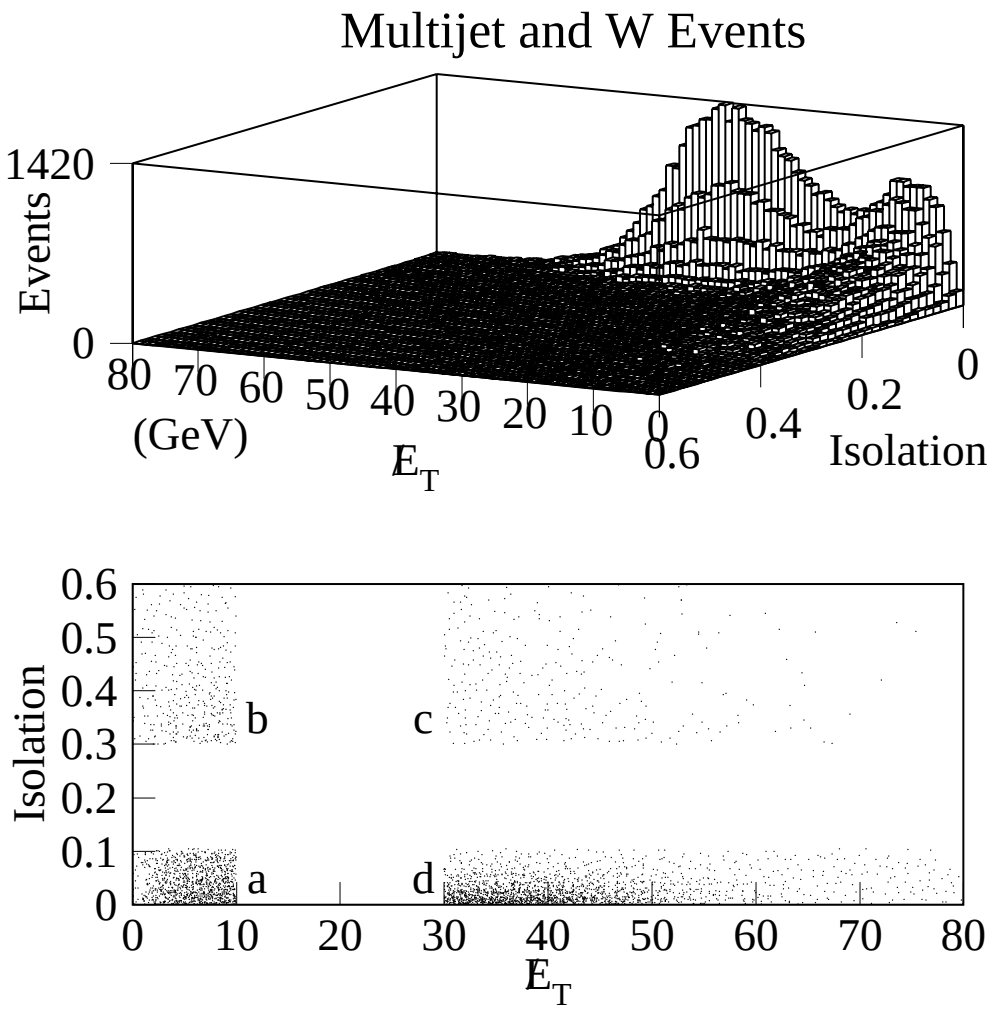

Figure 4.1: Isolation vs $\not{E}_t$ for the QCD sample. The bottom plot shows the 3 regions (a,b,and c) which are used to calculate the QCD events in region d where W bosons dominate. The characteristic $\not{E}_t$ distribution of $W \to e\nu$ events is evident in the lego plot (top). The QCD events have a $\not{E}_t$ distribution that peaks near 0 in this plot.

a mix of QCD and W events. We exclude events with an electron isolation in the region 0.1 to 0.3 and any events with a $\not{E}_t$ in the region 10 to 30 GeV [2].

We remove $Z \to e^+e^-$and Drell-Yan contamination by selecting events with a

[2]This cut rejects $W \to e\nu$ leakage as well as $W \to \tau\nu$ events which have an average $\not{E}_t$ less than $W \to e\nu$ events but generally larger than 10 GeV

second electron regardless of the mass of the electron-positron pair. However, if a second electron exists and is within a radius of 0.4 of the first electron the isolation of the two are correlated resulting in poor isolation of both electrons. The isolation of the first electron versus the second electron is shown in figure 4.2 for the QCD sample before any electroweak contamination is removed. We use an isolation variable defined by

$$ISO(0.4) = \frac{E_T(0.4\text{cone}) - E_T(\text{electron})}{E_T(\text{electron})}$$

If the e^+e^- pairs are close enough each appears in the isolation definition of the other. These events rarely allow the isolation of the first electron to pass our W selection; however, the spoiled isolation of the first electron also results in the failure of the e^+e^- removal cuts. Since these events do not contribute to W + jets yet do appear in the multijet background sample we must explicitly remove them from our multijet sample.

To enrich the sample further in multijet events we require that there is at least one other high energy cluster (besides the selected electron). The fraction of electromagnetic energy in this jet must be less than 0.8. This last selection criteria for a second energy cluster is only applied to the low $\not\!\!E_t$ events (regions a and b) where we expect all jets were measured reasonably well and therefore expect at least two high E_T jets.

A first order description of the isolation extrapolation method assumes the isolation shape for QCD jets faking electrons is independent of $\not\!\!E_t$ of the sample (see figure 4.3). Therefore, if the ratio ($\frac{N_a}{N_b}$) of well-isolated to poorly-isolated QCD events is known for the low $\not\!\!E_t$ region then it is known in the high $\not\!\!E_t$ region. We directly count the number of multijet events (N_c) with poor isolation and large $\not\!\!E_t$. With these quantities the number of QCD background events in the W sample (N_{QCD}) is

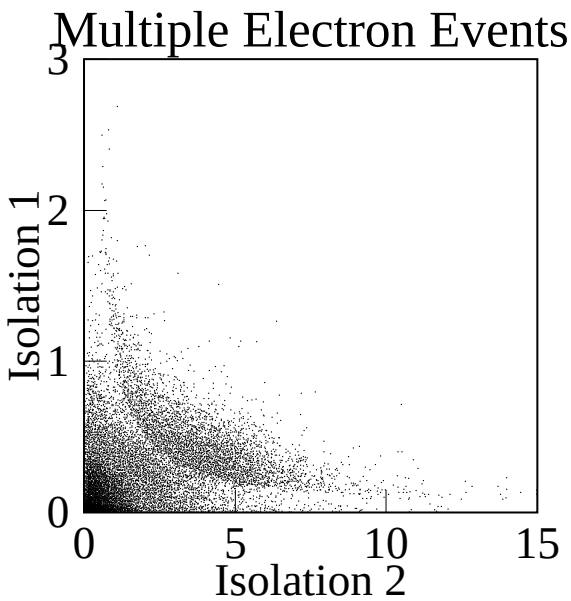

Figure 4.2: The isolation of electron 1 versus isolation of electron 2 for events with at least two electrons. The events that show the inverse relation between electron isolations are events where the two electron clusters are closer than the cone used to define the isolation. We remove these events from the QCD sample because they do not contaminate the W sample.

$$N_{\mathrm{QCD}} = \frac{N_a}{N_b} \cdot N_c \tag{4.2}$$

In reality, there may be some correlation between the $\not\!\!E_t$ of the event and isolation of the electron. To account for this correlation we follow past analyses in estimating the ratio $\frac{N_a}{N_b}$ with two low $\not\!\!E_t$ control samples. The first sample for the low $\not\!\!E_t$ region is required to have at least one other cluster (besides the QCD "electron") with an $E_T \geq 10\ GeV$. The second requires the cluster to have an $E_T \geq 20\ GeV$. The second sample is a subset of the first. Table 4.3 gives the number of events of the two samples for each multiplicity. Previous analyses used the control samples to establish an error on the QCD background estimate; however, we will assign an error based on

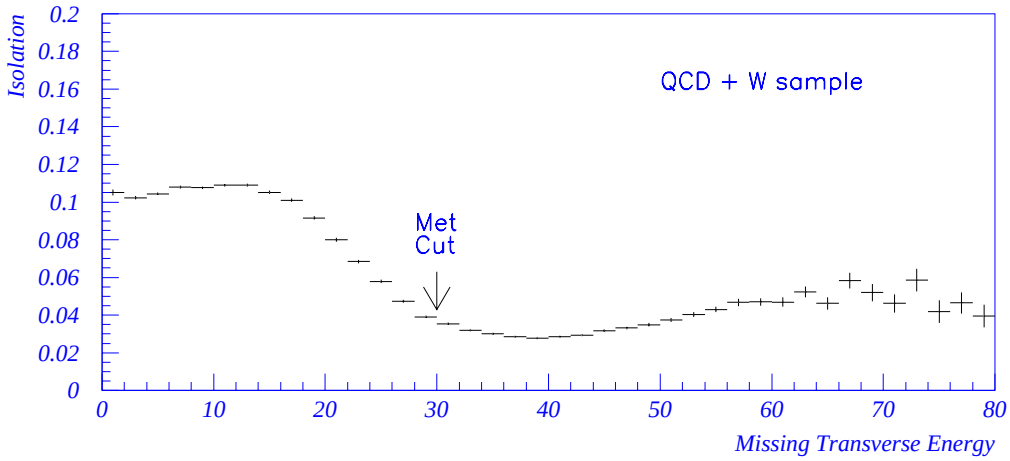

Figure 4.3: A profile plot of isolation versus missing transverse energy. The vertical axis shows the average isolation for events with a particular $\not\!\!E_t$ (horizontal axis). The high missing energy events show the low isolation characteristic of W electrons but significant QCD contamination is evident up to our $\not\!\!E_t$ cut of 30 GeV. The isolation of the low missing energy events are not completely independent of missing energy.

direct tests of the isolation extrapolation method.

Table 4.3: Number of events and the ratio ($\frac{N_a}{N_b}$) for the two control samples used in the QCD background calculation.

	Control Sample 1 $E_{T\,jet} \geq 10\ GeV$			Control Sample 2 $E_{T\,jet} \geq 20\ GeV$			
	Region a	Region b	$\frac{N_a}{N_b}$	Region a	Region b	$\frac{N_a}{N_b}$	$< \frac{N_a}{N_b} >$
≥ 0 jets	23540	6053	3.89	15158	4816	3.15	3.52
≥ 1 jets	19160	5453	3.51	14376	4553	3.16	3.34
≥ 2 jets	4100	1689	2.43	3311	1451	2.28	2.35
≥ 3 jets	798	333	2.40	717	306	2.34	2.37
≥ 4 jets	139	69	2.01	134	69	1.94	1.98

4.3.4 Tests of the QCD Background Calculation

The large statistics of the run 1 data sample allow direct tests of the isolation extrapolation method. For these tests we select two subsamples of the QCD sample. The low $\not\!\!E_t$ sample consists of all events with a $\not\!\!E_t$ less than 10 GeV. The anti-isolated

Table 4.4: Number of events with a poorly-isolated electron and high $\not\!\!E_t$ (region c) in the QCD sample.

Sample	Number of events
≥ 0 jets	429
≥ 1 jets	374
≥ 2 jets	175
≥ 3 jets	53
≥ 4 jets	17

sample is defined by an electron isolation greater than 0.3 . These two samples which are shown in figure 4.4 contain essentially no W events. To test the isolation extrapolation method we divide each of these samples into four regions just as we did with the QCD superset of events. Within each sample we can calculate the events in the new region d from the other three regions. We can also directly count the events since these are no longer dominated by W events. The calculations and observations are compared directly in table 4.5.

Table 4.5: Results for the tests of the QCD background calculation. The predicted number of events in region 4 and the observed number of events are compared. The first column lists the results for the low $\not\!\!E_t$ sample and the second column lists the results for the poor isolation sample. Both samples are essentially free of W contamination.

	Low $\not\!\!E_t$ Sample $\not\!\!E_t \leq 10\ GeV$		Anti-isolation sample Isolation $\geq .3$	
	Predicted	Observed	Predicted	Observed
≥ 0 jets	16522	15399	301	235
≥ 1 jets	13658	12480	263	198
≥ 2 jets	2782	2724	101	97
≥ 3 jets	569	543	29	29
≥ 4 jets	105	93	8.5	10

Overall, table 4.5 shows the method performs with the desired accuracy (35 %). We use the test from the anti-isolation sample to assign a systematic of 30 % to the

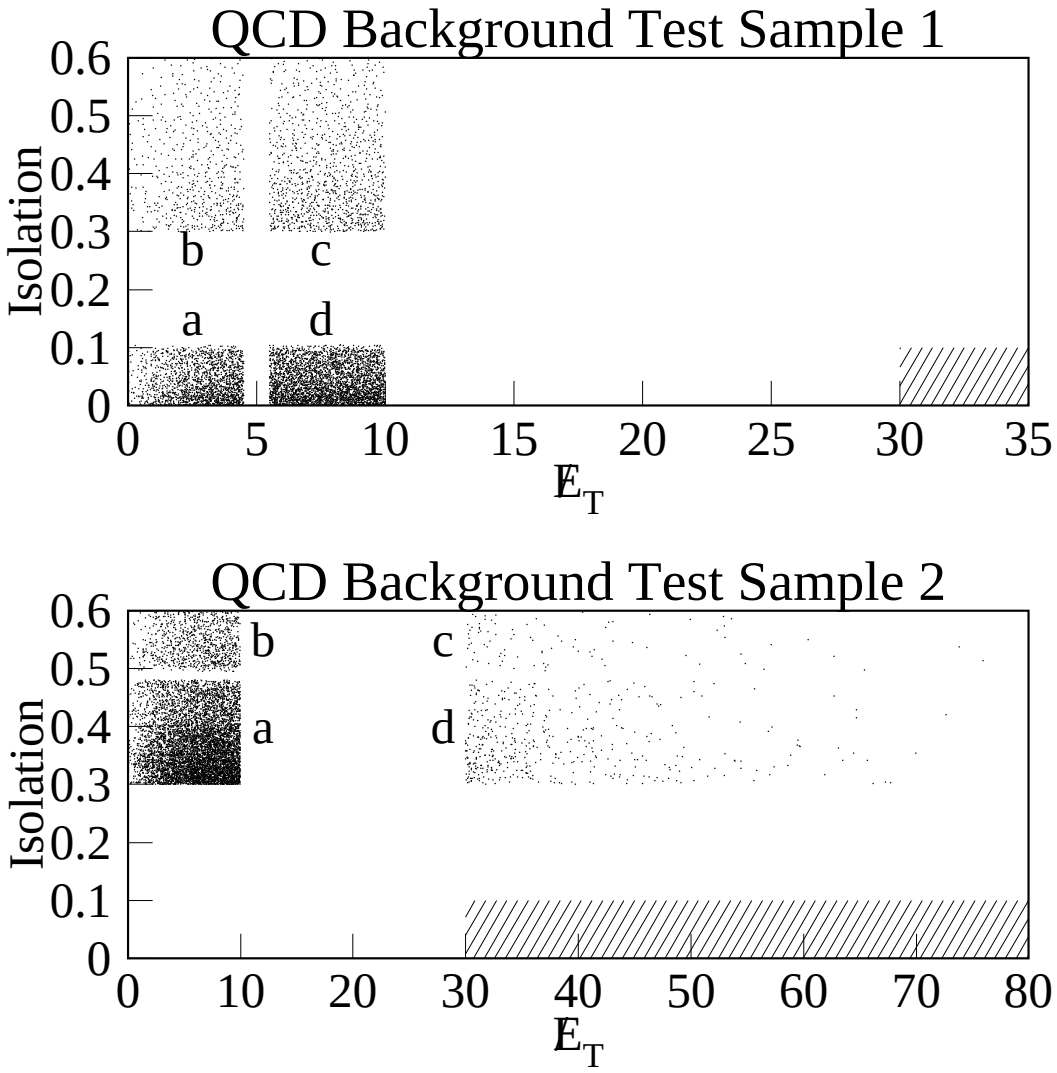

Figure 4.4: The plots show the subsamples of events in the isolation-$\not{E}_t$ plane which are used to test the QCD calculation. The upper plot is the subsample of QCD events with low $\not{E}_t$ sample. The lower is the subsample with a poorly-isolated electron. Each sample is divided into 4 regions to allow a calculation of the events in region d which is compared to the number of events (N_d) observed in the region. These samples are chosen to be displaced from the W dominant region (indicated by empty box).

QCD background calculation at each multiplicity.

4.3.5 QCD Background Results

Using the ratios listed in table 4.3 we calculate the QCD background for the $n \geq$ 0,1,2,3, and 4 jets samples of our W analysis. We see that the QCD contamination is significant and that the probability of contamination from multijet events increases with the number of jets in the $W+$ jet samples.

Table 4.6: Final results for QCD background. The first column is the number of W events selected with at least n jets. The second column presents the expected contamination of the W sample from QCD background. Statistical and systematic errors are shown.

	W Candidates	QCD Background
≥ 0 jets	51431	1509 ± 73(stat) ± 453(syst)
≥ 1 jets	11144	$1248 \pm 65 \pm 374$
≥ 2 jets	2596	$412 \pm 31 \pm 124$
≥ 3 jets	580	$125 \pm 17 \pm 38$
≥ 4 jets	126	$33.6 \pm 8.1 \pm 10.0$

4.4 Single Boson Backgrounds

4.4.1 Sources of Single Boson Background

W decay in which a final state electron results from an intermediate particle such as the τ can contribute to our $W \to e\nu +$ jet samples. $W \to \tau\nu$ accounts for one third of the leptonic W decays and the τ has a significant branching fraction (18%) to electrons. These events will sometimes be identified as $W \to e\nu$ decay [3]. However, the momentum of the τ is shared among three decay products ($e\nu\nu$), two of which do not deposit energy in the calorimeter. Our kinematic cuts reject most of the $W \to \tau\nu$ events.

[3] Muons have a 100% branching fraction to electrons; however, their long lifetime does not typically allow decay until they traverse the detector. Therefore, $W \to \mu\nu$ decay does not contribute as a background

An accurate estimate of the $W \rightarrow \tau\nu$ + jet contamination of our $W \rightarrow e\nu$ + jet samples is made using a LO QCD calculation for $W \rightarrow \tau\nu$ + jets events. The QCD production diagrams are the same whether the W decays to an electron or τ final state. We use this fact to remove the renormalization scale dependence inherent in LO QCD predictions. Rather than extracting an absolute prediction of the $W \rightarrow \tau\nu$ + $\geq n$ jet cross section, we extract the ratio

$$R_{W \rightarrow \tau\nu} = \frac{\sigma(W \rightarrow \tau\nu\ ) \cdot \epsilon(W \rightarrow \tau\nu\ )}{\sigma(W \rightarrow e\nu\ ) \cdot \epsilon(W \rightarrow e\nu\ )} \tag{4.3}$$

The ϵ in equation 4.3 is the efficiency for finding a W boson which is dependent on the decay mode. The ratio as calculated from equation 4.3 used with the counts in our W + jet data samples yields $W \rightarrow \tau\nu$ background.

Another significant source of high E_T electrons is produced from $Z \rightarrow e^+e^-$decays. The electron E_T spectrum is similar to that of electrons from $W \rightarrow e\nu$ but the Z cross section is a factor 10 below that of the W cross section. Although we have explicitly removed $Z \rightarrow e^+e^-$ decays from the W sample (chapter 3) the efficiency for our $Z \rightarrow e^+e^-$ identification was about 50%. A fraction of the Z's that failed the Z selection will contribute to our W events. If one lepton in the Z decay passes the electron selection and the other escapes through a gap in the detector coverage then a W signature can result.

Figure 4.5 shows the η distribution of the second electron for Monte Carlo Z events which pass Z selection. The gaps in the detector coverage are indicated by dips in the η distribution. We have also plotted the η distribution of the second electron in events which fail Z selection and have a large ($\geq 30\ GeV$) $\not{E}_t$. The peaks of this distribution correlate with the gaps in the detector which are seen in the first distribution. The calculation we use to estimate the rate of $Z \rightarrow e^+e^-$events faking $W \rightarrow e\nu$ is identical to the $W \rightarrow \tau\nu$ method described above.

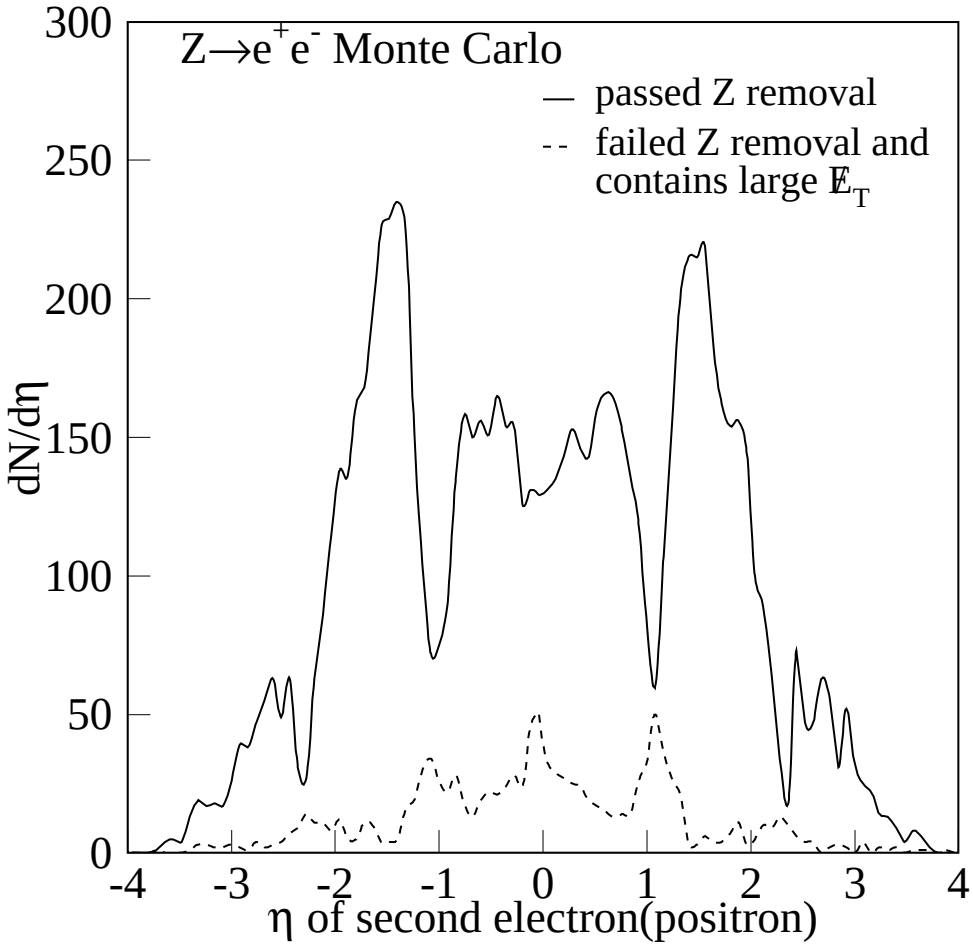

Figure 4.5: The η distribution of the second electron in a Monte Carlo simulation of $Z \to e^+e^-$events. The first electron is defined as the one that passes tight central electron cuts identical to the W selection. The solid line is the distribution for events which pass our Z removal cuts. We can see a loss of events near the η gaps in our detector. We have also plotted the η of the second electron (dashed) for events that fail our Z removal cuts and have a large $\not{E}_t$. The peaks in this distribution correlate with the dips of the other distribution.

4.4.2 Single Boson Background Samples and Results

We generate leading order $W \to \tau\nu + \geq n$ jet Monte Carlo samples using VECBOS.

The renormalization scale is $Q^2_{ren} = M^2_w$. We use HERWIG to add initial/final state

radiation and provide fragmentation of the partons with the HERWIG fragmentation scale (Q^2_{frg}) set equal to $M^2_w + P^2_t$. The program TAUOLA[27] is used to decay the τ to all allowed final states and provide the correct polarization. The Monte Carlo events are processed through the CDF detector simulation code (QFL) and our W selection executable is used to select events with the identical cuts used for data selection. A detailed description of the Monte Carlo generation is found in chapter 7.

For each $W \rightarrow \tau\nu + \geq n$ jet sample we create a $W \rightarrow e\nu + \geq n$ jet sample with identical generation parameters. The ratio in equation 4.3 is determined by the number of events passing our W selection cuts from both the $W \rightarrow \tau\nu$ and $W \rightarrow e\nu$ Monte Carlo samples. We use the following formulas to determine the backgrounds:

$$N_{W \rightarrow \tau\nu} = R_{W \rightarrow \tau\nu} \cdot N_{W \rightarrow e\nu} \tag{4.4}$$

$$N_{Z \rightarrow e^+e^-} = R_{Z \rightarrow e^+e^-} \cdot N_{W \rightarrow e\nu} \tag{4.5}$$

where

$$N_{W \rightarrow e\nu} = \frac{N_{Selected} - N_{QCD} - N_{top}}{(1 + R_{W \rightarrow \tau\nu} + R_{Z \rightarrow e^+e^-})} \tag{4.6}$$

These equations assume of course that no other contamination besides QCD and top exist in the W data. The results are shown in table 4.7 for $n = 1$ through 4. The results show that the contaminations from $W \rightarrow e\nu$ and $Z \rightarrow e^+e^-$ are small and will have a negligible effect on the relative cross section measurements. The asterisk identifies samples for which the calculation could not be performed. We extrapolated assuming a flat behavior. This extrapolation should be safe given the background is fairly insensitive to the number of jets but we have increased the error for these extrapolations by a factor 2.0.

Table 4.7: Expected background for $W \to \tau\nu$ and $Z \to e^+e^-$. Fractions are number of background over number of $W \to e\nu$.

	$W \to \tau\nu$		$Z \to e^+e^-$	
Sample	fraction	background	fraction	background
≥ 0 jets	0.0150	726	$--$	752(*)
≥ 1 jets	0.0217	196	0.0173	157
≥ 2 jets	0.0329	62.9	0.0137	26.3
≥ 3 jets	0.0213	7.87	0.0155	5.73
≥ 4 jets	0.0213	1.26(*)	0.0155	0.92(*)

4.5 Jet Multiplicity Promotions

4.5.1 Sources of Promotions

The previous sections discussed contributions to the W candidates selected for our $W+$ jet analysis. Here we discuss backgrounds which do not contribute to the total number of W events but rather add to the number of jets in a W boson event. We correct for two contributions of jets which do not arise from direct single $W+$ jet production.

- jets produced in interactions that occur in the same crossing as the W interaction
- γ's in $W\gamma$ events which are counted as jets

About 40% of our W events have at least one other vertex reconstructed in addition to the W boson vertex. The extra vertices indicate the presence of additional $\overline{p}p$ interactions. Typically these interactions contribute a small amount of energy which is spread over the detector. As we discussed in chapter 3 this energy is subtracted from our jet energy with a value determined by the number of extra vertices that we find in the W event. Occasionally the energy from an extra interaction will

be large enough and localized enough to result in a reconstructed jet. These jets will be counted along with any jets produced in association with the W boson.

4.5.2 Calculation of Promotions

The probability of a W event containing a jet that is generated from an extra interaction is 0.0099. This value was calculated from our minimum-bias events (see chapter 3, section 3.4.2 for the definition of this sample). The events in the minimum-bias sample closely model the extra interactions found in W events. Specifically, neither sample has a significant bias in triggering its acceptance. This is true for minimum-bias samples by design.

We counted the number of jets and the number of vertices in our minimum-bias sample. We found that for every 81 vertices in the minimum-bias sample, one single-jet event was found. The W sample contains 41188 vertices in addition to those vertices associated with the W bosons. We then expect 507 events with a single extra jet from an extra interaction in our W sample. This number of jets in 51431 W events yields the probability of 0.0099 for obtaining a single jet from an extra interaction per W event. The formula is shown explicitly in equation 4.7 below. In equation 4.7, $N_{\text{jet}}(\text{MB})$ is the number of jets in the minimum-bias sample, $N_{\text{vtx}}(\text{MB})$ is the number of vertices in the minimum-bias sample, $N_{\text{extra vtx}}(W)$ is the number of extra vertices found in the W sample, and P_1 is the probability for a jet to arise from an extra interaction in a W event. The calculation is repeated for the probability of obtaining 2, 3 and 4 jets from an extra interaction. The probabilities are listed in table 4.8 and are seen to drop by a factor 6 with the addition of each additional extra jet.

$$P_1 = \frac{N_{\text{extra vtx}}(W)}{51431} \cdot \frac{N_{\text{jet}}(\text{MB})}{N_{\text{vtx}}(\text{MB})} \tag{4.7}$$

So far we have shown that the probability for obtaining a jet from an extra interaction is less than a percent so why are we correcting for this? Consider that the 1% of $W+$ 1 jet events which get promoted to $W+$ 2 jet events represent a 5% increase on the number of $W+$ 2 jet sample because the 2 jet sample is roughly 5 times smaller. The $W+$ 2 jet sample is also increased by promtions from the $W+$ 0 jet sample. The probabilty of a 2-jet promotion is 6 times smaller but the $W+$ 0 jet sample is 5 times larger than the $W+$ 1 jet sample. This means that the correction to the $W+$ 2 jet sample for $W+$ 0 jet promotions is roughly the same as that for $W+$ 1 jet promotions. The effect of the promotions therefore represents our second largest background correction to the $W+$ jet samples [4].

The actual correction for promotions is complicated by the fact that we must simultaneously correct for the jets being promoted to and from a particular jet multiplicity. In the promotion calculation we use a matrix of probabilities which maps the n jet sample to the $n+m$ jet sample via the promotion probability for m jets from extra interactions. The corrections to the $W+ \geq n$ jet samples are shown in table 4.9 and are calculated for m as high as 4.

Table 4.8: The table shows the probabilities for obtaining a single jet, 2 jets, 3 jets and 4 jets from an extra interaction. The first column shows the number of events found with m jets in the minimum bias sample. We use the number of vertices (40117) found in the minimum-bias sample and the number of extra vertices (41188) found in the W sample to calculate the probabilities in the second column (equation 4.7).

m jets	P_m	
1 jet	494	9.910^{-3}
2 jets	67	1.310^{-3}
3 jets	11	2.210^{-4}
4 jets	2	4.010^{-5}

A second source of promotion arises from $W\gamma$ events. The photon in these events

[4]except where top events become significant

will be counted as a jet if its transverse energy is above 15 GeV and $|\eta|$ is less than 2.4.

The probability (P_γ) that a photon will contribute a jet to an event in our W sample is 0.004 ± 0.0006. This value was determined from $W\gamma$ Monte Carlo events [28]. We corrected the photon energy using the standard jet corrections. The jet corrections raise the energy for the hadronic response of the detector and for the radiation that falls out of the 0.4 clustering cone. These corrections are necessary since we do not distinguish photons and jets in the data. After obtaining the number of photons which pass the jet selection cuts in the Monte Carlo, we scale the Monte Carlo luminosity to our data luminosity. We expect 207 ± 32 photons measured as jets in the W sample. This number of photon-jets yields the value of P_γ (207/51431).

To correct for photons faking jets we add P_γ for a photon faking a jet to the probability (P_1) of obtaining 1 jet from an extra interaction.

4.5.3 Errors on the Promotion Correction

Although the most reliable method for obtaining the promotion probabilities (P_m) is from the minimum-bias sample as described in the preceding section, we have estimated the number of jets from extra interactions in the W events from other methods to establish an error.

One study [29] looked at the $\Delta\phi_{ej}$ distribution between the electron and jet in $W+$ jet events. The electron from W decay is uncorrelated with jets from an independent interaction therefore this distribution is flat. The distribution for jets produced in association with W bosons will be peaked at π. The actual $W+$ jet data was fit with these distributions to extract the amount of each.

Another study divided the $W+$ jet sample into 4 subsamples dependent on the average instantaneous luminosity at which the events were collected. We would expect

that in high luminosity running the average number of extra interactions that occur would increase. This increase would result in a higher probability for jets from extra interactions.

The two studies gave results which bracketed our estimate from the minimum-bias sample and from these we quote an error on the promotion probabilities of +100% and -50%.

4.6 Chapter Summary

The significant backgrounds to the single $W+$ jet production have been estimated in this chapter. We found that the top contribution and multijet contamination are significant and are strongly dependent on the number of jets. The contamination of our $W \to e\nu$ + jet samples from $W \to \tau\nu$ and $Z \to e^+e^-$is small and have a negligible effect on the relative cross sections when compared to the systematics from top and multijet background subtraction. Finally, we corrected our counting of jets in W events for jets from extra interactions and photons identified as jets. The summary of our background estimates are presented in table 4.9.

Table 4.9: Summary of backgrounds to single $W+ \geq$ jet samples.

Background	n jets ≥ 0	n jets ≥ 1	n jets ≥ 2	n jets≥ 3	n jets≥ 4
QCD	1509	1248	412	125	33.6
$W \to \tau\nu$	726	196	62.9	7.87	1.26
$Z \to e^+e^-$	752	157	26.3	5.73	.92
Top	36.87	36.85	36.18	30.86	21.03
Promotion	0	464	149	40.8	9.92

Chapter 5

The Efficiency for Finding $W \rightarrow e\nu$ Events

5.1 Introduction

We restrict electrons to be in the region of the detector where the most reliable electron measurements are made. This requirement necessarily involves the loss of a large fraction of the W's produced at CDF. In this chapter we determine our losses from this requirement and all other requirements made in our W data selection. Since some W selection cuts are biased against events with jets, we measure the efficiency for each $W+$ n jet sample independently. The total efficiency for each W sample is the product of all individual efficiencies as shown in equation 5.1. The descriptions of these efficiencies are in table 5.1.

$$\epsilon_{tot} = \epsilon_{geo} \cdot \epsilon_{kin} \cdot \epsilon_{ID} \cdot \epsilon_{trig} \cdot \epsilon_{obl} \cdot \epsilon_{Zrem} \tag{5.1}$$

Table 5.1: The name and description of losses to the $W \rightarrow e\nu$ sample due to the selection criteria.

Name	description
Geometric(ϵ_{geo})	electron in central detector
	electron in well-instrumented region
Kinematic(ϵ_{kin})	electron $E_T \geq 20\ GeV$
	$\not{E}_t \geq 30\ GeV$
Identification(ϵ_{ID})	passes event and electron quality cuts
Trigger(ϵ_{trig})	passes online trigger cuts
Obliteration(ϵ_{obl})	loss of events due to electron-jet overlap
Z removal(ϵ_{Zrem})	loss of $W+$ jet events due to Z removal

5.2 Acceptance Calculation for $W + \geq n$ Jets

The efficiency for geometric and kinematic restrictions on the leptons is referred to as the acceptance. The geometric and kinematic acceptances are calculated separately. The geometric acceptance is the fraction of electrons that deposit energy in a fiducial region of the central electromagnetic calorimeter. The kinematic acceptance is the fraction of electrons and neutrinos to pass the E_T and $\not\!\!E_t$ cuts respectively. The fractions are calculated with simulated $W \rightarrow e\nu$ events.

5.2.1 $W+$ Jet Monte Carlo Samples

We generate $W + n$ parton data samples using a leading order Monte Carlo event generator (VECBOS [30]). The renormalization (Q^2_{ren}) scale for the calculation is the average parton P_T squared ($< P_T >^2$). The parton P_T and η cuts in VECBOS are 8 GeV/c and 3.5 respectively. There are no generation cuts on the electron or neutrino variables. Initial and final state radiation and underlying event energy are added using HERWIG[31] ($Q^2_{frg} = M^2_W + P^2_{tW}$). Events are passed through the detector simulation (QFL) to obtain the detector response of electron energy, jet energy, and underlying event energy. From the fully simulated Monte Carlo sample we select W events using our W selection executable. We count the number of reconstructed jets according to our jet selection cuts. A jet is defined in our acceptance calculation as it is in our W data selection:

- 0.4 cone clustering
- out-of-cone and underlying event corrections applied
- $E_T \geq 15\ GeV$ (corrected)
- $|\eta_{det}| \leq 2.4$

The number of events generated for each $W + n$ jets data is shown in table 5.2.

Table 5.2: Number of events with n jets reconstructed from $W + n$ parton Monte Carlo

Sample	# with n jets reconstructed
$W + 0$ jets	42836
$W + 1$ jets	37282
$W + 2$ jets	10972
$W + 3$ jets	3848
$W + 4$ jets	1399

To maintain consistency in the modeling of our W events, the W plus 0 jets sample is generated with VECBOS using a parton P_T cut lowered to 1 GeV. The Monte Carlo P_T distribution is then tuned off the real W data. This technique is described in appendix C.

5.2.2 Geometric Acceptance

We require the electron to be in the central region of the detector ($\eta \leq 1.1$). The region of the electron is determined from the reconstructed electron rather than the four-vector from the matrix element calculation so that we include detector smearing. The second acceptance cut applied to the electron is the fiducial requirement. Good fiducial status requires the electron to be in a well-instrumented region of the calorimeter. Non-fiducial regions include phi cracks, the 90 degree crack, chimney towers, tower 9, and electrons near tower edge (3 cm). The number of events with a central fiducial electron as a function of the jet multiplicity is shown in table 5.3.

In a small percentage of events the electron is not reconstructed. We determine the cause of such losses by using the four-vector from the matrix element calculation and propagating the electron into the detector. These "lost" electrons fall more

or less into two classes: electrons which escape the detector and electrons which are obliterated. An obliterated electron is defined as an electron which overlaps with a jet to the extent that electron reconstruction fails. The rate of obliteration is measured separately (section 5.3) using data. After propagating the electron the acceptance status is properly categorized. Table 5.6 lists the geometric acceptance for our W + jets samples.

5.2.3 Kinematic Acceptance

We apply a 20 GeV transverse energy cut to electrons in events which pass the geometry cuts. The electron energy is corrected with the Monte Carlo electron correction code which is the equivalent of the corrections used on W data events. The number of events surviving the electron E_T cut are presented in table 5.3.

Events with an electron $E_T \geq 20$ were tested for a $\not{E}_t \geq 30\ GeV$. We calculate the imbalance of transverse energy from fully corrected detector energy and include the effects of extra interactions. The smearing of $\not{E}_t$ due to extra interactions is performed 30 times per event so that the number of events listed in table 5.3 passing the $\not{E}_t$ cut is not an integer. The reliability of our simulation of $\not{E}_t$ is discussed in appendix B.

Table 5.3: Number of events passing each acceptance cut for our 0 to 4 jets samples.

Sample	N	$N_{central}$	$N_{fiducial}$	N_{E_T}	$N_{\not{E}_t}$
$W + 0$ jets	42835.7	23699.3	17862.7	15237.9	10054.2
$W + 1$ jets	37282.0	21486.0	16290.0	14139.0	8954.7
$W + 2$ jets	10972.0	6543.0	4954.0	4305.0	2646.6
$W + 3$ jets	3848.0	2383.0	1819.0	1566.0	1053.3
$W + 4$ jets	1399.0	873.0	654.0	575.0	384.4

5.2.4 Z Removal

Our selection of W events includes a rejection of events which pass loose Z identification requirements (chapter 3). These cuts are applied to a second electron after the primary electron identification and $\not\!\!E_t$ cut. This procedure is repeated on the W Monte Carlo. Although the Monte Carlo sample is entirely W + jets events, some jets in these events look enough like a second electron so that the event passes Z identification. Therefore the fraction of W events that pass the Z identification is dependent on the number of jets. Table 5.4 shows the efficiency for Z removal as calculated from our W Monte Carlo.

Table 5.4: Z removal efficiency for W + jets

Sample	Z removal
$W + 0$ jets	1.0000 ± 0.0
$W + 1$ jets	0.9976 ± 0.0005
$W + 2$ jets	0.9953 ± 0.0014
$W + 3$ jets	0.9881 ± 0.0035
$W + 4$ jets	0.9846 ± 0.0062

5.2.5 Systematics

In this section we present the systematics which can change the ratio of the acceptance of $W + n$ jets to that of $W + 0$ jets. We recalculate the acceptance from QFL after shifting the jet energy scale by $+/- 5.0\%$. This scaling will not only affect jet counting but will change the measurement of the $\not\!\!E_t$ which depends on the measurement of jet energy. The absolute shifts of the acceptance for this procedure are shown in table 5.5. We also have a choice for the renormalization scale when generating $W + n$ jets Monte Carlo. We expect some dependence on this parameter since the acceptance does depend on P_T and a $Q^2 = M_W^2 + P_{tW}^2$ would yield a harder P_T spectrum than

our default choice of $Q^2 =< P_T >^2$ (parton P_T). The shifts due to a change in the renormalization scale are also presented in table 5.5.

Table 5.5: Acceptances for variations in renormalization scale and jet energy scale.

Sample	Default	$Q^2_{ren} = {P_T}^2 + M^2_W$	+5% Et Scale	-5% Et Scale
$W + 1$ jets	0.2402	0.2406	0.2420	0.2381
$W + 2$ jets	0.2412	0.2423	0.2434	0.2407
$W + 3$ jets	0.2737	0.2766	0.2729	0.2702
$W + 4$ jets	0.2747	0.2756	0.2847	0.2717

5.2.6 Results and Conclusions

Our measured W acceptances are shown in table 5.6. The results are given for exclusive jet multiplicities with n=0 to 4. The measurement used a LO matrix element calculation with partial higher order corrections via a HERWIG parton shower simulation. The QFL detector simulation was used to model the response to electrons and the recoil to the W.

Table 5.6: Geometric and kinematic acceptances for W + jets. The last column shows the total acceptance with the statistical error and the systematic error respectively.

Sample	Geometric	Kinematic	Total
$W + 0$ jets	0.4170	0.5629	0.2347 ± 0.0020
$W + 1$ jets	0.4369	0.5497	$0.2402 \pm 0.0022 \pm 0.0021$
$W + 2$ jets	0.4515	0.5342	$0.2412 \pm 0.0041 \pm 0.0025$
$W + 3$ jets	0.4727	0.5791	$0.2737 \pm 0.0072 \pm 0.0045$
$W + 4$ jets	0.4675	0.5877	$0.2747 \pm 0.0119 \pm 0.0100$

5.3 Electron-Jet Overlap Losses

Subsequent to the kinematic and geometric cuts described, we apply a series of quality cuts to the electrons. The loss of true electrons due to these cuts will be determined in this section and the next. In this section we factor out the losses that depend on the jet activity in the event. As part of the W selection we require that the electron and any high E_T jets be separated by a radius of no less than 0.52. We can only apply this cut when we can physically distinguish an electron from a jet. If a jet and an electron occupy the same area of the detector we might lose the electron altogether. These events by their nature will not appear in the electron data samples therefore we need to simulate the effect from existing data.

5.3.1 Electron-Jet Overlap Data Samples and Calculation

The method we use to determine the rate at which jets and electrons overlap uses a Monte Carlo to decay W and Z bosons. We decay a boson many times and observe the rate that the electron from the decay falls on top of a jet in the event. In order to decay a boson we require its momentum. Unfortunately, this information does not exist for W bosons in the data because the longitudinal component of the neutrino is not known. The momentum is known for Z bosons in the data and for W's in Monte Carlo. The Z data can be used because we can remove the electron and positron from the event and substitute a $W \rightarrow e\nu$ decay. The advantage of the Z data is that it contains all sources of low-energy hadronic contamination of the electron. The disadvantage of the Z data is the limited statistics for events with high jet multiplicity. There are only 7 events in the $Z+$ 4 jet data. Although we decay the Z events several thousand times systematic effects can enter the calculation when using only a few events.

The Z data and W Monte Carlos events are passed through a special Monte Carlo

[32] that redecays the boson many times. We check to see if the electron from boson decay lands near any jets in the event. The criteria for the electron to be obliterated by jet activity is

- a jet cluster with an $E_T(\text{jet}) \geq 0.1 \cdot E_T(ele)$ within a cone of 0.4 of the electron cluster.
- a jet satisfying our jet selection criteria ($E_T \geq 15\ GeV$ and $|\eta| \leq 2.4$) within a cone of 0.52 of the electron

Our final results of decaying the W and Z bosons are shown in figure 5.1. These plots show the fraction of events which pass our electron-jet separation criteria. The errors are obtained by varying the polarization of the boson. The quantity that actually enters the W cross section calculations is the ratio of the efficiencies and not the absolute magnitude.

Where the Z statistics allow comparison the ratio showed agreement for the Z and W samples. In the magnitude the W Monte Carlo was a little more efficient than the Z data (figure 5.1. This is not surprising since low-energy contamination is not modelled well by the Monte Carlo(see appendix B).

Table 5.7: Electron-Jet Separation Efficiency for W + jets

Sample	obl
= 0 jets	0.9558 ± 0.0101
= 1 jets	0.9249 ± 0.0087
= 2 jets	0.8942 ± 0.0113
= 3 jets	0.8633 ± 0.0095
≥ 4 jets	0.8261 ± 0.0117

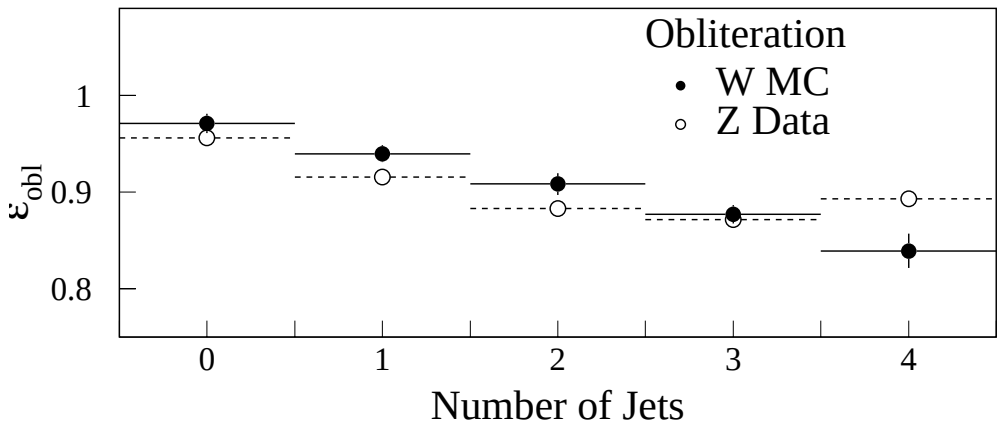

Figure 5.1: Obliteration efficiency as calculated from W Monte Carlo (filled circles) and Z data (open circles). Statistical errors only.

5.4 ID Efficiency

5.4.1 Introduction

We showed in chapter 3 that an effective means of selection electrons while reducing backgrounds was to impose electron quality criteria on the electromagnetic cluster in the central calorimeter. This procedure necessarily involves the loss of true electrons that happen to fail these cuts. Simulations of electron response are difficult because some of these cuts are sensitive to the running conditions such as the luminosity while others could show time dependent behavior due to the slow degradation of detectors such as the calorimeter. An example of the former is the isolation variable. The isolation is the fraction of non-electromagnetic energy in the vicinity of the electron. As the luminosity increases the average number of interactions increases. The contamination of the electron energy by extra interactions increases with the number of interactions and therefore with the luminosity. To obtain reliable efficiency numbers we measure the efficiency using data rather than simulations. The Z data

is a very suitable sample for several reasons. The Z data were collected over the same time period as our $W+$ jet data. The kinematics of Z and W boson decay are similar. Z bosons are easily found and contain very small backgrounds.

5.4.2 The ID Efficiency Sample and Calculation

We begin by selecting events from the inclusive electron sample. The events must have at least one lepton which passes our tight electron selection cuts. From this sample we apply the following cuts to a second electron.

- central
- $E_T \geq 20\ GeV$
- fiducial

The final result is a sample where both leptons are central and fiducial and both have a $E_T \geq 20\ GeV$. Additional event cuts are made to insure that we have clean Z bosons:

- $Q_{e^+} + Q_{e^-} = 0$
- $81 \leq M_{e^+e^-} \leq 101$
- $|Z_{vtx}| \leq 60.0$ cm

There are 2696 events which satisfy these cuts. In 2138 of these events both the electron and positron pass the electron quality cuts. Given that P represents the probability that a lepton will pass the quality cuts we can write the number of events which have both leptons passing as

$$N_{PP} = P^2 \cdot N_{tot} \tag{5.2}$$

and the number of events for one lepton passing as

$$N_{PF} = 2 \cdot P \cdot (1 - P) \cdot N_{tot} \tag{5.3}$$

N_{tot} represents all electron-positron pairs which satisfy the kinematic and event cuts listed above. This number is an unknown since we do not have the events for which both leptons fail the cuts. However we can eliminate N_{tot} from equations 5.2 and 5.3 and solve for the probability P in terms of N_{PP} and N_{PF}.

$$P = \frac{2 \cdot N_{PP}}{N_{PF} + 2 \cdot N_{PP}} \tag{5.4}$$

Substituting 2696-2138=558 for N_{PF} and 2138 for N_{PP} yields $P = 0.8846 \pm 0.0049$ as our ID efficiency.

We have assumed that our ID efficiency calculation is independent of the number of jets in the event. We did this because we calculated the efficiency with obvious jet dependence separately. To check that this was a reasonable course of action we recalculate the ID efficiency for each $Z+$ jet sample. The results are shown in table 5.8. We do not observe a significant trend for the efficiency as a function of jet multiplicity.

Table 5.8: ID efficiency for electrons as a function of the number of jets.

Sample	$N_{pf} + N_{pp}$	N_{pp}	ϵ_{ID}
= 0 jets	2128	1690	0.8853 ± 0.0054
= 1 jets	439	348	0.8844 ± 0.0120
= 2 jets	107	83	0.8737 ± 0.0256
= 3 jets	18	14	0.8750 ± 0.0620
$\geq$ 4 jets	4	3	0.8571 ± 0.1414

5.5 Trigger Efficiency

The selection of a our electron dataset must begin online with a hardware trigger that is designed to signal the presence of a high E_T central electron candidate. All events in our data sample must pass the level-two and level-three inclusive central electron triggers. To determine the fraction of electrons which fail these triggers we select a new W boson sample from the $\not\!\!E_t$ triggers at level-two and level-three which are based on identifying neutrino candidates instead of electron candidates. This trigger provides a dataset from which to select W bosons without the requirement of an electron trigger. From these events we select W events by applying our geometric, kinematic and extra tight[1] electron selection. The $\not\!\!E_t$ is required to be at least 25 GeV. We find 36999 events passing these cuts. From these events we check that the electron passes the level-two and level-three central electron triggers. The efficiency is then

$$\epsilon_{trig} = \frac{N_p}{N} \tag{5.5}$$

The number of events which pass (N_p) is 36781 so that our trigger efficiency is 0.9941 $\pm$ 0.0004. The results are presented as a function of the number of jets in table 5.9 and show no dependence with jet multiplicity.

5.6 Chapter Summary

We have measured the efficiencies for identifying $W \rightarrow e\nu$ decays as a function of the number of jets. The individual and total efficiencies are collected in table 5.10. One source of W boson loss has not been determined in these estimates. The loss of a $W \rightarrow e\nu$ events due to our requirement that the event vertex is within 60 cm of

[1] "extra tight" refers to limiting the isolation to less than 0.05 to eliminate multijet background

Table 5.9: Trigger efficiency for electrons as a function of the number of jets.

Sample	ϵ_{trig}
= 0 jets	0.9936 ± 0.0005
= 1 jets	0.9969 ± 0.0007
= 2 jets	0.9947 ± 0.0022
= 3 jets	0.9959 ± 0.0041
≥4 jets	0.9667 ± 0.0232

the center of the detector is not dependent on the number of jets and therefore will cancel in our final cross section measurements since we scale our cross section to a previous CDF inclusive W measurement. The value has been determined for the run 1a data ($\approx$ .95[34]).

Table 5.10: Summary of $W+$ jet efficiencies.

Eff	= 0 jets	= 1 jets	= 2 jets	= 3 jets	≥4 jets
ϵ_{geo}	0.4170	0.4369	0.4515	0.4727	0.4675
ϵ_{kin}	0.5629	0.5497	0.5342	0.5791	0.5877
ϵ_{ID}	0.8846	0.8846	0.8846	0.8846	0.8846
ϵ_{Trig}	0.9941	0.9941	0.9941	0.9941	0.9941
ϵ_{obl}	0.9478	0.9172	0.8867	0.8561	0.8192
ϵ_{Zrem}	1.0000	0.9976	0.9953	0.9881	0.9846
ϵ_{tot}	0.1956	0.1933	0.1872	0.2036	0.1948

Chapter 6

Data Results

6.1 Introduction

We have measured the quantities required for a calculation of the direct single $W \to e\nu + \geq n$ jet cross sections. First, we calculate the number of $W \to e\nu + \geq n$ jet events produced at CDF during the period of data collection. This number is derived by correcting the number of $W \to e\nu + \geq n$ jet candidates for the contamination from backgrounds and for the loss of direct single $W \to e\nu + \geq n$ jet events (efficiency). The relative production is defined as the number of $W \to e\nu + \geq n$ jet events divided by the total number of $W \to e\nu$ events. The absolute cross sections will be obtained from the relative production rates by scaling to the inclusive $W \to e\nu$ cross section as measured from a previous CDF analysis [35].

The $W+$ jet cross section measurements are derived from a sample of events which were selected with analysis cuts designed to parallel a previous $Z+$ jet [33] analysis. A comparison of the W and Z measurements has the advantage that the largest systematic in the data ,the jet counting uncertainty, will cancel to a large degree. Preliminary results for the W and Z ratio as function of jet multiplicity is in agreement with theory.

6.2 $W \to e\nu + \geq n$ Jet Cross Section Results

To calculate the number of $W \to e\nu$ events produced with at least n jets, we use the number of $W \to e\nu + \geq n$ jet candidates (N_n), the estimated background contamination (B_n), and the efficiency of identifying a $W \to e\nu$ decay (ϵ_n). The subscript

indicates that these quantities are measured for each $W+\geq n$ jet sample. B_n is subtracted to remove undesired contributions from our sample. The result of subtracting the background yields the number of $W \rightarrow e\nu$ events in our candidate sample that were contributed from direct single W production. The estimates in chapter 5 yielded the efficiency (ϵ_n) of identifying a $W \rightarrow e\nu$ decay when the W is produced with n jets. Therefore we divide by this efficiency to obtain the number of $W \rightarrow e\nu$ events that were produced. The calculation is presented explicitly in equation 6.1. Substituting $n = 0$ into this equation yields the total (inclusive) number of direct single $W \rightarrow e\nu$ events. The fraction F_n is defined as the rate of $W \rightarrow e\nu + \geq n$ jet events relative to the total production rate and is given by equation 6.3. These fractions (F_n) are the relative production rates and they are presented in table 6.1. The inputs that were used in the determination of the relative production rates are also shown in the table.

$$N'_n = \frac{N_n - B_n}{\epsilon_n} \tag{6.1}$$

$$N'_0 = \frac{N_0 - B_0}{\epsilon_0} \tag{6.2}$$

$$F_n = \frac{N'_n}{N'_0} \tag{6.3}$$

The last step for obtaining cross sections is to scale the relative rates to the inclusive cross section times the branching ratio ($\sigma_0(W) \cdot BR(W \rightarrow e\nu\ ) = 2490 \pm 120\ pb$ [35]). The inclusive cross section times branching ratio is from a previous CDF analysis that used the first 19.6 pb^{-1} of luminosity. The luminosity and vertex cut efficiency were well measured for these data. The errors in this measurement are retained in our absolute cross section measurements and represent a 4.8% error for each $W+\geq n$

Table 6.1: Candidates, total background, total W efficiency (exclusive), and the relative cross sections for the $W+$ jet samples.

	≥ 0	≥ 1	≥ 2	≥ 3	≥ 4	≥ 5
N_n	51431	11144	2596	580	126	21
B_n	3024	2102	686	210	66.7	16.2
ϵ_n	0.1956	0.1933	0.1872	0.2036	0.1948	0.1948
F_n	1.0000	0.1868	0.3945×10^{-1}	0.7638×10^{-2}	0.1224×10^{-2}	0.9823×10^{-4}

jet cross section. We refer to this contribution to the error as the common error. The absolute cross sections for $W \to e\nu + \geq n$ jets are presented in table 6.2 and plotted in figure 6.1. The curve in figure 6.1 is an exponential fit to the data. The errors in table 6.2 are divided according to type. The first error listed in the table 6.2 is the statistical error. The second error is the common error due to the uncertainty on the inclusive W cross section measurement (4.8%). The third error is the systematic error.

The systematic error dominates the errors in the $W+$ jet measurements. An estimate of the systematic error must avoid double counting the uncertainties that are already accounted for in the common error. This is achieved by defining the systematic error to represent only the uncertainty on the ratio of $W+\geq n$ jet events to $W+\geq 0$ jet events. We discuss the quantities that can change the ratio in section 6.3. Here, we only note that the dominant contribution is due to the uncertainty on the the jet energy.

Also shown in table 6.2 is the ratio

$$R_{n/(n-1)} = \frac{\sigma_n}{\sigma_{n-1}}$$

$R_{n/(n-1)}$ shows explicitly that the cross section drops about a factor of 5 with each additional jet. This ratio gives the probability of measuring one additional jet in a W event and is therefore closely related to the coupling strength of the strong

interaction α_s. In chapter 7, we use $R_{n/(n-1)}$ to make more demanding tests of QCD since the error on this ratio is smaller than the error on the absolute cross section. The cancellation of the systematic error is predominately due to the correlation in the jet counting errors in the numerator and denominator of $R_{n/(n-1)}$. For example, the increase in the number of jets from a shift in the jet energy increases both σ_n and σ_{n-1}. The increase in cross section is greater for higher jet multiplicities so that the cancellation is not complete but the final error is relatively smaller when compared to the absolute cross sections. This argument is not true in the ratio $\frac{\sigma_1}{\sigma_0}$ because σ_0 is insensitive to the jet counting errors. We will present the systematic errors more completely in section 6.3.

Table 6.2: $W+\ \geq n$ jet Cross Sections. The first error listed is the combined statistical error which includes the statistical error on the number of events and the statistical error on the efficiency and background calculations. The second error is a common systematic error of 4.8% from the input inclusive W cross section. The third error is the systematic which is dominated by jet counting systematics (see next section). For this table we list the maximum of the plus and minus systematic. The last error is the total error.

n	Cross Sections Results					
Jets	$BR \cdot \sigma$ (pb) Stat	Common	Syst.	Total	$\frac{\sigma_n}{\sigma_{n-1}}$	
≥ 1	471.2 ± 6.3	± 23.1	± 51.8	± 57.1	0.189	± 0.021
≥ 2	100.9 ± 3.2	± 4.9	± 18.1	± 19.0	0.214	$\pm .015$
≥ 3	18.4 ± 1.4	± 0.9	± 5.1	± 5.3	0.182	± 0.020
≥ 4	3.1 ± 0.7	± 0.1	± 1.2	± 1.4	0.166	± 0.042
≥ 5	0.24 ± 0.24	± 0.01	± 0.28	± 0.36	0.080	± 0.109

6.2.1 The $W+\ \geq$5 Jet Cross Section

We have included the $W+\ \geq$5 jet cross section measurement in table 6.2 and figure 6.1. The $W+\ \geq 5$ jet sample contains a sufficient number of events (26) for a measurement; however, some of the other quantities necessary for a cross section must be determined from calculations at lower jet multiplicities. Specifically, we must

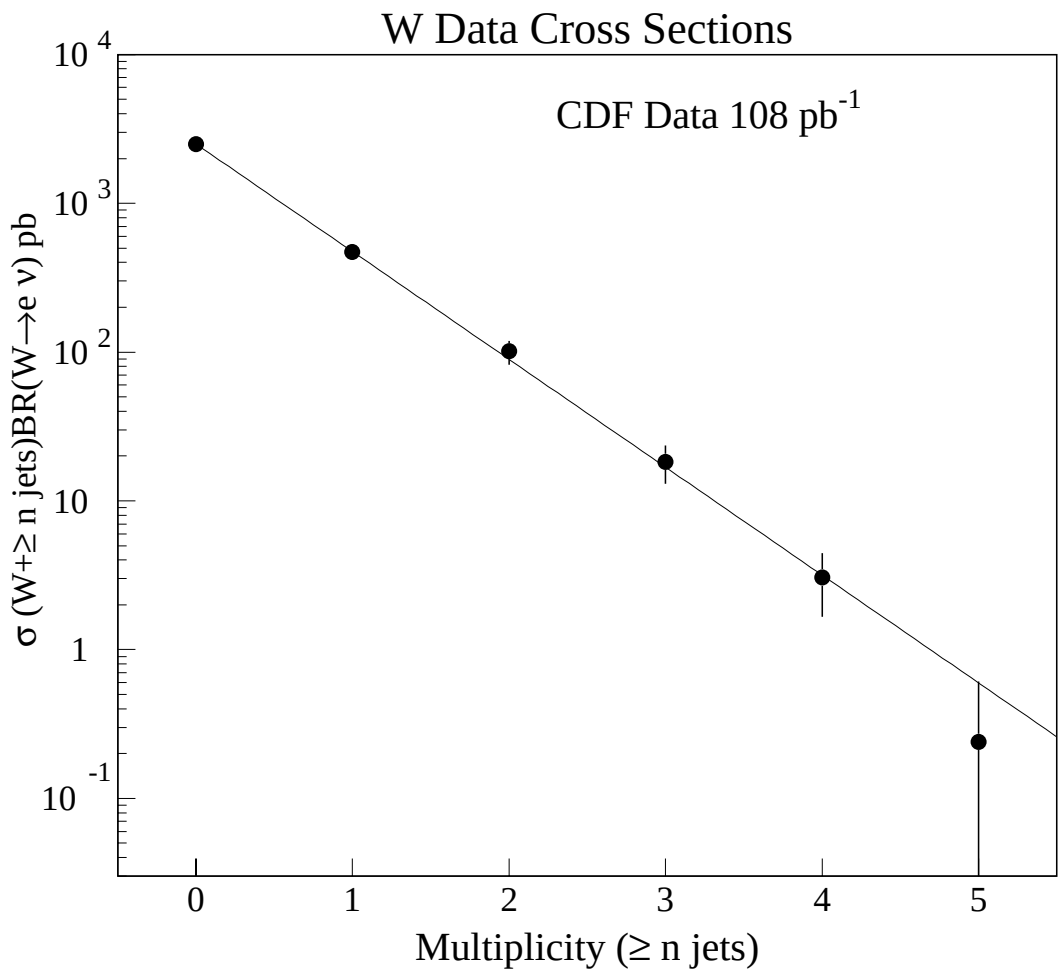

Figure 6.1: $W + \geq n$ jets cross sections. The inclusive ($W+ \geq$0 jet) cross section is from a previous CDF measurement.

use the efficiency (ϵ_4) for the 5 jet efficiency. Although some individual efficiencies showed a dependence on the number of jets (chapter 5), the total efficiency is fairly flat so that the uncertainty on our 5 jet efficiency is relatively small when compared to the jet counting systematics and even the statistical error.

We were able to calculate the QCD and top backgrounds for the 5 jet data but the smaller backgrounds ($W \rightarrow \tau\nu$ and $Z \rightarrow e^+e^-$) are taken from the 4 jet calculation (chapter 4). Again, the smaller backgrounds do not show a substantial trend with

the number of jets in the event so that the $W+\geq 5$ jet cross section measurement does not contain a significant error from these approximations.

6.3 Determination of the Systematic and Statistical Errors

6.3.1 Sytematic Errors

In this section we give descriptions of the systematic errors in the $W+$ jets analysis. The determination of a particular systematic is produced by varying a quantity by its uncertainty and recalculating the cross section. The difference of the new cross section and default cross section yields the systematic error on the cross section. The systematic variations we examine are those that change the ratio of the number of events with $\geq n$ jets to the total number of events. The following quantities are varied systematically:

- Jet Counting Variations
    1. Jet E_T
    2. Jet Detector η
    3. Jet Underlying Event Energy Scale
    4. Promotion Correction
- Background
    1. QCD background Normalization
    2. TOP background Normalization
- Efficiencies
    1. Obliteration

2. Acceptance

The uncertainty on each of these quantities is explained more fully in the associated chapters but we have collected brief descriptions of each variation in appendix D for easy reference. Table 6.3 and figure 6.2 show the change in the cross sections as a result of the variations that are listed above. Figure 6.2 clearly shows that systematic error due to the uncertainty on jet counting dominates in all $\geq n$ jet samples. The counting error is in turn dominated by the uncertainty of the jet E_T. However, the contribution of systematic error due to extra interactions is also significant. The effect of extra interactions is seen in two uncertainties. First, the uncertainty on the correction of jet energy due to contamination of 0.4 clustering cone (UE) from extra interaction energy. Second, the uncertainty on the promotion correction which corrects for jets from extra interactions. As the instantaneous luminosity at CDF increases both the extra interaction correction and the promotion correction contribute a larger fraction of the total error. This point needs to be considered in future analyses which will collect data at even higher instantaneous luminosities.

Table 6.3: List of systematic errors for $W+$ jets analysis.

	$W+ \geq 1$ Jet		$W+ \geq 2$ Jets		$W+ \geq 3$ Jets		$W+ \geq 4$ Jets	
Syst (pb)	$-\sigma$	$+\sigma$	$-\sigma$	$+\sigma$	$-\sigma$	$+\sigma$	$-\sigma$	$+\sigma$
E_T scale	−31.46	31.79	−10.11	11.52	−2.35	3.08	−0.53	0.70
η_{det}	−10.73	9.08	−4.10	3.71	−0.99	0.89	−0.41	0.17
UE	−22.96	27.29	−8.57	9.87	−1.91	3.01	−0.48	0.65
Promotion	−12.13	24.69	−3.75	7.24	−0.97	1.81	−0.24	0.44
QCD	−15.18	14.90	−5.58	5.48	−1.71	1.68	−0.49	0.49
Top	−0.24	0.24	−0.28	0.28	−0.24	0.24	−0.17	0.17
Acceptance	−3.58	3.64	−1.02	1.05	−0.32	0.34	−0.10	0.11
Oblit	−0.97	0.97	−0.30	0.30	−0.11	0.11	−0.04	0.04

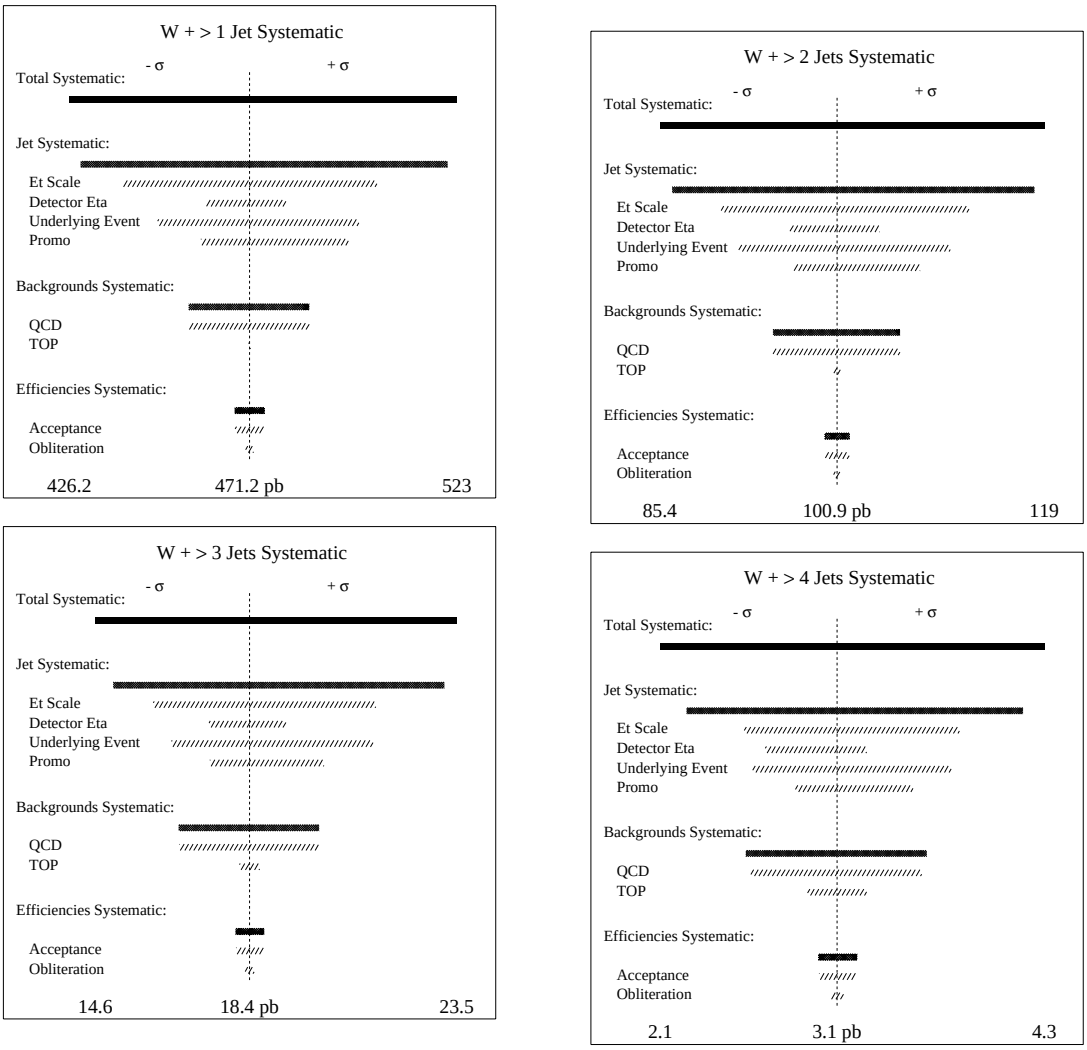

Figure 6.2: Cross section Systematics.

6.3.2 Statistical Errors

The statistical errors on the cross sections are shown in figure 6.3 for the $W+\geq n$ jet ($n = 1, 2, 3, 4$) samples. The statistical error is the counting error as determined from the raw number of events(N_n). Shown separately is the error on the cross sections due to the statistics of the independent samples used to determine the background expectations and the individual efficiencies. All statistical errors are fully propagated through the cross section calculation.

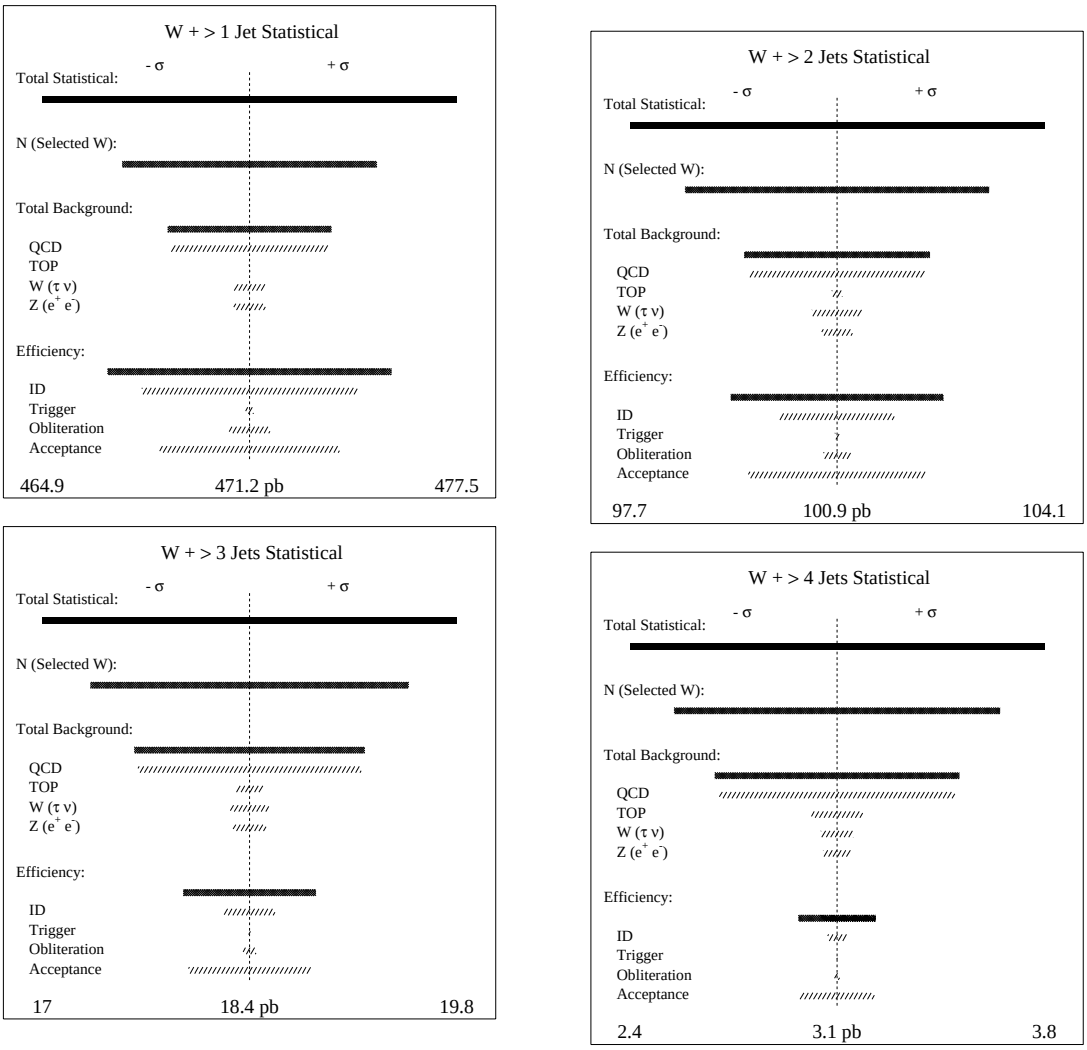

Figure 6.3: Statistical Errors.

6.3.3 Comments on the $W+$ Jet Cross Section Errors

Figure 6.4 shows the ratio of the statistical error to the systematic error for all jet multiplicities. We are clearly systematics limited with the systematic error dominated by the jet counting systematics. Given the current jet systematics we cannot expect a significant reduction in the total error with the addition of more data. This is true even at the 4 jet level. The bottom of figure 6.4 shows the total error for an equivalent run 2 analysis with the assumption of 20 times the statistics. For this plot all systematic errors defined above were held constant and all statistical errors above were reduced by $\sqrt{20}$.

6.4 Comparison of W and Z Cross Sections

The data selection for $W+$ jet samples began with the inclusive electron sample. This sample was also the source for a previous $Z+$ jet analysis [33] which utilized identical tight central electron identification cuts and identical jet definitions. Both measurements have been fully corrected for boson efficiencies. The $W+$ jet cross sections are calculated for direct single $W+$ jet production by removing other significant sources of real W's (top quark). Isolating single direct W production allows a fair comparison to the Z measurements.

In figure 6.5 we plot the W and Z cross sections as function of the jet multiplicity. Within the statistical error of leading order QCD calculations for direct single $W/Z+$ $\geq n$ jet cross sections [1], we expect no dependence of the ratio of W to Z cross sections on the jet multiplicity. The inset plot in figure 6.5 shows this ratio with statistical errors only for n=1 to 4. The ratio of the inclusive W and Z measurements [36] which are used to scale the W and $Z+$ jet measurements is also shown. We see no anomalous deviations from the expected flat behavior.

[1] 4 jet numbers are unavailable for the $Z+$ jet predictions

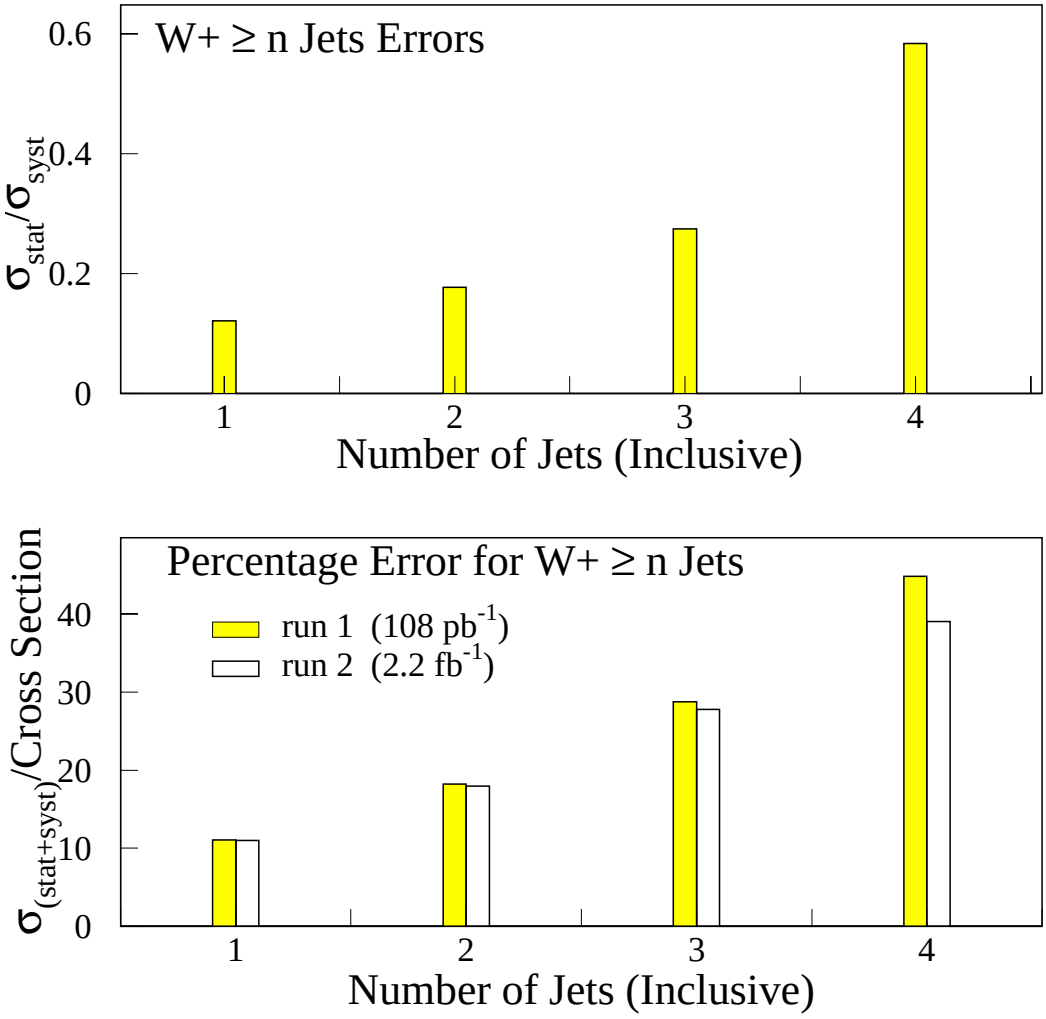

Figure 6.4: The upper plot is the ratio of the statistical error to systematic error for our $W+$ jet cross sections. The $x-$axis is is the number of jets. The lower figure gives the percentage error for $W+$ jet cross sections. The shaded histogram represents the current analysis and the unshaded represents the same analysis with 20 times the events. The systematic uncertainties were held constant.

6.5 Chapter Summary

We have measured the cross sections for W production times the branching ratio to $e\nu$ as function of inclusive jet multiplicity. The measurements were made for $n=$ 1, 2, 3, 4, and 5. We presented the errors on the cross section which included all

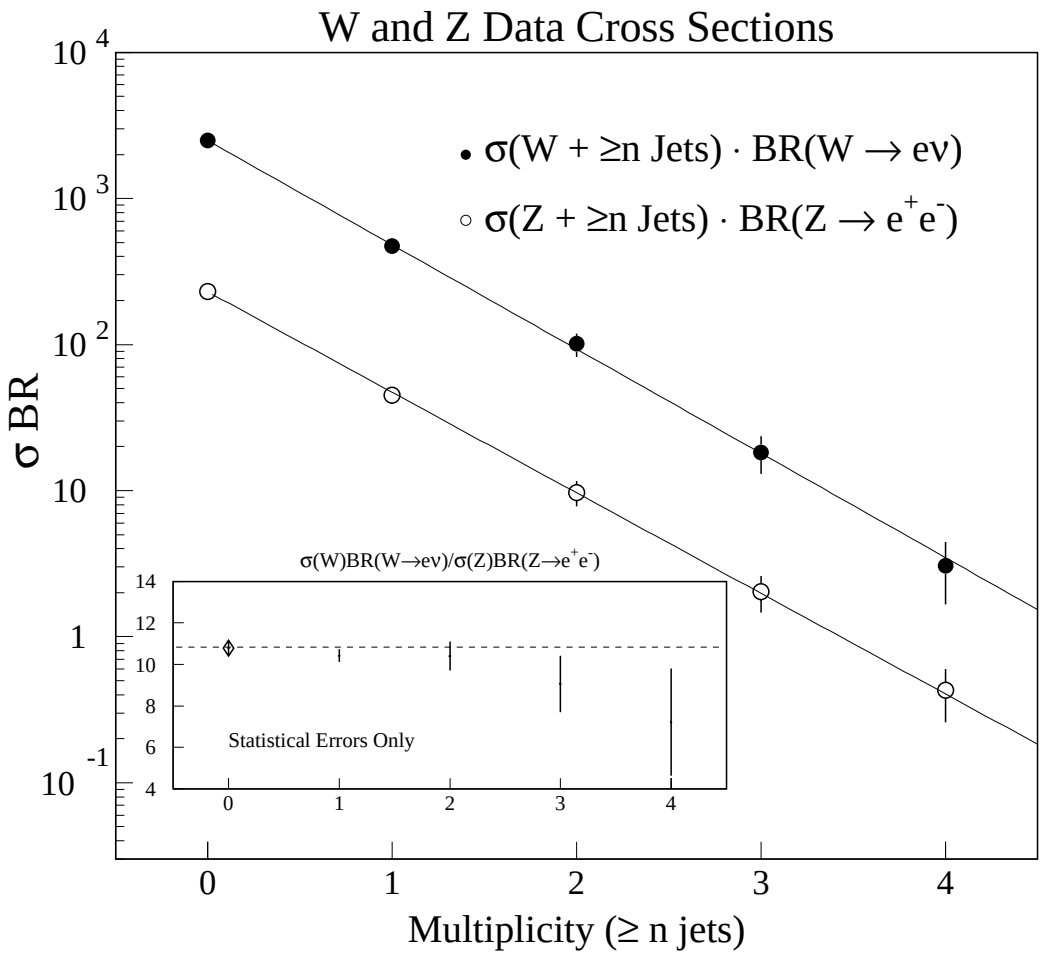

Figure 6.5: Comparison of $W \to e\nu$ and $Z \to e^+e^-$cross section vs jet multiplicity. The inset shows the ratio of the $W \to e\nu$ cross section to the $Z \to e^+e^-$cross section. The error bars represent statistical uncertainties only.

known statistical and systematic errors. The systematic error is dominated by the uncertainty in counting jets in W events. The ratio of $\frac{\sigma_n}{\sigma_{n-1}}$ $(R_{n/(n-1)})$ was calculated and showed that the drop in the cross section with the addition of 1 jet is about a factor 5. We compared the W and Z cross sections as function of the number of jets. A full systematic evaluation of the W to Z ratio is not complete but the dominant systematic, jet counting, will almost completely cancel. The ratio of W to Z cross sections as a function of the number of jets showed the expected flat behavior within

the statistical errors of the measurements.

Chapter 7

Comparison to Theory and Conclusions

7.1 Introduction

As described in chapter 1, generating perturbative QCD predictions requires several inputs which must be chosen with reasonable attention to both theoretical and experimental considerations. The leading order $W+$ parton calculations are most sensitive to the renormalization scale used in the evaluation of the strong coupling of the theory. We assess the dependence on this scale and other inputs to the LO perturbative calculation.

Perturbative QCD yields definite predictions for the $W+$ parton cross sections. In order to compare theory to data at the level of jets, we use the HERWIG parton shower simulation which fragments the parton and hadronizes the final state quarks. Additionally, this procedures provides gluon radiation off the initial state partons. The degree to which HERWIG adds radiation is determined by the fragmentation scale. As expected, the cross section predictions are fairly insensitive to this scale but the kinematic predictions show some dependence which we discuss in this chapter.

7.2 Theory Implementation

We use the program VECBOS[30], a leading order $W(Z)+$ parton Monte Carlo event generator, to produce the $W \rightarrow e\nu + n$ parton event samples. For n= 1,2,3 and 4, we generate samples of 50000 events using the following generation cuts

- parton $P_T \geq 8.0\ GeV/c$

- parton $|\eta| \leq 3.5$, where $\eta = -\log(\tan(\theta/2))$ and θ is measured from the proton direction.

- $\Delta R_{pp} \geq 0.4$ where $\Delta R = (\Delta\eta^2 + \Delta\phi^2)^{1/2}$ is the angular separation of the partons in $\eta - \phi$ space

The leading order Matrix element calculation uses a two-loop (NLO) evolution of α_s chosen for consistency with the NLO order parton distribution function (CTEQ3M). We evaluate α_s at two renormalization scales that bracket the W boson mass. These scales are defined by equations 7.1 and 7.2 below. The value of α_s as a function of the renormalization scale is shown in figure 7.1.

The low renormalization scale is defined by the average value of the parton P_T. Explicitly, the lower renormalization scale is the scalar sum of the parton P_T's divided by the number of partons (n). The value of the lower renormalization scale is on average approximately $\frac{M_W}{4}$. The high renormalization scale is defined by the square root of the sum of the squares of the bosons mass [1] and P_T. The average value of this quantity is about 84 GeV. The lower scale has several features that distinguish it from the higher scale. First, it is on average less than 1/4 of the higher scale which means that the value of α_s is larger. The cross sections for the lower renormalization scale will be greater. Additionally, the decrease of the cross sections as a function of jet multiplicity will depend on the renormalization scale since the power of α_s is n. Finally, the lower renormalization scale varies with the parton P_T which can vary by an order of magnitude from event to event, while the higher scale is more or less a constant because the W boson invariant mass is large and fairly constant. This last distinction will primarily be reflected in the shapes of the kinematic variables that we examine. We will see that the differences in the higher and lower renomalization

[1] c is suppressed

scales do not have a large effect on these shapes so that the kinematic variables provide stringent tests of QCD predictions.

$$Q^2_{ren\ low} =< P_T >^2 = (\frac{\sum P_{Ti}}{n})^2 \tag{7.1}$$

$$Q^2_{ren\ high} = M_w^2 + P_{TW}^2 \tag{7.2}$$

The factorization scale is the scale used to evaluate the proton structure as defined by the parton distribution functions. This scale is always set equal to the renormalization scale for the $W+\ n$ parton predictions. The results of varying these scales independently for the $W+\ 1$ parton calculation are shown in figure 7.2. The horizontal axis of this figure is the renormalization scale. The vertical axis, λ, is the ratio of the factorization scale to the renormalization scale. For each renormalization choice we have varied the factorization scale between 60% and 130% of the renormalization scale. The lines are contours of equal cross section. Specifically, the lines are chosen to represent 6% deviations from a reference cross section ($Q^2_{ren} = Q^2_{fac} = M_W$). The figure indicates that the sensitivity to the factorization scale is much less than the sensitivity to the renormalization scale.

Although the VECBOS parton calculations are not compared directly to data it is interesting to explore the dependency of the kinematic predictions on the various inputs to the theory. This allows us to see the effects of the LO scales factorized from the enhancements which are described in the next section. Figure 7.3 compares the $W+\ 1$ parton predictions for the parton P_T distribution. The comparison is made for changes in the renormalization scale, the factorization scale and the parton distribution function. The renormalization scale has a noticeable effect on the parton P_T shape especially at low P_T. This is expected because the lower renormalization scale is in a region where α_s changes more rapidly (figure 7.1). For the 1 parton sample that is plotted in figure 7.3, there is an exact correlation between the parton

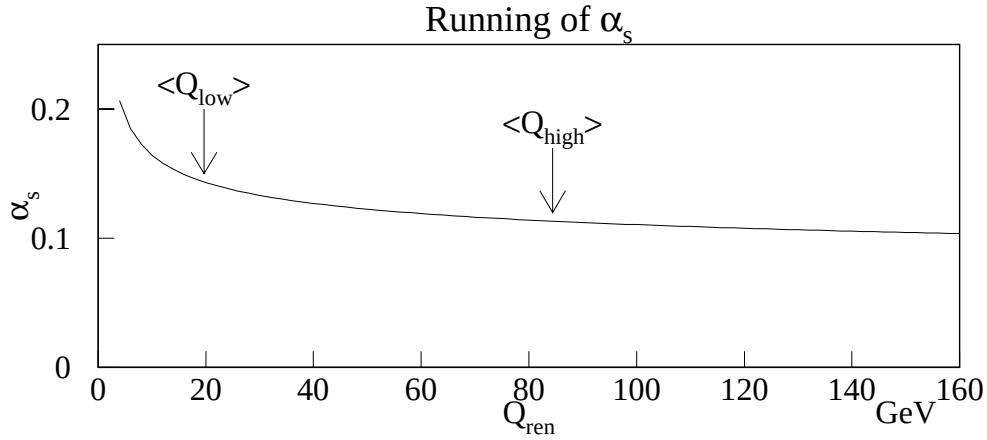

Figure 7.1: The variation of strong coupling (α_s,two-loop) with the renormalization scale. The value of α_s for the two renormalization scales that are used in the LO matrix element calculation are indicated by the arrows.

P_T and the renormalization scale.

Fragmentation and Hadronization

The jet energy corrections in the $W+$ jet data analysis are designed to correct jets back to the parent-parton energy. Ideally we would compare the data results to the VECBOS predictions; however, parton fragmentation effects and measurement resolution must be included before a comparison is warranted.

A HERWIG([31]) parton shower simulation is used to fragment the partons and add initial state gluon radiation. The fragmentation scale sets an upper energy limit on the added radiation from HERWIG. We use two scales for this fragmentation scale which are identical to the choices we use for the renormalization scale. The lower scale essentially limits the radiation from HERWIG to a level lower than that of the partons from the matrix element calculation. The higher (or hard) scale is more or less a flat scale which allows the addition of very high radiation. The radiation added by HERWIG can sometimes be hard enough to produce its own jet. In this way, the

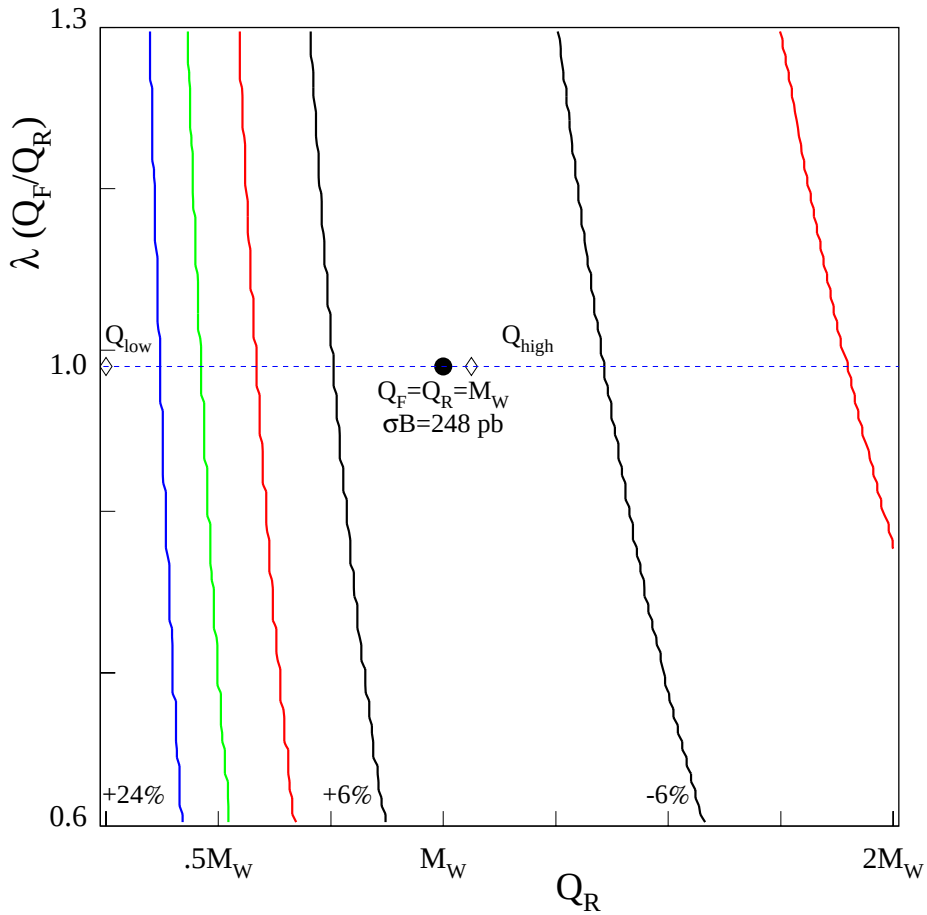

Figure 7.2: Contour plot of the deviation of the LO $W+$ 1 parton cross section as a function of the renormalization scale (horizontal axis) and the factorization scale(vertical axis). The vertical axis is the ratio of factorization to renormalization scale. The deviation is defined as the absolute value of the percentage difference from the cross section at $Q^2_{ren} = Q^2_{fac} = M_W$. The dotted line is cross section for $Q^2_{ren} = Q^2_{fac}$. The average value for our default choices for the renormalization scale are shown on this line.

$W+$ n parton calculations provided by VECBOS are enhanced to provide a $W+\geq n$ jet calculations. We refer to the VECBOS+HERWIG calculation as enhanced leading order.

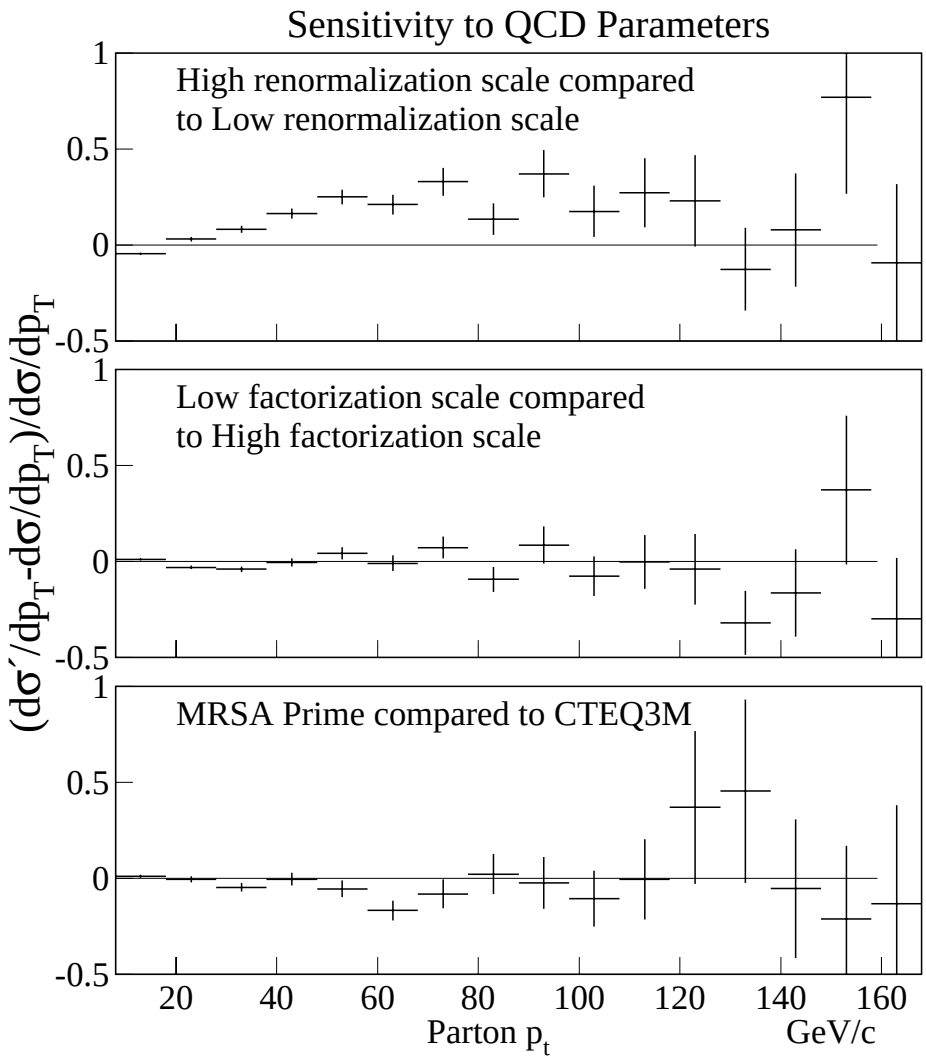

Figure 7.3: Comparison of the parton P_T distributions for various $W+$ 1 parton VECBOS Monte Carlo samples. The plots shows (theory′-theory)/theory as a function of parton P_T. The default calculation uses $Q^2_{ren} = Q^2_{fac} = < P_t >^2$. This sample is compared to a sample derived from the high renormalization scale $Q^2_{ren} = M^2_W + P^2_{tW}$ (top), the high factorization scale $Q^2_{ren} = M^2_W + P^2_{tW}$ (middle) and an alternate pdf MRSA′ (bottom).

Enhanced LO Predictions

The enhanced LO $W+ \geq n$ jet cross sections are presented in table 7.1 for both the hard and soft fragmentation scales. The $W+ \geq n$ jet cross sections were measured by

counting the number of events with at least n jets that have a E_T above 15 GeV and an $|\eta|$ less than 2.4. The jets from the HERWIG output were first processed with a detector simulation (QFL) to model the detector jet acceptance, jet energy response and jet energy resolution. The reconstruction of jet energy in the simulated Monte Carlo is identical to the algorithm used in the data.

Table 7.1: Enhanced LO $W+ \geq n$ jet cross section predictions. The results are presented for n=1 to 4 with statistical errors shown. The determination of the cross section counted jets with a $E_T \geq 15.0$ GeV and an $|\eta_{det}| \leq 2.4$ after a full detector simulation of the jets had been performed.

$Q^2_{ren} = Q^2_{fac}$	$< P_t >^2$	$< P_t >^2$	$M^2_W + P^2_{tW}$
Q^2_{frg}	$M^2_W + P^2_{tW}$	$< P_t >^2$	$M^2_W + P^2_{tW}$
$W+ \geq 1$ jet	367 $\pm$ 5.4	316 $\pm$ 4.6	285 $\pm$ 4.0
$W+ \geq 2$ jet	112 $\pm$ 4.6	80.8 $\pm$ 2.5	58.1 $\pm$ 1.0
$W+ \geq 3$ jet	27.2 $\pm$ 2.1	21.1 $\pm$ 1.3	12.3 $\pm$ .62
$W+ \geq 4$ jet	5.81 $\pm$ .77	–	2.29 $\pm$ .21

7.3 Comparisons to Data

7.3.1 Cross Section Comparisons

The $W \rightarrow e\nu$ + jet measured cross sections and the theory predictions for these cross sections are plotted in figure 7.4. The errors on the data points are the sum of the statistical and systematic errors. The sensitivity to the renormalization scale is indicated by the band between the two theory predictions. The lower renormalization scale ($< P_t >^2$) yields higher cross sections as is expected since α_s has a higher value at lower renormalization scale.

We have have also plotted the leading order theory prediction [37] for the inclusive W cross section ($W \rightarrow e\nu$ + $\geq$0 jets). There is no QCD theory in this point (α_s^0); therefore, there is no dependence on the renormalization scale. The uncertainty

on the inclusive prediction is derived from the sensitivity to the factorization scale. The variation of this scale was from $\frac{M_W}{2}$ to $2M_W$ while the default value is M_W. The variation is not noticeable in the plot. This choice of factorization scale is consistent with the higher factorization scale ($\sqrt{(M_W^2 + P_{tW}^2\ )}$) that we use in the $W+$ jet predictions because the boson P_T is 0 for the born level calculation.

In figure 7.5 we plot the ratio of data to theory cross sections versus the jet multiplicity. The upper plot shows the change in the theory predictions with the same renormalization scales from the previous cross section plot. This plot is to be compared with the lower plot in the same figure which shows the variation of the cross sections with the fragmentation scale. Clearly the fragmentation scale does not introduce large uncertainties into the cross section predictions when compared with the renormalization scale. The increase in cross section at a higher fragmentation scale is understood as the introduction of parton radiation from HERWIG that passes our jet selection criteria. These HERWIG jets can promote an event into the sample when the event contains a parton from the matrix element calculation that has failed the jet cuts.

We show the ratio $R_{n(n-1)}$=($\frac{\sigma_n}{\sigma_{n-1}}$) for the data and Monte Carlo at the top of figure 7.6. The data measurement of this ratio benefits because the errors are less than half the relative size of the cross section errors [2]. We also see that $R_{n(n-1)}$ is more robust to the renormalization scale.

The particular value of $R_{n(n-1)}$ will vary as function of the specific jet E_T cut that defines a jet. The jet definition we chose is jet E_T $\geq$15. To remove this dependence to some degree we plot in figure 7.6 (bottom) the ratio of data and theory for $R_{n(n-1)}$. With accurate theory predictions and accurate data measurements the value of this ratio is 1.0. The predictions and measurements are in fair agreement for this quantity.

[2]This is true except at one point R_{10} where the jet counting systematics will not cancel.

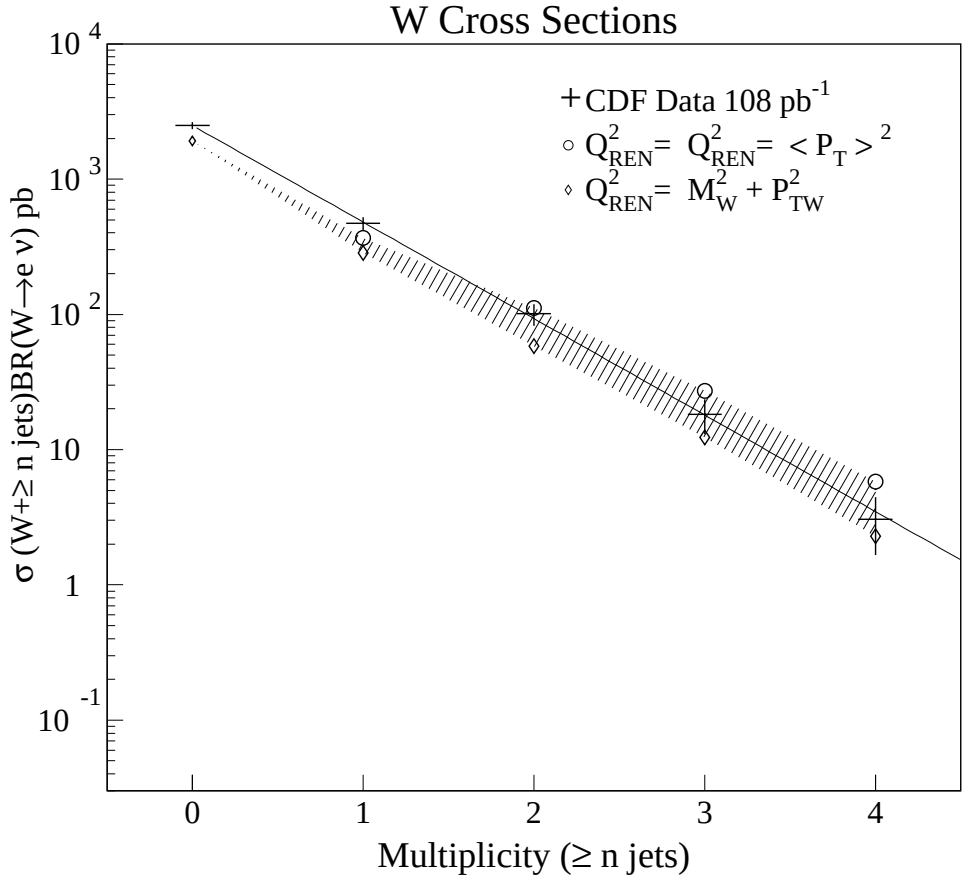

Figure 7.4: $W + \geq n$ jets cross sections compared to theory. The filled circles are the data measurements with the error bars representing the combined statistical and systematic uncertainties. The band indicates the variation of the predictions with the renormalization scale. The $W+ \geq 0$ jet prediction is from a born calculation of inclusive W production.

If the QCD predictions reproduce the jet kinematics accurately the ratio of data to theory is independent of the choice of jet E_T cut so that the quantity may be of more general interest. Although we have measured this ratio for only one jet E_T definition for each $W+$ jet sample, we examine the performance of QCD kinematic predictions through alternate tests in section 7.3.2.

Interpreting the data and theory comparisons that were just described, we see that the absolute cross section predictions agree with the data for n=2 through 4.

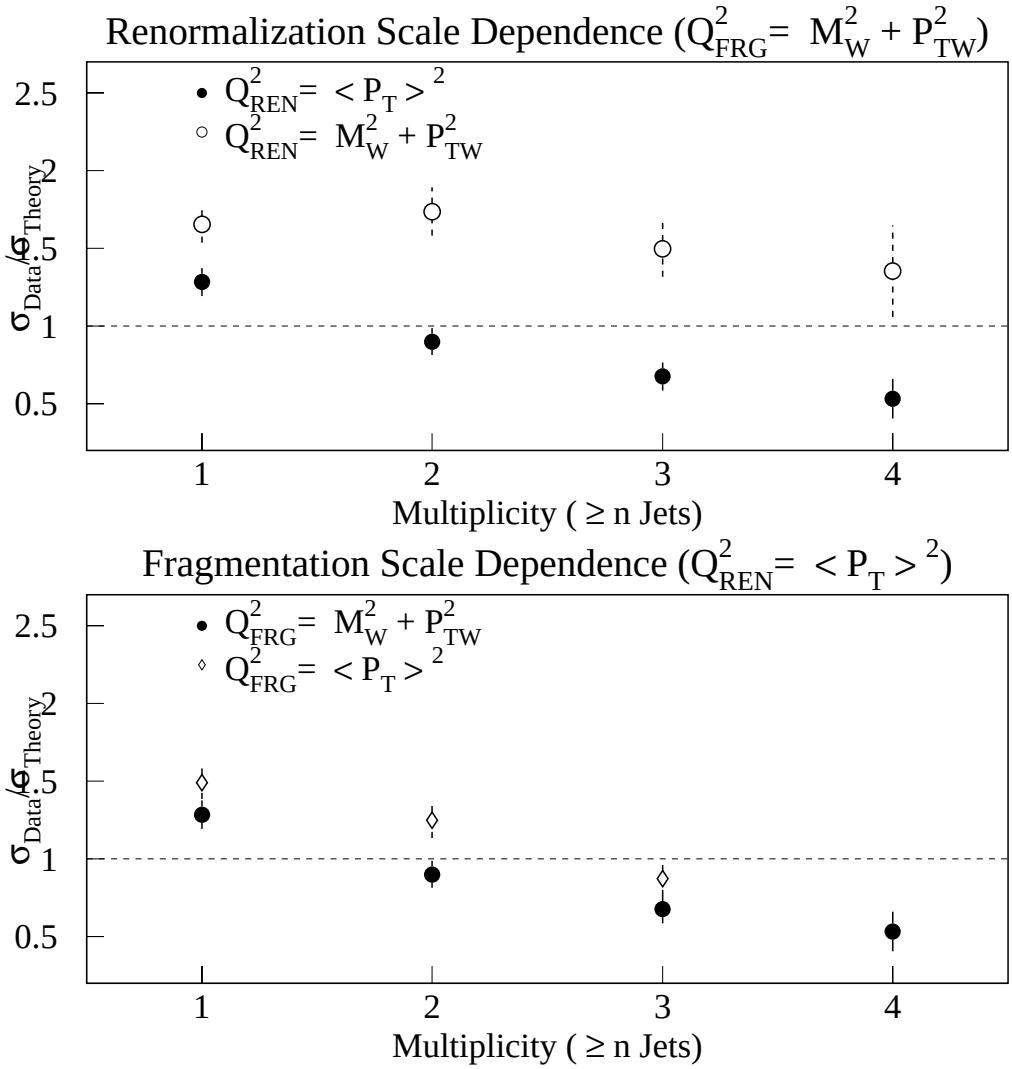

Figure 7.5: The ratio of data to theory for the $W+$ $\geq$n jet cross sections. The horizontal axis is the jet multiplicity. The upper figure compares the ratio for a variation in the renormalization scale. The lower plot shows the results for a variation in the fragmentation scale. The n= 4 point is unavailable for the lower fragmentation scale.

The $W+$ $\geq$1 jet data cross section is a factor of 1.3 high for $Q^2_{ren} = < P_t >^2$ and a factor 1.7 high for $Q^2_{ren} = M^2_W + P^2_{tW}$. The lower renormalization scale agrees better in magnitude, while the higher scale agrees better with the slope of cross section versus the number of jets. The variation of the cross section predictions with the

renormalization scale indicates that higher order corrections to the LO $\geq$1 jet cross section could be of the order of 30%. The QCD corrections to the inclusive prediction are known to be about 20% [37]. Therefore, the lack of quantitative agreement is not a serious concern. The QCD predictions of the absolute cross sections are in agreement with the data given the inherent uncertainty of LO QCD.

The $R_{n(n-1)}$ comparison (figure 7.6) is valid if higher order QCD corrections to the LO cross sections are not strongly dependent on the number of final state partons (i.e. the order of α_s). The ratio $R_{n(n-1)}$ measures the decrease in cross section with the addition of 1 jet. Although not a direct measure of α_s, the value of $R_{n(n-1)}$ is clearly dictated by the magnitude of the strong coupling. Figure 7.6 shows that this ratio is well predicted by QCD and the lower value of α_s is favored by the data (see figure 7.1). This value yields roughly a factor of 5 decrease in the cross section with each additional jet. This decrease in the data actually may show some dependence with the number of jets which is clearly evident in the theory.

One last note on $R_{n(n-1)}$ is that this ratio has been measured for n=1 at the next order (NLO) of perturbative QCD by the $D0$ collaboration [38]. A direct comparison of our data measurements with the $D0$'s data is impossible because of several differences which include: 1) the E_T and η cuts defining a jet are different. 2) the $D0$ analysis uses exclusive (=1 jet, =0 jets) measurements. However, the ratio $R_{n(n-1)}$ at LO and NLO has been produced from the CDF and D0 measurements respectively. The results in reference [38] show a large discrepancy at the next order. Furthermore, the $D0$ analysis showed that the extraction of α_s from $R_{n(n-1)}$ may be practically impossible. The issue here is whether the corrections to the lower order calculations (represented by the so called K factor) are well behaved as a function of the order of α_s. From our examination of the dependency on the renormalization scale at LO as a function of the number of jets, we do not expect large discrepancies at the next

order. These conclusions are admittedly based on enhanced LO predictions with the use of a HERWIG fragmentation model. In any case, the results underscore the need for further examination of perturbative QCD beyond our enhanced LO calculations.

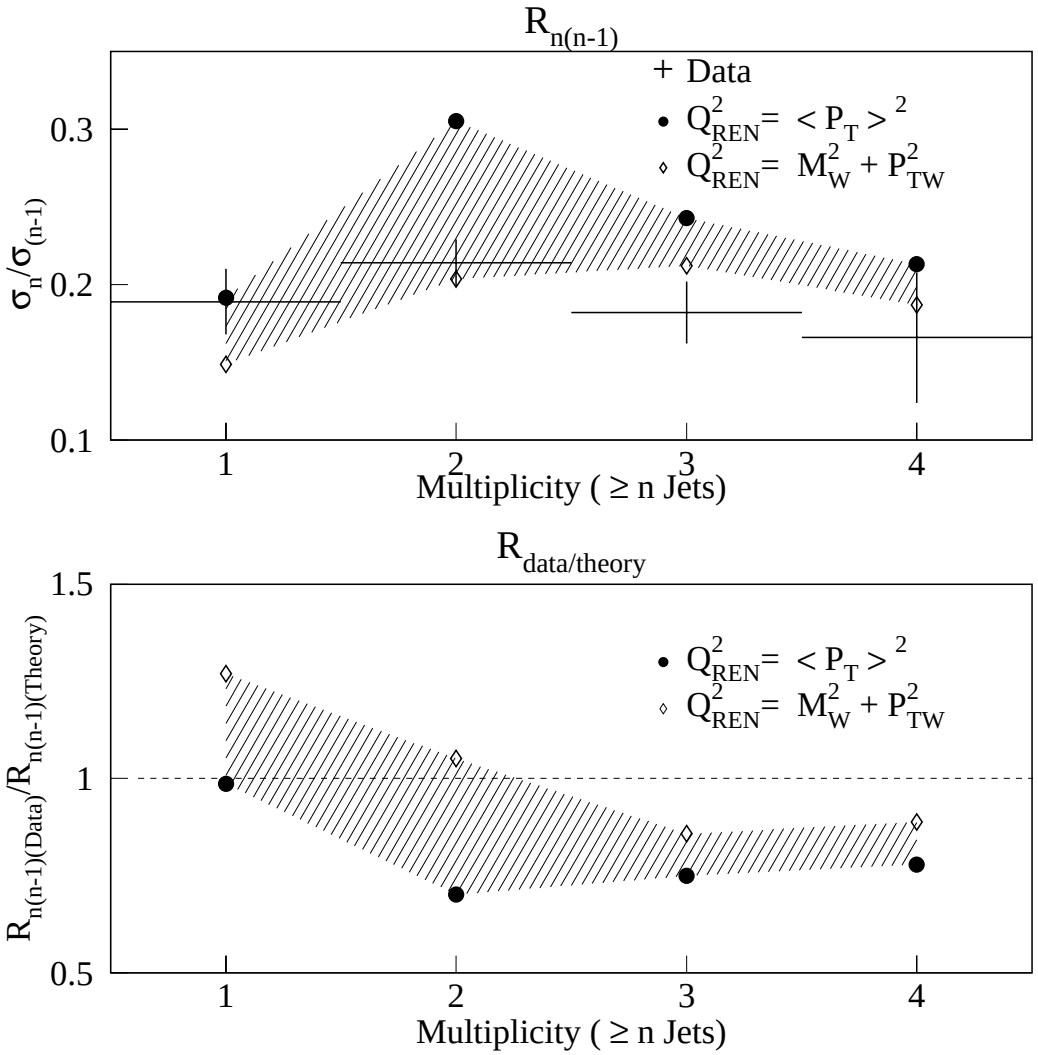

Figure 7.6: The upper plot shows data and theory comparisons for σ_n/σ_{n-1}. The band represents the variation with the renormalization scale. The error bars on the data represent the combined statistical and systematic uncertainty. The lower plot shows the ratio of data to theory of the quantity σ_n/σ_{n-1}. The horizontal axis for both plots is the jet multiplicity.

7.3.2 Kinematic Distributions

Our kinematic distributions will include various jet E_T, mass and angular variables. These distributions have been measured from the $W+$ jet data but were not corrected for variations in the efficiency of W boson identification as a function of the variable that we study. For example, the shape of the jet E_T spectra has some dependence on the geometric and kinematic restrictions on the electron and neutrino used in W boson identification. In order to make a fair comparison we must include this differential efficiency in the theory. This is achieved with the use of a full detector simulation that models the response to all final state particles from $W \rightarrow e\nu$ + jet production. For these fully simulated events we apply our full W selection procedure in order to include the the biases from the use of electron and neutrino cuts.

Before the data are compared to theory, the $W+$ jet kinematic distributions are corrected for the backgrounds that change the shape of the jet spectra. There are three significant backgrounds: promotions, QCD, and top. The top quark contributions are only important in the $W+ \geq 4$ jet distributions. The promotion backgrounds (photons and jets from extra interactions) generally contribute jets at the lowest transverse energies so that that they have a concentrated effect on the jet E_T spectra. Likewise, the QCD background has a significant effect on the low region of the E_T spectra but this is due to a deficit of QCD contribution in this region rather than an excess.

We show in figure 7.7 a shape comparison between the W^+ and W^- data for distribution of the highest E_T jet in an event. The plot shows the fractional difference in the contribution to each bin of the E_T distribution by W^++ jet events and W^-+ jet events. The distributions should be consistent because there is no known physics which could change the shape of one distribution without changing the other. Thus the comparison of figure 7.7 could indicate η assymetries in the detector's jet accep-

tance since W^+'s are produced preferentially in the direction of the proton and W^-'s are produced preferentially in the direction of the antiproton. In figure 7.8 the same distribution is compared for W and Z data [3]. In this comparison, the jet E_T and background systematics cancel except for the QCD background which is negligible in the Z data. There was small but noticeable improvement after correcting the W data for the QCD contribution. LO QCD predicts that the W and Z jet E_T distributions are very similar and we observe this in figure 7.8.

Finally, before we compare data to theory we normalize the theory distributions to the total number of events in the data. The kinematic tests of the theory will therefore explicitly reveal the sensitivity of the kinematic shapes to the QCD parameters that we used as input. The systematic errors in the data distributions are also calculated to only represent the change in the shape of the distributions.

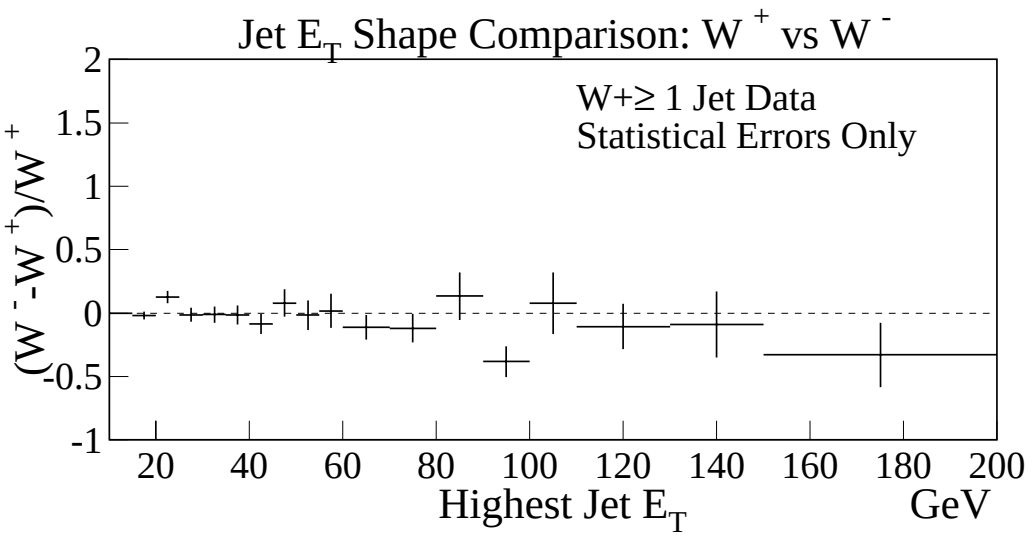

Figure 7.7: The plot compares the jet E_T distributions for the highest E_T jet found in W^+ events and W^- events. The vertical axis represents the fractional difference of events per bin of E_T. The samples are normalized in area to one another before a comparison is made.

[3]The Z data is normalized to the W data for this distribution

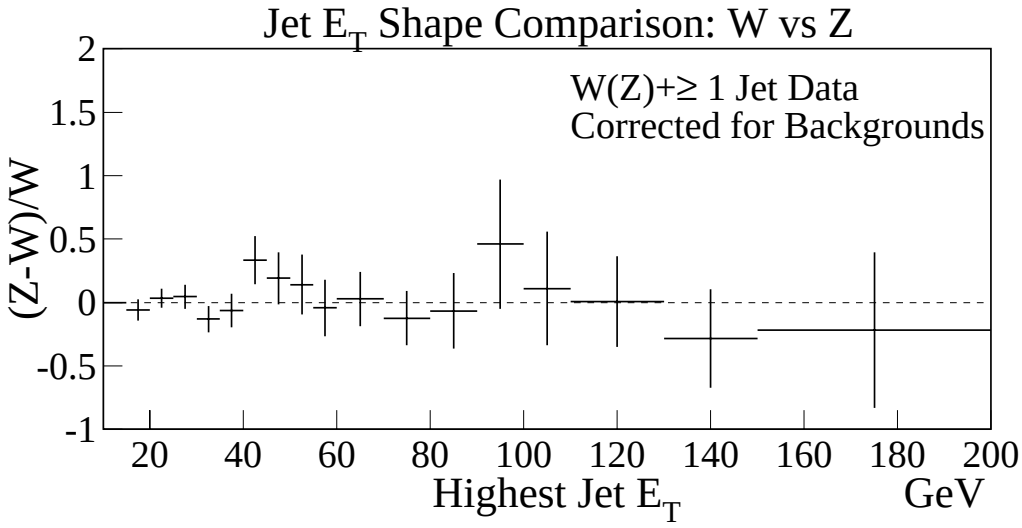

Figure 7.8: The plot compares the jet E_T distributions for the highest E_T jet found in W and Z events. The vertical axis represents the fractional difference of events per bin of E_T. The samples are normalized in area to one another before a comparison is made.

Jet Transverse Energy

We compare data to theory in figure 7.9 for the E_T of the highest E_T jet in $W+$ $\geq$1 jet events, the second highest E_T jet in $W+$ $\geq$2 jet events, the third highest E_T jet in $W+$ $\geq$3 jet events, and the fourth highest E_T jet in $W+$ $\geq$4 jet events. The solid curves are theory for the low renormalization scale and the dotted curves are theory for the high renormalization scale. The curves are fits of an analytic function to the theory histograms. The analytic function was chosen exclusively on its ability to reproduce the theoretical distributions via a minimum χ^2 test.

We can see in figure 7.9 that the sensitivity of the theory to the renormalization scale is mild with respect to the variations in the cross section predictions. However, we expect that the lower renormalization scale yields a softer E_T spectrum because the lower scale weights low E_T events more than the high E_T events. The details of the data and theory comparison for the $\geq$1 jet sample are better seen in figure 7.10. This

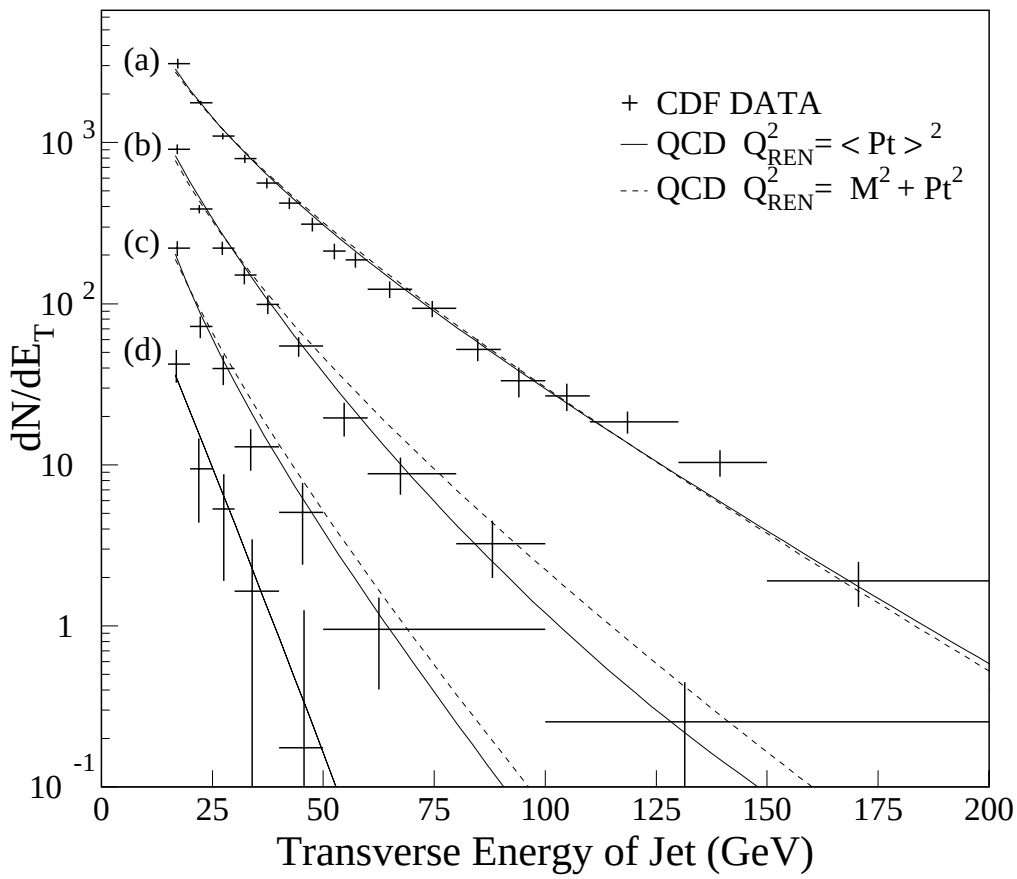

Figure 7.9: The jet E_T distribution for (a) the highest E_T jet in $W+ \geq 1$ jet events, (b) the second highest E_T jet in $W+ \geq 2$ jet events, (c) the third highest E_T jet in $W+ \geq 3$ jet events, (d) the fourth highest E_T jet in $W+ \geq 4$ jet events. The points represent the data and the curves represent the theory. The solid curve is for the lower renormalization scale and the dotted is for the higher renormalization scale. The curves were derived from fits to an analytic function that reproduced the theory well.

plot shows $\frac{\text{data}-\text{theory}}{\text{theory}}$ using the low renormalization scale. The error bars represent the statistical uncertainty while the band represents the systematic uncertainty on the data due to the background corrections and the jet energy uncertainty. We notice deficits in the theory at low E_T and high E_T. The low E_T and high E_T regions of the jet E_T distribution are regions where we expect the theory to be sensitive to higher order corrections.

A detailed examination of the $W+\ \geq 1$ jet E_T distribution reveals several important features. An example is figure 7.11 which plots the fraction of events with exactly 1 jet as a function of the E_T of the highest E_T jet. In the data, as the jet E_T increases, the number of events with exactly 1 jet decreases. In other words, this distribution partially discriminates events based on the their jet multiplicity. In the region where the theory shows a deficit, above 100 GeV, the ≥ 2 jet events are dominant. Therefore we expect that higher order corrections will be significant in the high E_T region.

Partial higher order corrections are provided by the HERWIG parton shower model. Multijet events in the theory receive the extra jets from HERWIG added radiation. Figure 7.11 also shows the 1j fraction for the theory. The first feature to notice is that the addition of HERWIG radiation decreases the fraction of 1 jet events just as in the data. A LO 1 parton calculation alone can not reproduce this feature. The second feature to notice is that the partial higher order corrections provided by HERWIG begin to fail at about the W boson mass energy. The flattening of the 1 jet fraction at high jet E_T can be partially related to the fragmentation scale which limits the energy of the added radiation.

The fragmentation scale we use is a high scale and is equal to $\sqrt{(M_W^2 + P_{TW}^2)}$. The variation of the fragmentation scale was examined in the previous $Z+$ jet analysis where high ($\sqrt{M_W^2 + P_{tW}^2}$) [4] and low ($\sqrt{(< P_t >^2)}$) scales were tested with the $Z+$ jet kinematic distributions. The results favored the higher scale in reproducing the angular distributions of jets in Z events. We examine the effect of the higher fragmentation scale on the comparison of the $W+$ jet E_T distributions by looking directly at the E_T distribution of the jets produced by HERWIG. Figure 7.12 shows the E_T of the highest HERWIG-jet in the $W+\ \geq 1$ jet Monte Carlo. The results are

[4] This scale was referred to as *unlimited* in the Z analysis but since we test an even higher value for this scale we reserve the term unlimited for Q_{frg}=300.0

shown for the default fragmentation scale and for unlimited added gluon radiation. The two scales show agreement up to an energy equivalent of the W mass which is where HERWIG begins to limit the radiation in our predictions. Although the unlimited fragmentation scale better reproduces the data, there remains a deficit of events in the high E_T region. Additionally, the choice to add unlimited radiation is not guided by any physics scales in the $W+$ jet events. A more coherent approach is to obtain the true higher order corrections for the enhanced LO $W+$ 1 jet calculations.

The shape of the jet E_T distribution at low jet E_T is sensitive to backgrounds and the jet energy uncertainty. We have studied the variation of the shape due to these effects and find that they can not account for all of the deficit in the theory (figure 7.10). The shape of theory distribution is also sensitive in this region for two reasons. The added initial state radiation can have a higher E_T than that from the jet initiated from matrix-element parton. This introduces a sensitivity to the fragmentation scale, particularly in regions where the matrix element parton P_T is low. Additionally, hard HERWIG radiation can not only supersede the the matrix-element parton but can promote an event into the sample which previously would be rejected due to the low P_T of the matrix-element parton. This effect introduces an ambiguity in the parton P_T cut used to generate the LO calculation. Above 25 GeV all of these effects reduce and the data and theory are in good agreement.

Summarizing the comparisons of data to theory for the jet E_T distributions, we see that the theory reproduces the data over a large range of jet E_T for all jet multiplicities. Focusing on the $W+ \geq 1$ jet predictions, the theory accurately reproduces the data in those regions where we expect that higher order corrections are small. The partial higher order corrections provided by HERWIG are insufficient in the regions that are dominated by higher order QCD production mechanisms.

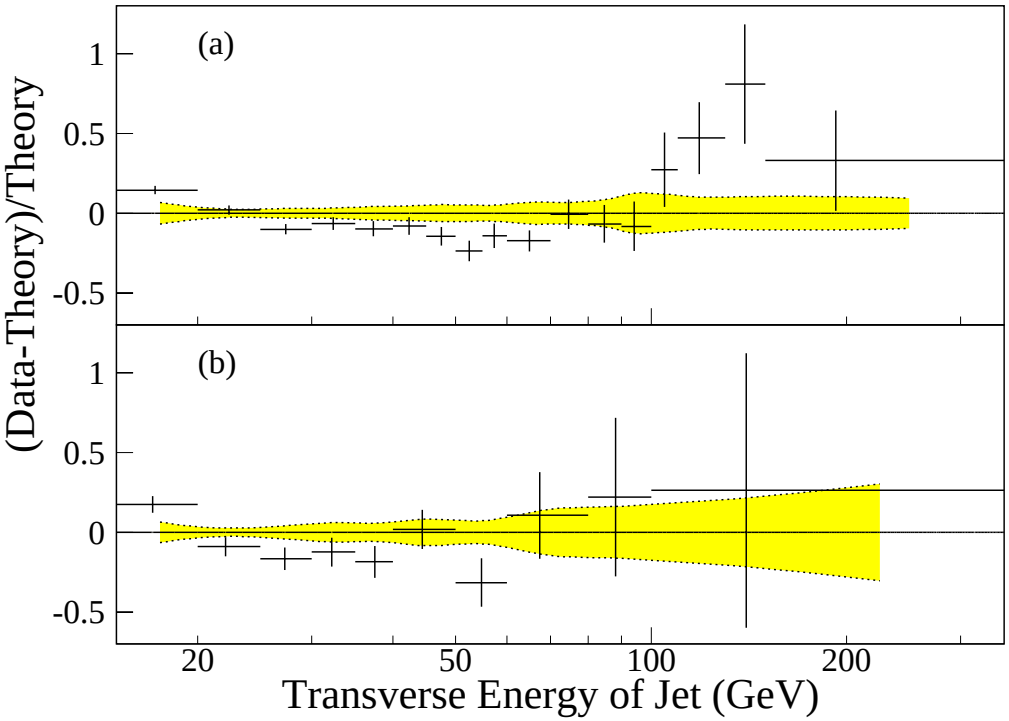

Figure 7.10: Comparison of jet E_T distributions between data and theory. The fractional difference ((data-theory)/theory) verses the E_T of the highest E_T jet in $W+$ $\geq$1 jet events (a) and second highest E_T jet in $W+$ $\geq$2 jet events (b). The theory is normalized to the data before comparison.

Angular and Mass Distributions

The angular correlations of jets are studied with two variables: the dijet invariant mass (M_{jj}) and the dijet angular separation ($\Delta R_{jj} = \sqrt{(\Delta\eta^2 + \Delta\phi^2)}$). In figure 7.13 we show the invariant mass of the two highest E_T jets in the $W+$ $\geq$2 jet sample (top-left) and the W + $\geq$3 jet sample (bottom-left). On the right side of this figure is the jet-jet separation (ΔR_{jj}) for the two highest E_T jet events in the $W+$ $\geq$2 jet sample (top) and $W+$ $\geq$3 jet sample (bottom).

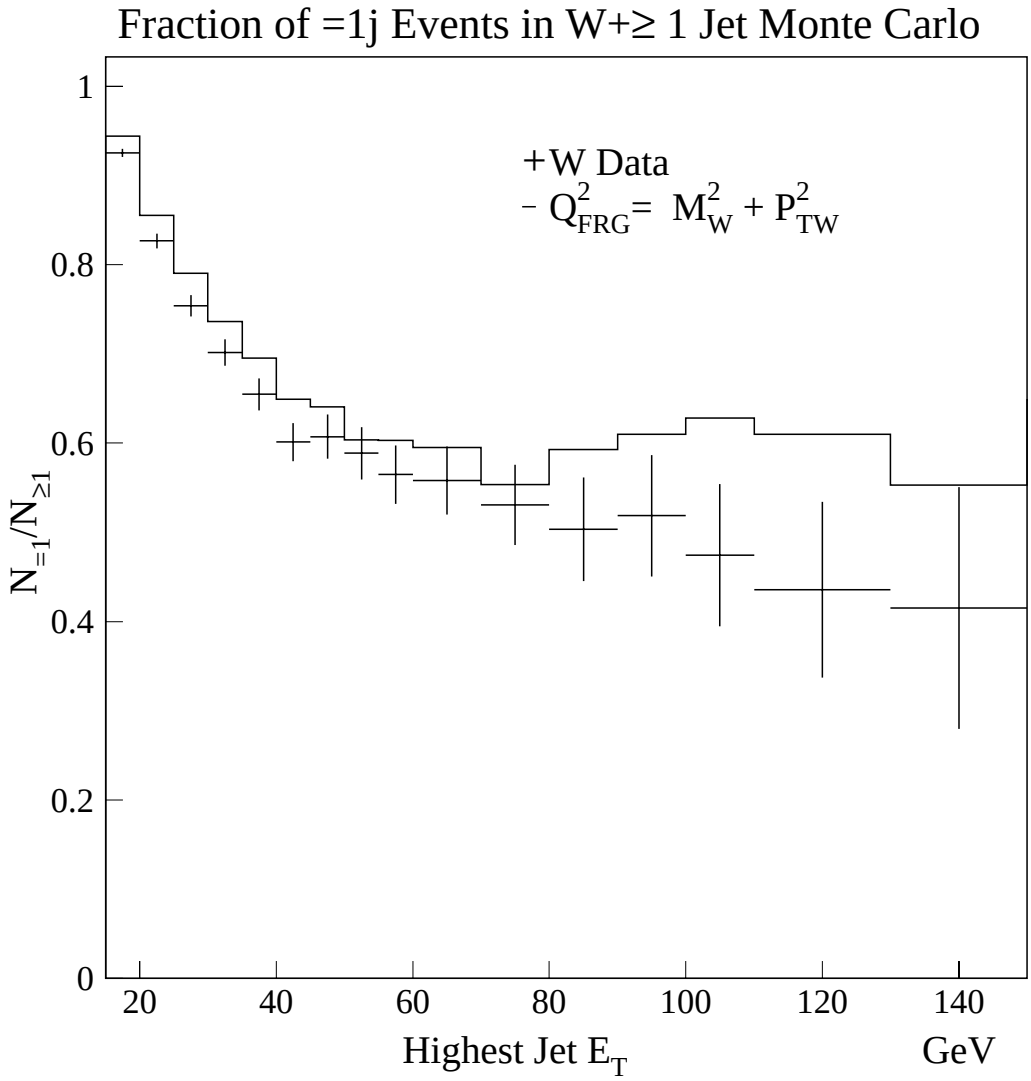

Figure 7.11: The fraction of =1 jet events in ≥1 jet events versus the E_T of the highest E_T jet.

The dijet invariant mass spectra of figure 7.13 are qualitatively well reproduced by the QCD predictions. We do note a harder mass spectrum for both renormalization scale choices. The distribution is better produced by the low renormalization scale. Since the mass distribution is not completely uncorrelated with the E_T distributions that were discussed earlier, a more reliable test of the angular correlations is given by the ΔR_{jj} distributions. ΔR_{jj} is the angular separation of two jets in η-ϕ space

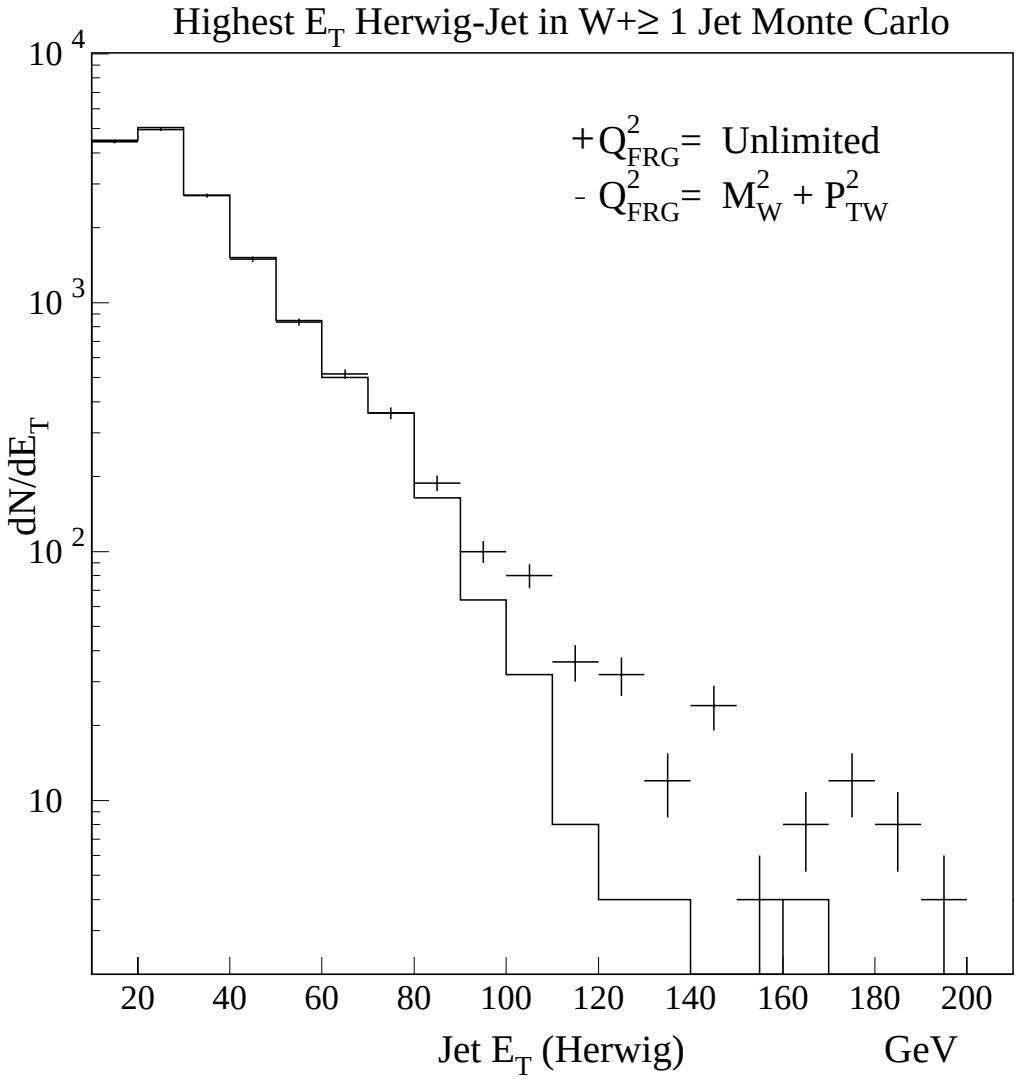

Figure 7.12: E_T of highest E_T jet from HERWIG. The histogram shows the distribution with Q^2_{frg}=$M^2_W + P^2_{tW}$. To generate the points we ran with essentially no limit on the radiation ($Q^2_{frg} = 300^2$).

(ΔR_{jj}=$(\Delta\eta^2 + \Delta\phi^2)^{1/2}$). The jet–jet separation is insensitive to the renormalization scale and shows excellent agreement with the data for both the $W+$ $\geq$2 jet data and $W+$ $\geq$3 jet data. Uncorrelated jets will peak at a value of ΔR_{jj} equal to about π. Therefore the low region of the ΔR_{jj} distribution provides the clearest test for QCD predictions. This region consists of 2 jets separated by a small angle. These are

referred to as collinear jets. We can observe collinear jets to a small separation of 0.52 because we use the small clustering cone for identifying jet clusters. In figure 7.13, we see that the theory predictions for the rate of collinear jets remains valid to the resolution limit of jet-jet separation for our analysis.

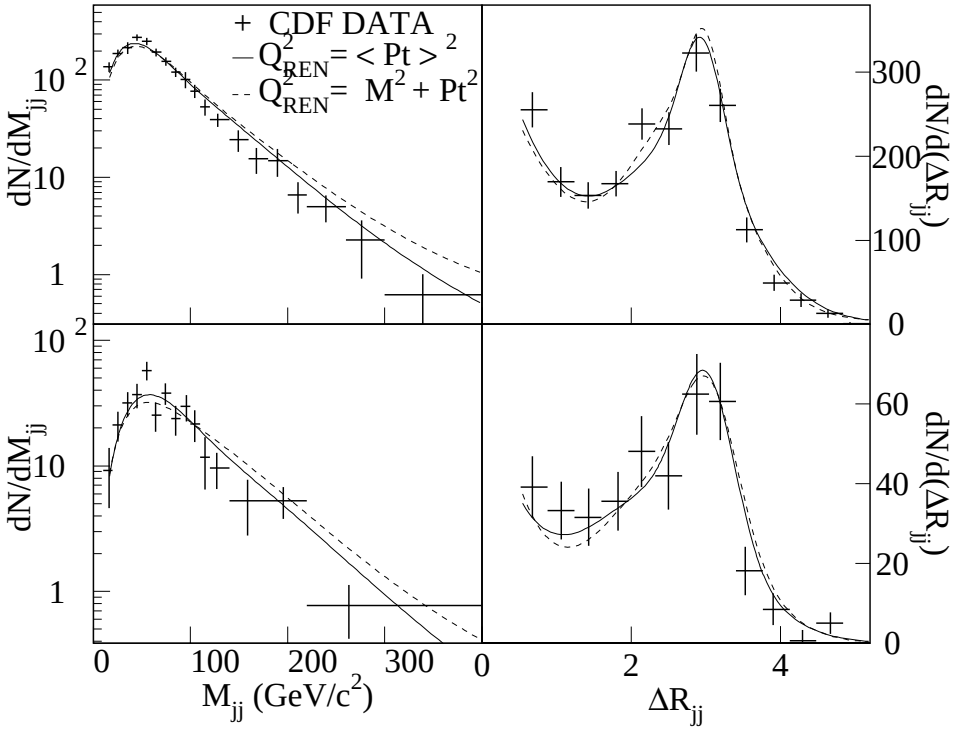

Figure 7.13: The plots on the left show the distributions for the invariant mass of the two highest E_T jets in $W+ \geq 2$ jet events (top) and $W+ \geq 3$ jet events (bottom). The plots on the right show the separation (ΔR_{jj}) in $\eta - \phi$ space for the two highest E_T jets in $W+ \geq 2$ jet events (top) and $W+ \geq 3$ jet events(bottom). $\Delta R_{jj} = (\Delta\phi^2 + \Delta\eta^2)^{1/2}$

7.4 Conclusions

We have measured $\sigma(W) \cdot BR(W \rightarrow e\nu\ )$ as a function of the jet multiplicity for W bosons produced in 1.8 TeV $\overline{p}p$ collisions. The cross section results were compared to previous $Z+$ jet measurements. Comparing the W to Z cross section ratios to the ratio predicted predicted by leading order QCD has the advantage of cancelling the jet systematics. The data are statistical consistent with the predictions.

The $W+$ jet cross section measurements and jet kinematic distributions were directly compared to enhanced LO QCD calculations of $W+$ jets. Generally, the QCD predictions reproduced the main qualitative features of the data for cross sections and jet kinematics. The comparisons show agreement between data and theory for the $W+\ \geq n$ jet cross section measurements with $n\ \geq 2$. The n=1 predictions are low by a factor of 1.28 ± 0.16 ($< P_t >^2$) and 1.65 ± 0.20 ($M_W^2 + P_{tW}^2$). However, the large variations with the renormalization scale indicate that the higher order corrections to the LO cross sections are substantial.

The ratio of the $W+\ \geq n$ jet cross section to the $W+\ \geq (n-1)$ jet cross section ($\frac{\sigma_n}{\sigma_{n-1}}$) is measured more accurately than the absolute cross sections. The dependence on the renormalization scale for this ratio was smaller. Comparing the ratio removes the normalization difference between the data and theory and focuses on the influence of the strong coupling. The data and theory showed good agreement across all multiplicities where calculations were available (n=1 to 4).

The enhanced LO QCD predictions accurately reproduced the main features of jet kinematics. QCD properly predicted the rate of collinear jets to the smallest angles observed. As with the cross section comparisons the kinematic distributions indicated that some distributions could benefit from true higher order corrections. Specifically, the $W+\ \geq 1$ jet data provided sufficient statistical accuracy for an examination of events with a highest jet E_T above 100 GeV. The highest E_T region is where one

might expect perturbative QCD to perform best. It was shown that this region contained a high concentration of multijet events which require higher order QCD production diagrams for their description.

Appendix A

Calculation of $P_{T\nu}$

A.1 Introduction

We wish to measure the true neutrino transverse energy from all energy found in the detector. This is achieved using the corrected energies from electrons, muons, photons and jets. However, these classifications do not account for all energy in a typical $W+$ jets event. Low-energy depositions are often scattered throughout the detector and must also be used in the missing transverse energy ($\not{E}_t$) calculation. We refer to the low-energy component as unclustered energy. The sources of unclustered energy include underlying event energy from the W interaction, energy from partons which escape the jet clustering algorithm (out–of–cone) and energy from extra interactions. Extra interaction energy is of course not useful in constraining the neutrino energy since it arises from an independent interaction; however, we must accept it since we can not separate it from the W event. Our goal is to measure the scale factor for the unclustered energy.

The first section will define electrons and jets and their energy corrections used in the $\not{E}_t$ calculation. The following sections will describe the unclustered-energy scale factor calculation. $Z \rightarrow e^+e^-$ data are used for this measurement because these events have well-measured electron energy and contain no true missing energy. Along the way we test our procedures with W and Z Monte Carlo events. The W Monte Carlo provides a nice check because we know the true neutrino energy before we process the events with our detector simulation. The Z Monte Carlo is used to calibrate the simulation or more specifically to determine the W Monte Carlo's unclustered-energy scale factor.

A.2 The Components of Missing Transverse Energy

We divide all energy in an event into one of three energy categories: electron energy, jet energy, and unclustered energy. High P_T muons are also defined but are unimportant for the datasets discussed here. From the corrected version of each of the three energies considered here we construct the missing transverse energy vector.

With the assumption that the events we are correcting are $W \rightarrow e\nu$ decays we use the following cuts to define the electron in the event.

- W Missing Transverse Energy Electron Cuts
  - Iso(0.4) ≤ 0.1
  - E_T(corrected) $\geq 20\ GeV$
  - $0.5 \leq$ E/p ≤ 2.0
  - $\mathrm{L}_{shr} \leq 0.2$
  - $|\Delta x| \leq 1.5$ cm (track match)
  - $|\Delta z| \leq 3.0$ cm (track match)

These cuts are a subset of the W electron identification cuts so that all electrons in the W set are treated consistently as electron energy. After the identification of an electron the raw energy of the associated tower cluster is subtracted from the calorimeter data. Underlying event energy is inserted in the electrons former calorimeter towers. We insert 30 MeV per tower which was determined by the average energy in towers away from electron towers in W events ([39]). After the electron is subtracted the jet clustering procedure is executed and jets are obtained with the following definition:

- W Missing Transverse Energy Jet Definition (JTC96S)
  - 0.4 cone
  - no out-of-cone correction
  - no underlying event correction
  - jet transverse energy $\geq 10\ GeV$
  - no η cut

The jets are not corrected for radiation of energy out of the 0.4 cone. This is so we avoid double counting this energy which will appear in our unclustered-energy component. No attempt was made to subtract the underlying event energy from the jet cluster and add it to the unclustered energy. Perhaps this low-energy component should be corrected as the rest of the unclustered-energy component; however, only average corrections can be made for the jets.

After identification of jets in the event we remove the associated raw jet energy from the calorimeter towers. The remaining energy defines the unclustered-energy component and we vectorially sum the individual calorimeter towers to obtain the unclustered-energy vector. A calorimeter tower contributes to this sum if it has at least 0.1 GeV of transverse energy, a threshold designed to match the jet clustering algorithm.

The above procedure results in the identification of the three components (electron, jet, and unclustered) of missing transverse energy. Each component is individually corrected and the vector sum is calculated yielding the $\not{E}_t$

$$\vec{\not{E}_t} = -(\vec{E_{ele}} + \vec{E_{jet}} + K \cdot \vec{E_{unc}})$$

In order to obtain the value of K in this equation we will use a sample of events for which the true $\not{E}_t$ is zero. The Z events satisfy this criterion.

A.3 Determination of the Unclustered-Energy Scale Factor

We use a sample of 6708 clean $Z \rightarrow e^+e^-$ events which are described in our $Z+$ jet analysis [33]. The assumption used in the measurement of the scale factor for unclustered energy is that the P_T of the Z as constructed from the final state electron-positron pair is balanced by the remaining event transverse momentum. The actual variable we use is the projection of the transverse energy onto the angular bisector(η) of the e^+e^- pair. The coordinate system is defined in figure A.1. In this coordinate system the projection of the Z P_T is positive and the projection of the Z recoil is negative. Fluctuations in the measured recoil due to resolution and incoherent energy from additional interactions will average out. These fluctuations will not disappear in the magnitude and would cause the ratio of Z P_T to measured recoil to go to zero as Z $P_T \rightarrow 0$, lowering the measured K factor when averaged over the entire Z data set.

We apply the jet selection criteria defined above to find the jets in the event. All events with jets are rejected from our final dataset so that the only energy balancing the unclustered energy is the well-measured electron energy with positive projection in the η direction.

Figure A.2 shows the mean of the P_η ($P_{\eta\ Z} + K \cdot P_{\eta\ unc}$) distribution as function of the scale factor K. The x-intercept determines the scale factor for the unclustered energy. Our criterion requires that the scale factor be chosen to yield zero for the mean. Figure A.2 also shows the width of the P_η distribution as well as the width of the orthogonal component (P_ψ). We use our measured scale factor to correct the η and ψ components of the Z recoil and plot the average against the Z components in figures A.3 and A.4. Figures A.5 and A.6 shows the same plots but with variations of the scale factor by $+/-$ 25% and $+/-$ 50%.

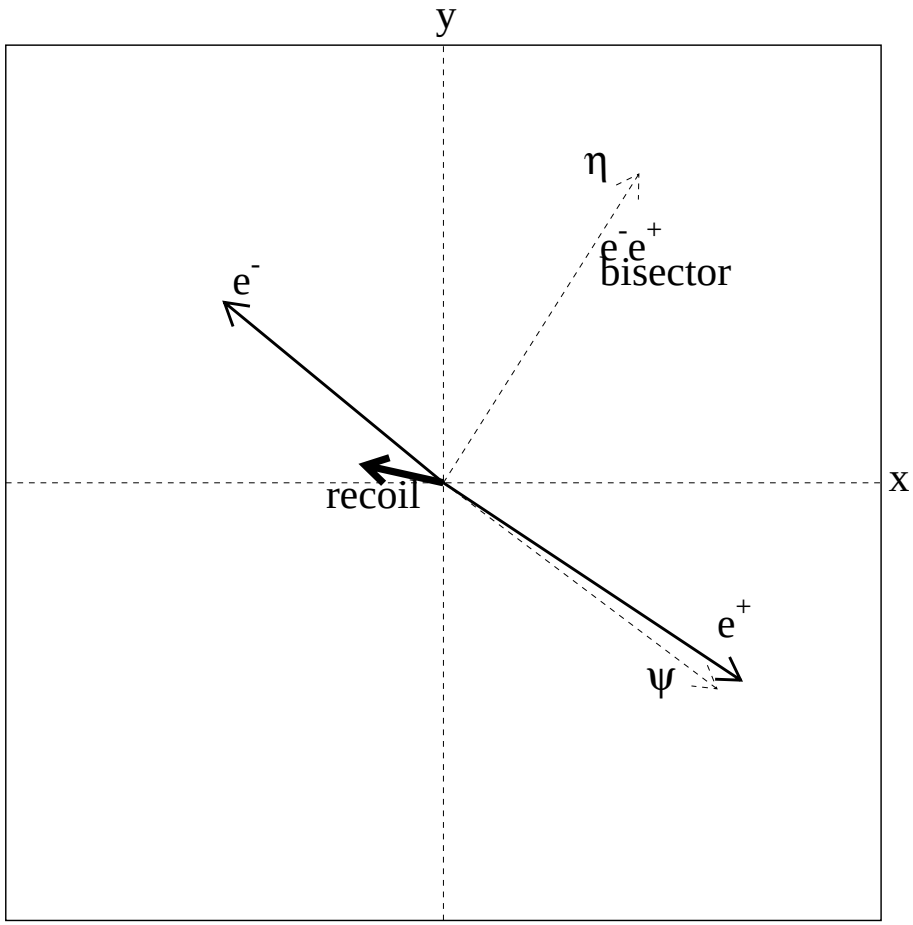

Figure A.1: Shown above is a $Z \rightarrow e^+e^-$event. The length of a vector is proportional to the momentum. The bisector of the angle between the e^+e^- pair is labeled η. This axis is the projection axis for the determination of the unclustered-energy scale factor (K). The orthogonal direction is labeled ψ.

We study the dependency of the measured scale factor and widths on additional smearing due to extra interactions. We use our Z Monte Carlo that has been processed through the detector simulation (QFL) which allows us to use the identical procedure to measure the scale factor for QFL. The results are shown in figure A.7 and figure A.8. For the second plot we introduced additional gaussian smearing of the unclustered-energy components. The magnitude of energy added corresponds

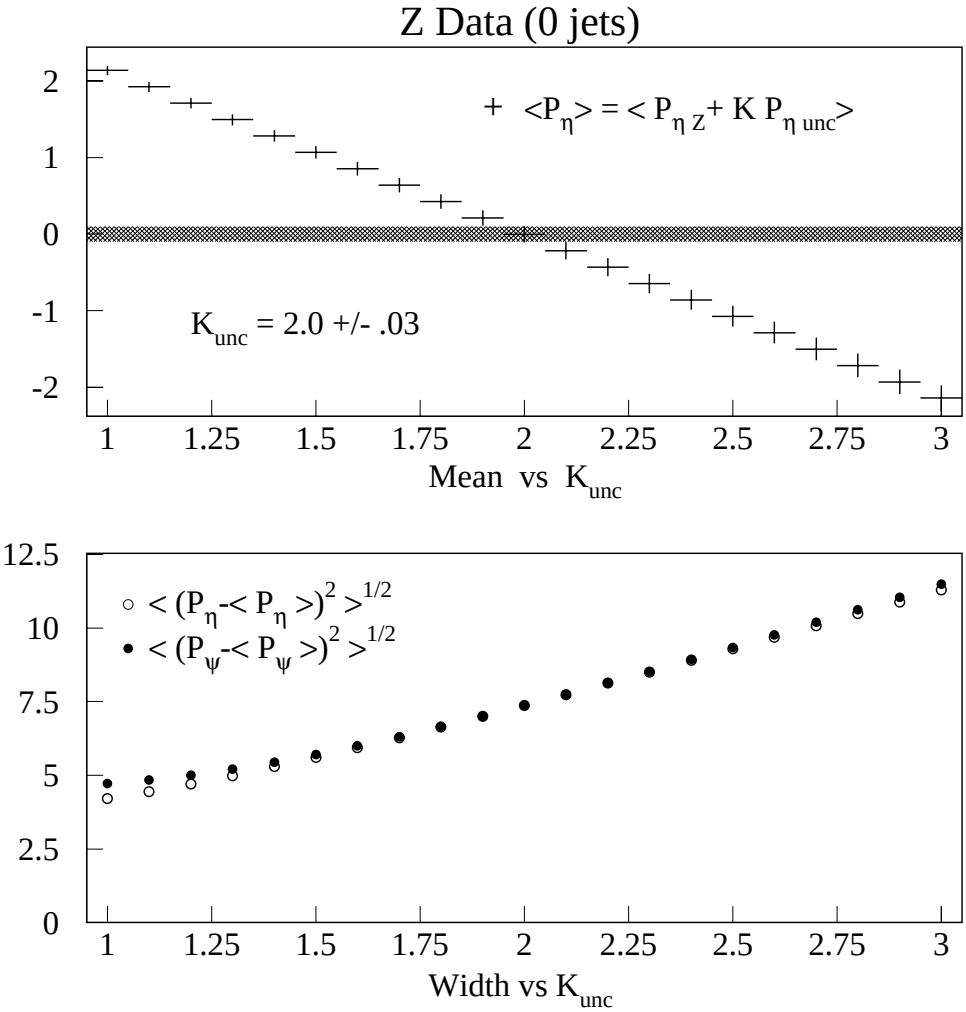

Figure A.2: The upper plot shows the mean of the projection of the Z + recoil for different values of the unclustered-energy scale. The sample is balanced at a scale factor of 2.0. The lower plot shows the corresponding width for the upper plot (open circles) and the width of the projection along the orthogonal direction (ψ see figure A.1)

roughly with the average energy that would be added to an event from extra interactions and is determined from minimum -bias events. We see that the measured scale factor changes by only 0.5% while the minimum of the P_ψ width is sensitive to the smearing ($1.6 \rightarrow 1.25$). Although we can minimize the average difference between true and corrected missing transverse energy with the K factor we do not recover the

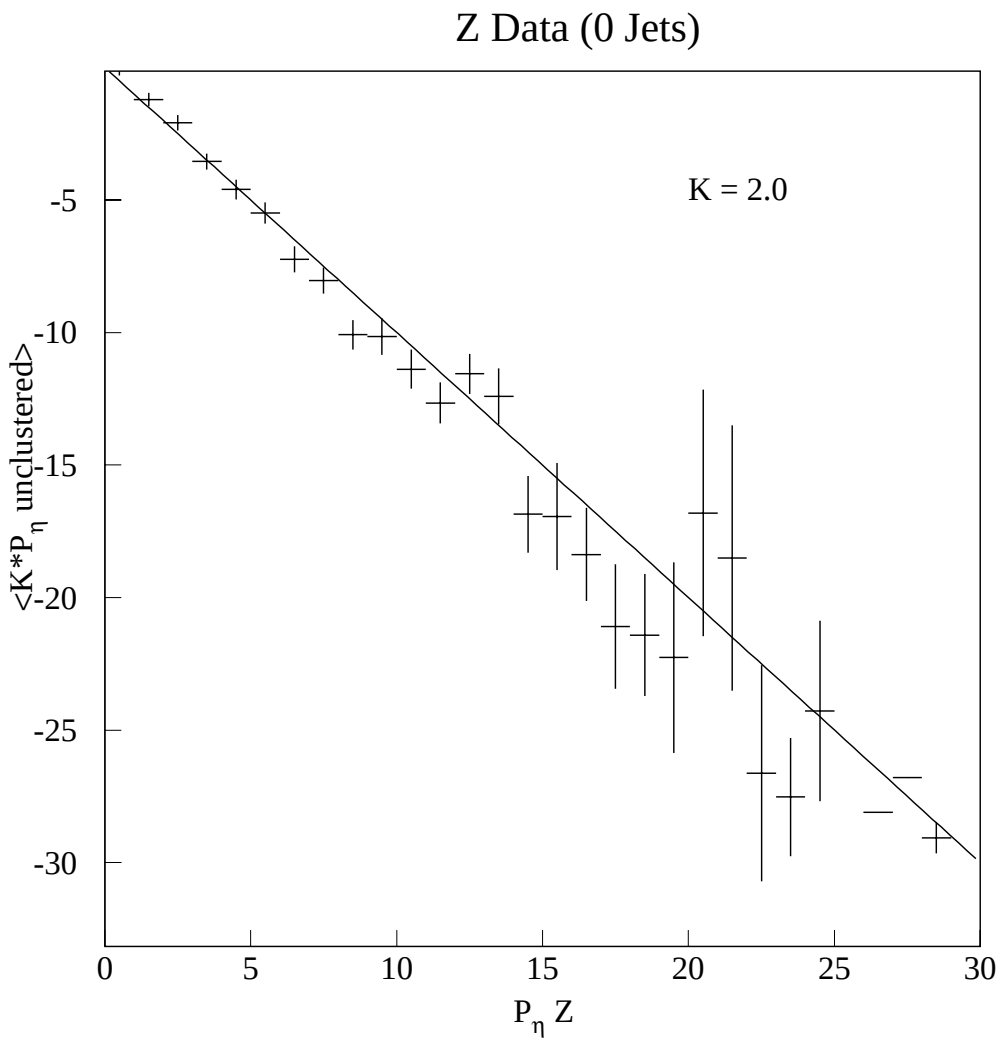

Figure A.3: The average unclustered energy along the η direction versus the η component of the electrons(Z) in the event. The unclustered energy is corrected by a factor (2.0) determined from the components along the η direction.

correct average true neutrino transverse energy. Since we cannot optimize the mean and the width simultaneously with one parameter we explore the variation of the jet energy cut to reduce the width later.

Now that we have obtained a scale factor from the Z Monte Carlo events we can apply it to the W Monte Carlo to check the ability of our procedure to obtain the average true neutrino transverse momentum. Figure A.9 shows the true neutrino

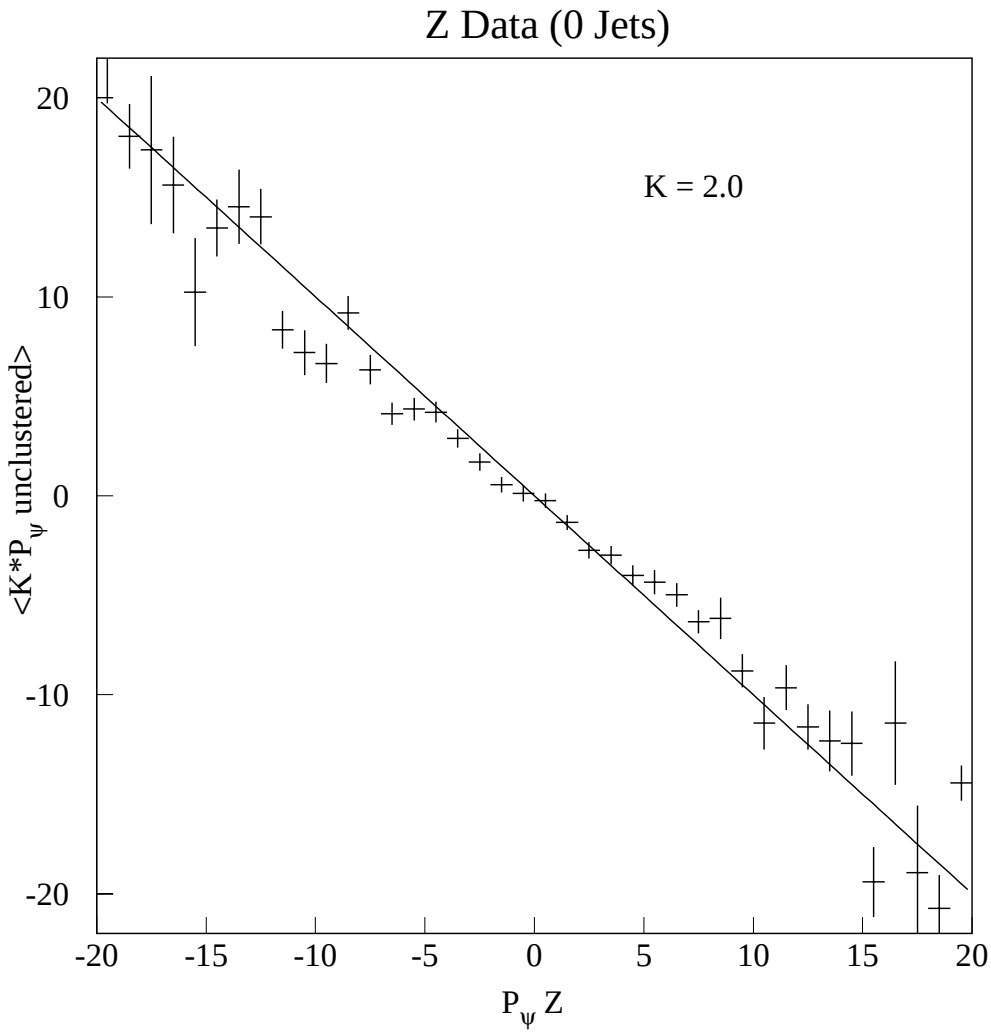

Figure A.4: The average unclustered energy along the ψ direction versus the ψ component of the electrons(Z) in the event. The unclustered energy is corrected by a factor (2.0) determined from the components along the η direction.

transverse momentum along with the measured values for selected ranges of neutrino transverse momentum. The left plot of this figure shows the measured value before any correction is applied which yields higher average measured energies for low $P_{T\nu}$ and lower average measured energies for high $P_{T\nu}$. The right side is corrected $\not{E}_t$ and shows on average the $P_{T\nu}$ is recovered. The measured distributions are shown in figures A.10 and A.11. The insets of these plots show the average measured missing

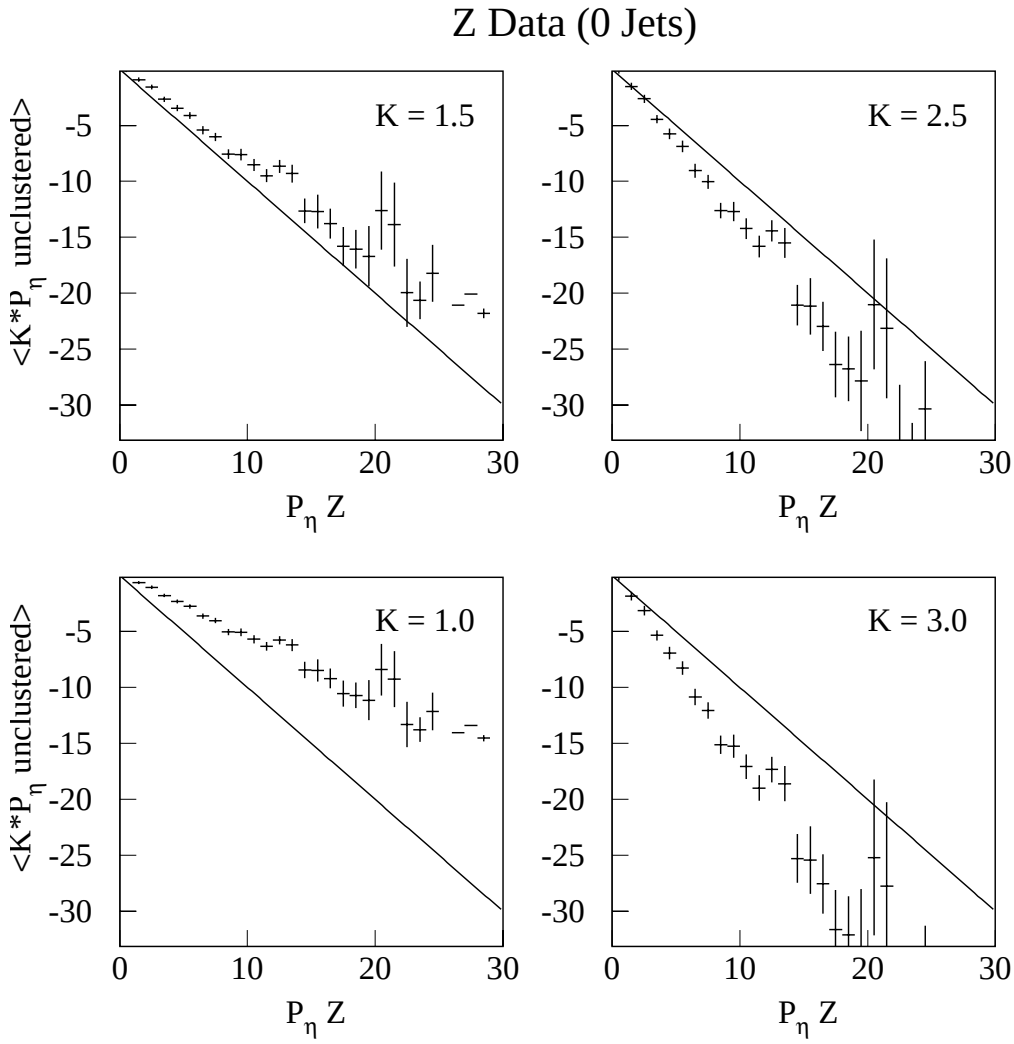

Figure A.5: The average unclustered energy along the η direction versus the η component of the electrons(Z) in the event. The correction factor for the unclustered energy has been scaled by $+/-$ 25% (upper plots) and $+/-$ 50% (lower plots)

transverse energies over the entire neutrino momentum spectrum. We have also varied the scale factor by $+/-$ 25% and $+/-$ 50% in the W Monte Carlo to see the changes in the average versus neutrino transverse momentum. Changes in the scale factor at the 25% level are noticeable in the plots of figure A.12.

It is important to note that the scale factor is dependent on the choice of what defines a jet in the event. The parameter we test is the transverse energy of the

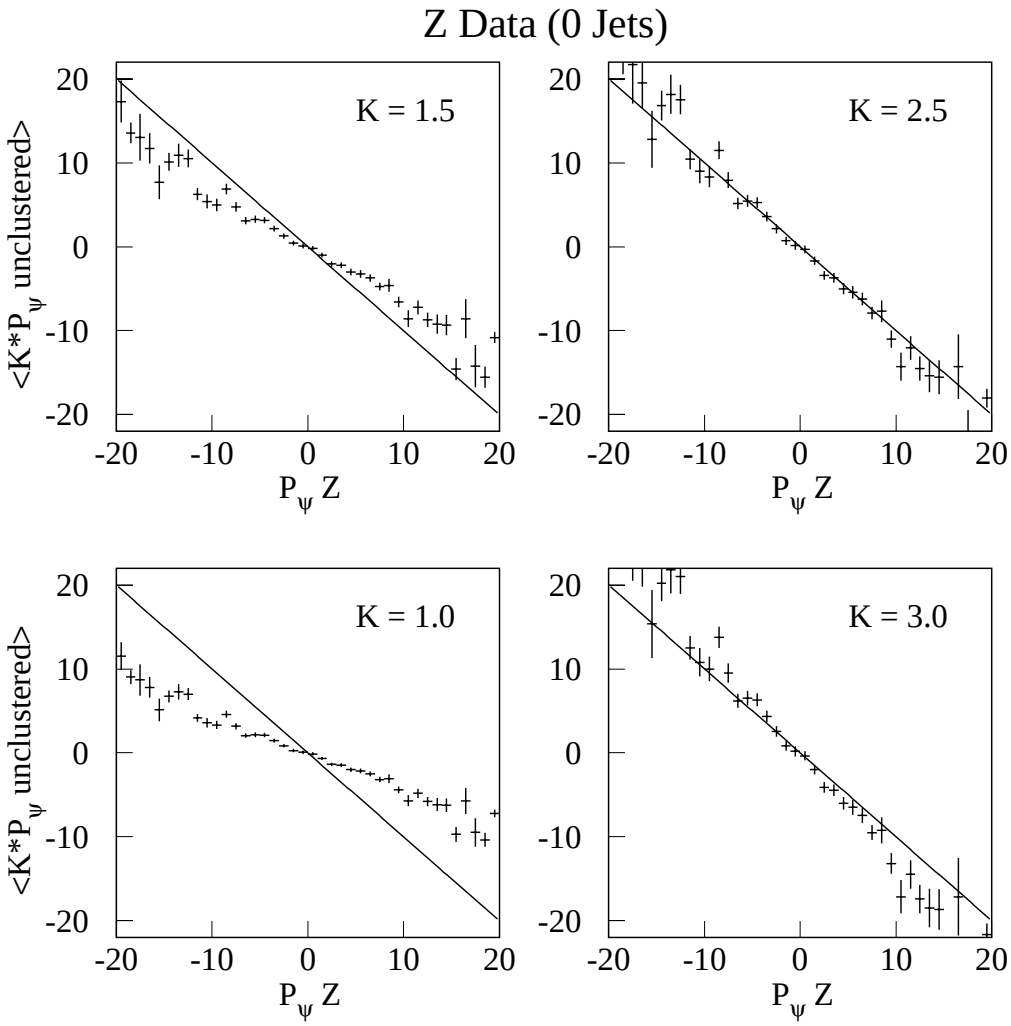

Figure A.6: The average unclustered energy along the ψ direction versus the ψ component of the electrons(Z) in the event. The correction factor for the unclustered energy has been scaled by $+/-$ 25% (upper plots) and $+/-$ 50% (lower plots)

jet. The measured unclustered-energy scale factor as function of the jet energy cut is presented in figure A.13. Here we see that as the unclustered transverse energy becomes more energetic due to the addition of jet clusters the scale factor decreases. The asymptotic value (no jets) is indicated by the line and shows a correction factor of about 1.6 for all non-electron energy in the event. The lower curve shows the average jet correction for jets at the energy of the jet cut. Jets which fall just below

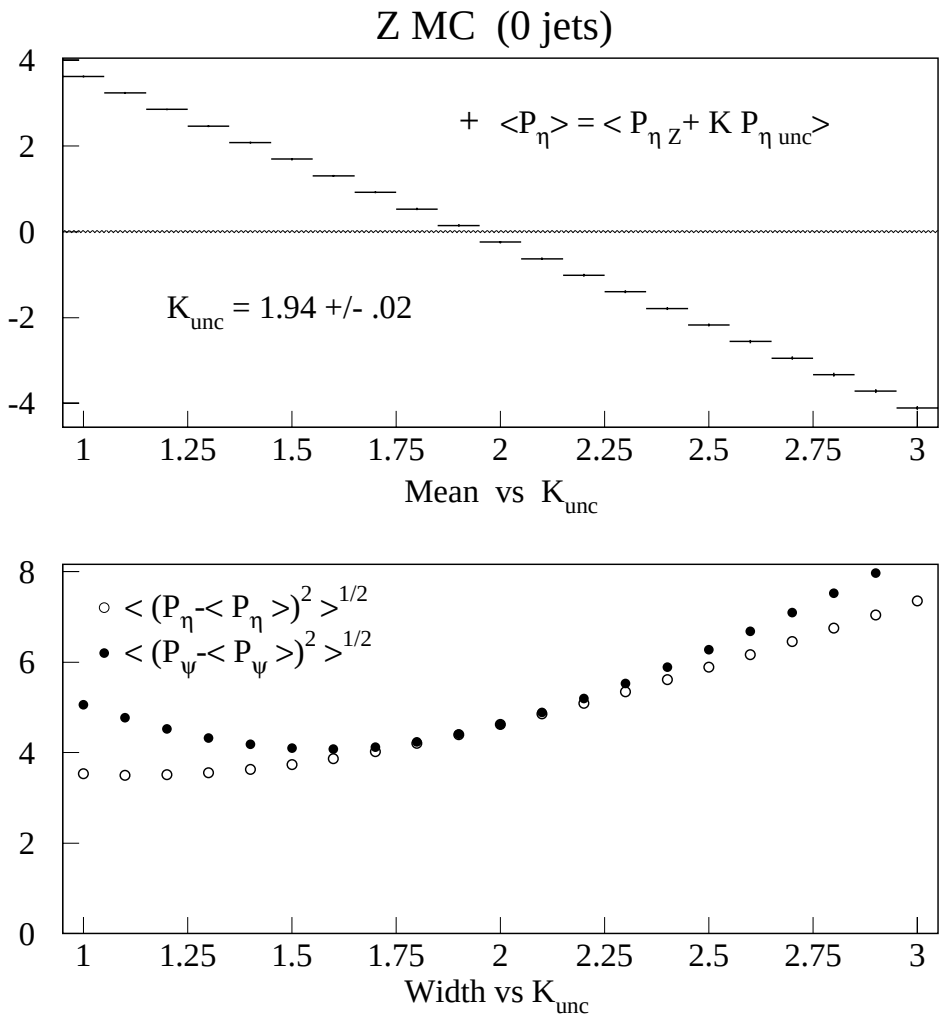

Figure A.7: The scale factor determination for the Z Monte Carlo. The upper plot shows the mean of the projection of the Z + recoil for different values of the unclustered-energy scale. The lower plot shows the corresponding width for the upper plot (open circles) and the width of the projection along the orthogonal direction.

the jet energy cut are not only corrected with only a global correction but the value of the correction is higher than the jet corrections would give. The assumption of a flat response below the jet energy cut requires this to be the case. Figure A.14 shows the difference between true and measured neutrino transverse momentum for corrected $\not\!\!E_t$ based on jet cuts of 10 GeV and 20 GeV. We choose the lowest jet energy cut for our $\not\!\!E_t$ calculation to minimize the average difference between true and measured

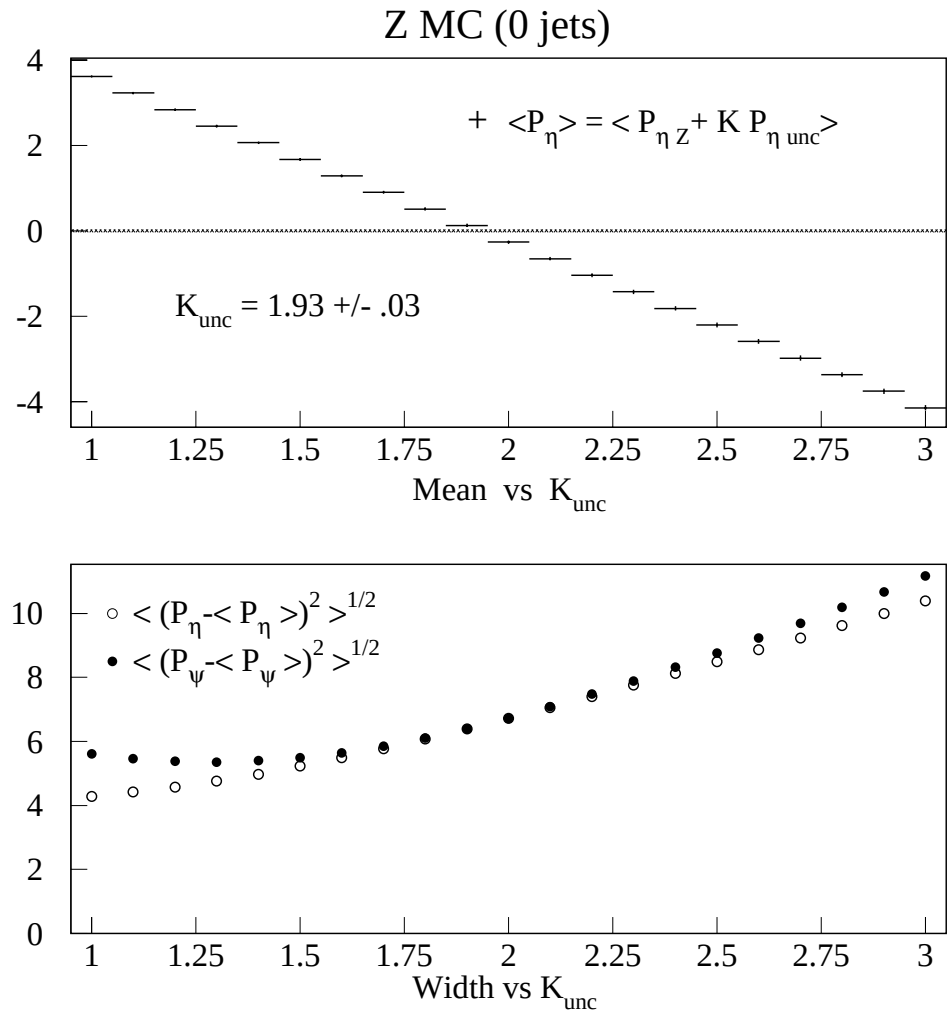

Figure A.8: These plots are identical to figure A.7 except additional smearing was introduced into the Monte Carlo unclustered energy.

missing transverse energy.

A.4 Summary and Conclusions

We have measured the scale factor for unclustered energy using Z events where the P_T of the boson is well measured. The scale factor was determined independent of the Z P_T since this information is not available in W events. The method we chose

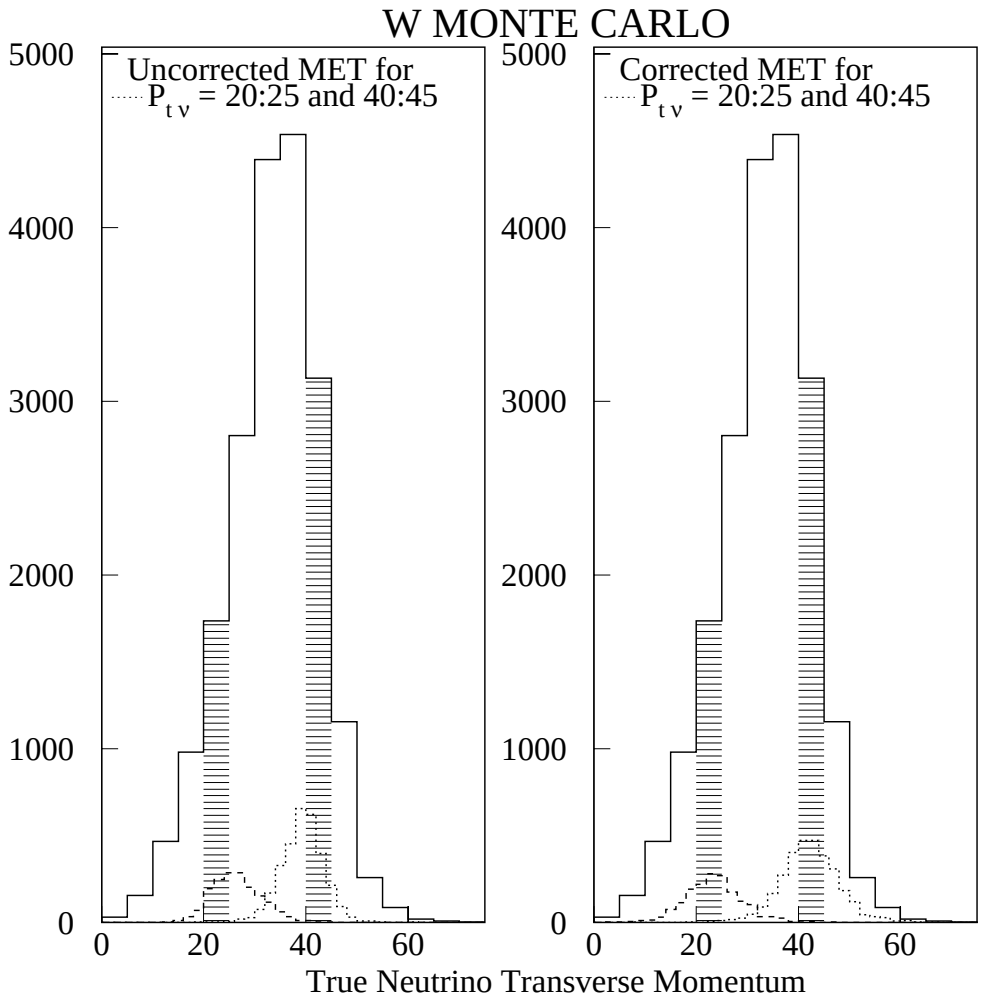

Figure A.9: Shown above is the true neutrino transverse momentum distribution. The measured $\not\!\!E_t$ for the shaded bands in the region 20:25 (dashed histogram) and 40:45 (dotted histogram) GeV are shown on the same plot. The left side is the raw $\not\!\!E_t$ vector the right side is the corrected $\not\!\!E_t$.

yields a value of 2.0 for the scale factor; however, at least one distribution (figure A.6) showed a preference for a higher value of the scale factor. Also the scale factors of 2.0 and 2.5 yield similar results for recovering the true neutrino transverse momentum (figure A.12) but the latter gives a larger spread in the measurement as determined from Monte Carlo studies. We have also tried varying the jet E_T definition in order to reduce the spread and found the correction favored a low jet E_T cut.

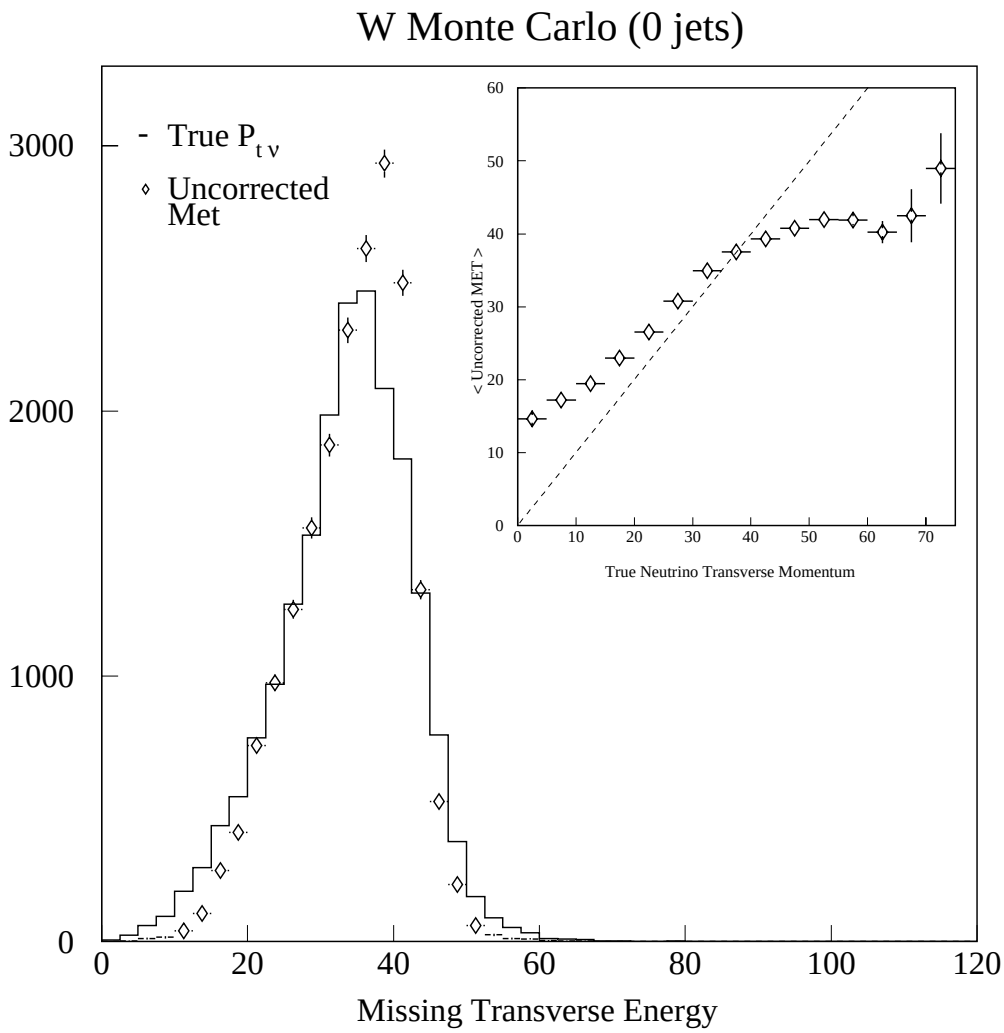

Figure A.10: Shown together are the true and measured (uncorrected $\not\!\!E_t$) neutrino transverse momentum distributions. The inset shows the average uncorrected $\not\!\!E_t$ for a given P_T of the neutrino.

We have chosen to use the corrected $\not\!\!E_t$ in the $W+$ jets analysis instead of the uncorrected $\not\!\!E_t$. There are advantages and disadvantages to this choice. The uncorrected $\not\!\!E_t$ is the vector sum of all raw energy in the detector with no distinction as to the types of energy. This calculation over low-transverse energy neutrinos and thus has a higher efficiency in identifying W candidates. However since we are comparing corrected data distributions to Monte Carlo we prefer to use the corrected $\not\!\!E_t$ for

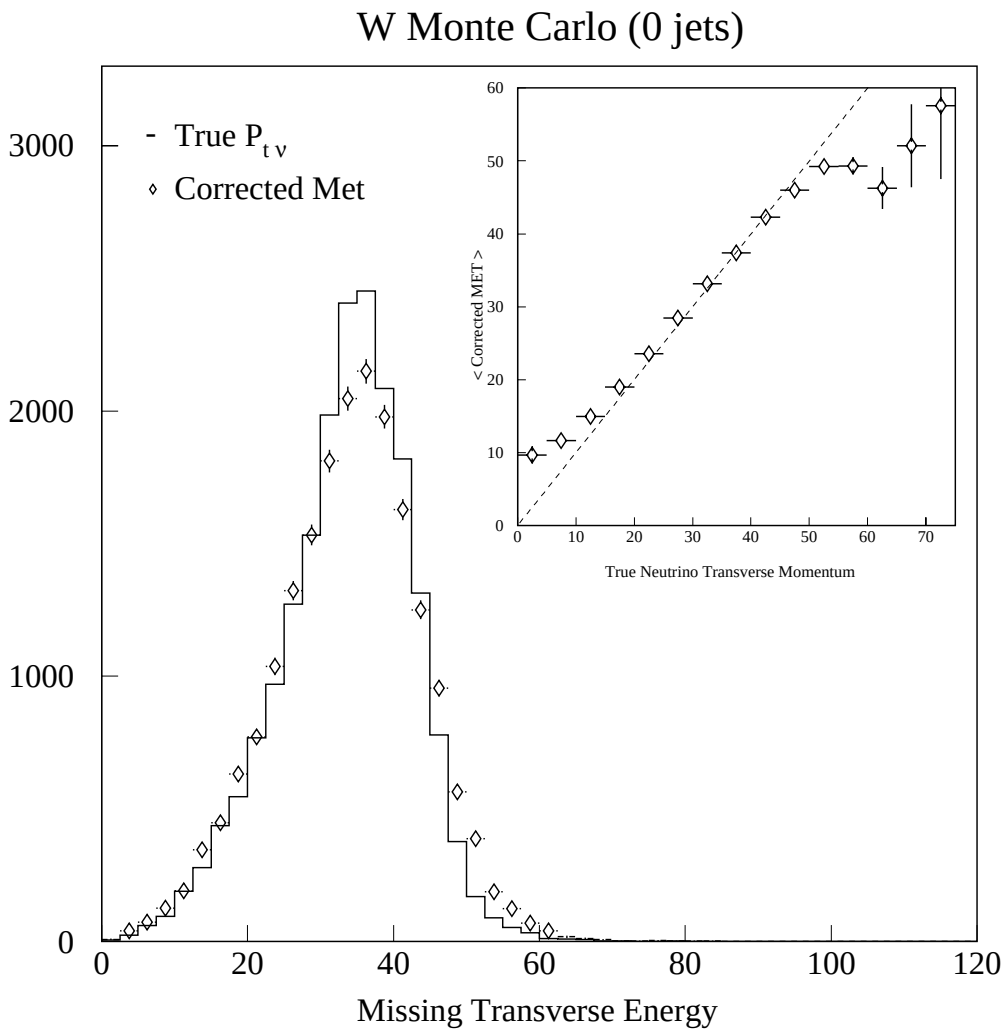

Figure A.11: Shown together are the true and measured (corrected $\not\!\!E_t$) neutrino transverse momentum distributions. The inset shows the average corrected $\not\!\!E_t$ for a given P_T of the neutrino.

selection and displaying data in order to avoid threshold effects from cutting on one variable and plotting another. The calculation of the $\not\!\!E_t$ in W Monte Carlo events relies on the Z Monte Carlo. Thus differences between the detector simulation's and true detector's response to low energy can be taken out more easily than is possible with the uncorrected $\not\!\!E_t$. This feature is utilized in the $\not\!\!E_t$ acceptance calculation. Finally the correlation between the $\not\!\!E_t$ and the isolation of the electron is weaker

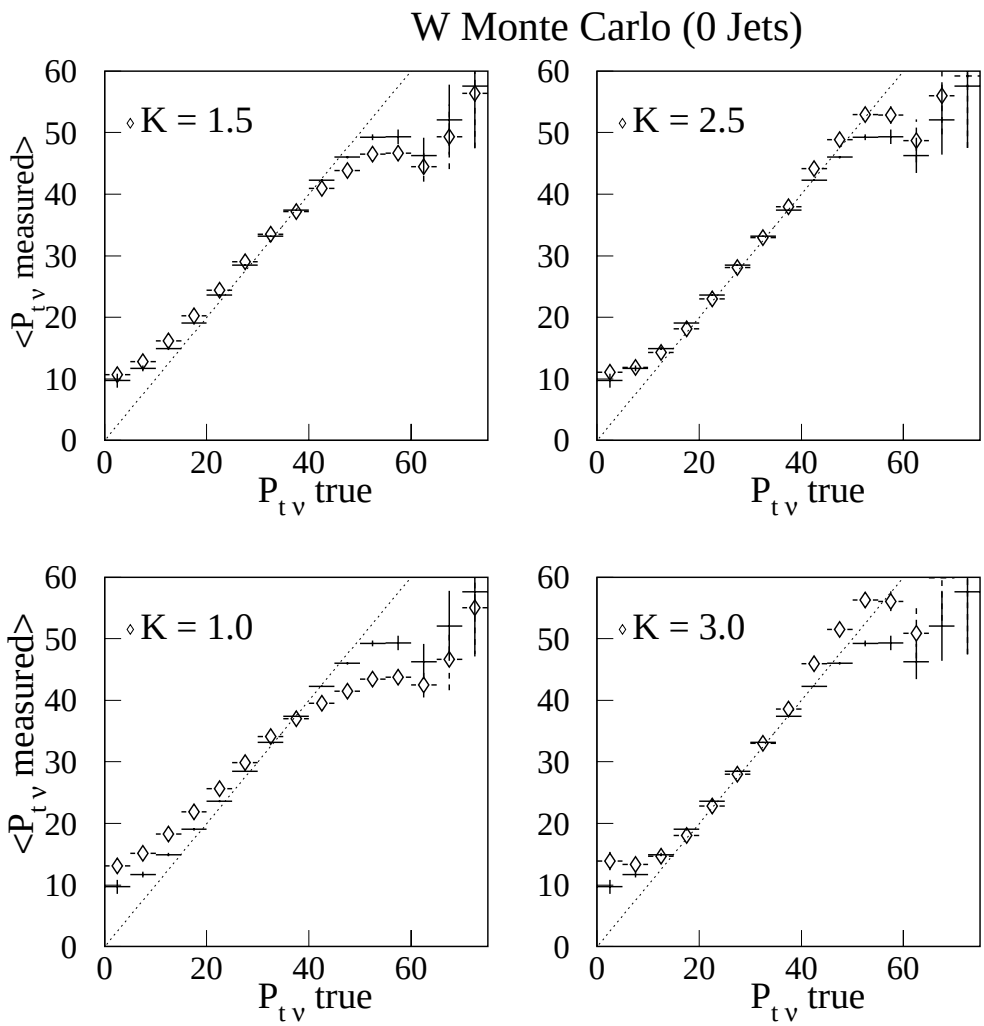

Figure A.12: The average corrected $\not{E}_t$ for a given P_T of the neutrino. The correction factor for the unclustered energy has been scaled by approximately +/− 25% (upper plots) and +/− 50% (lower plots). The crosses are for the default correction factor.

for the corrected $\not{E}_t$ which makes the calculation of the multijet background more reliable.

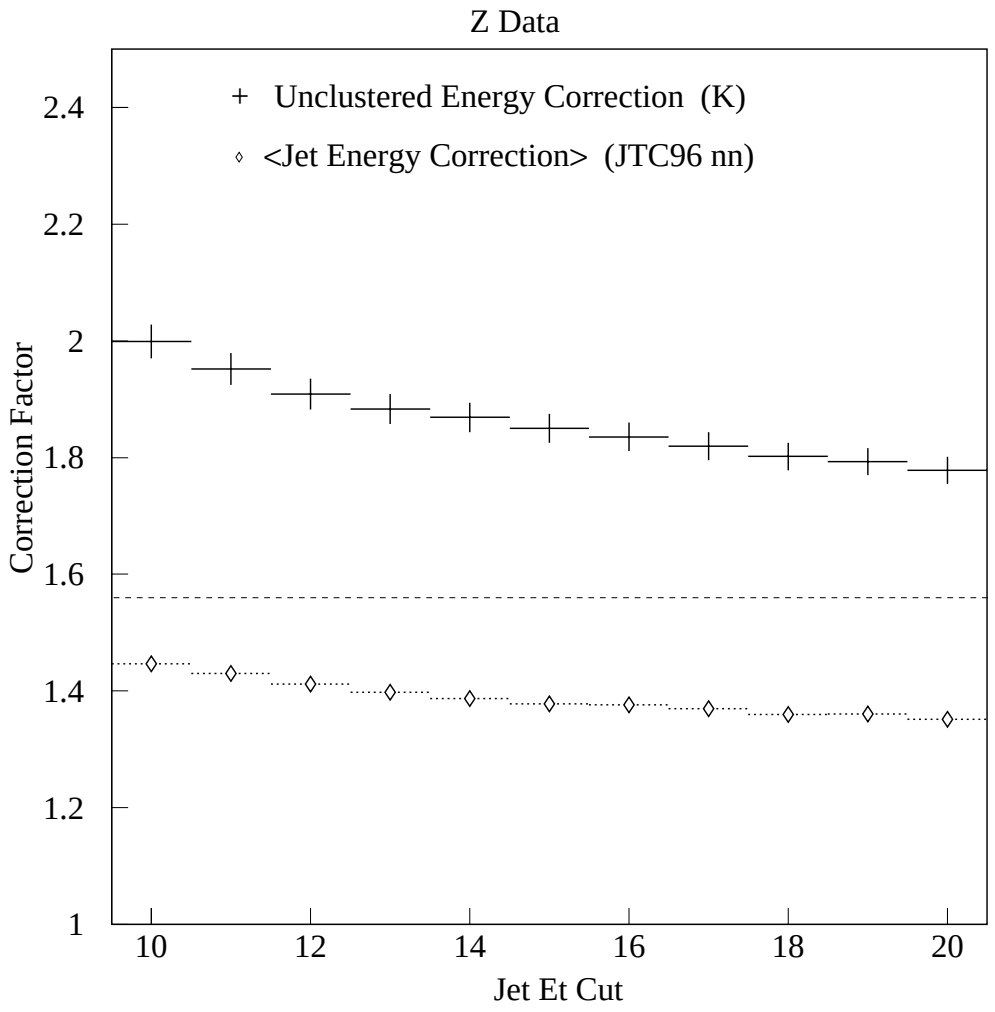

Figure A.13: The correction factor for unclustered energy (crosses) versus the jet energy cut (GeV). The line (~ 1.6) indicates the correction factor which results from treating all non-electron energy as unclustered (no jets). Also shown is the average correction factor (diamonds) for jets at the energy of the jet cut.

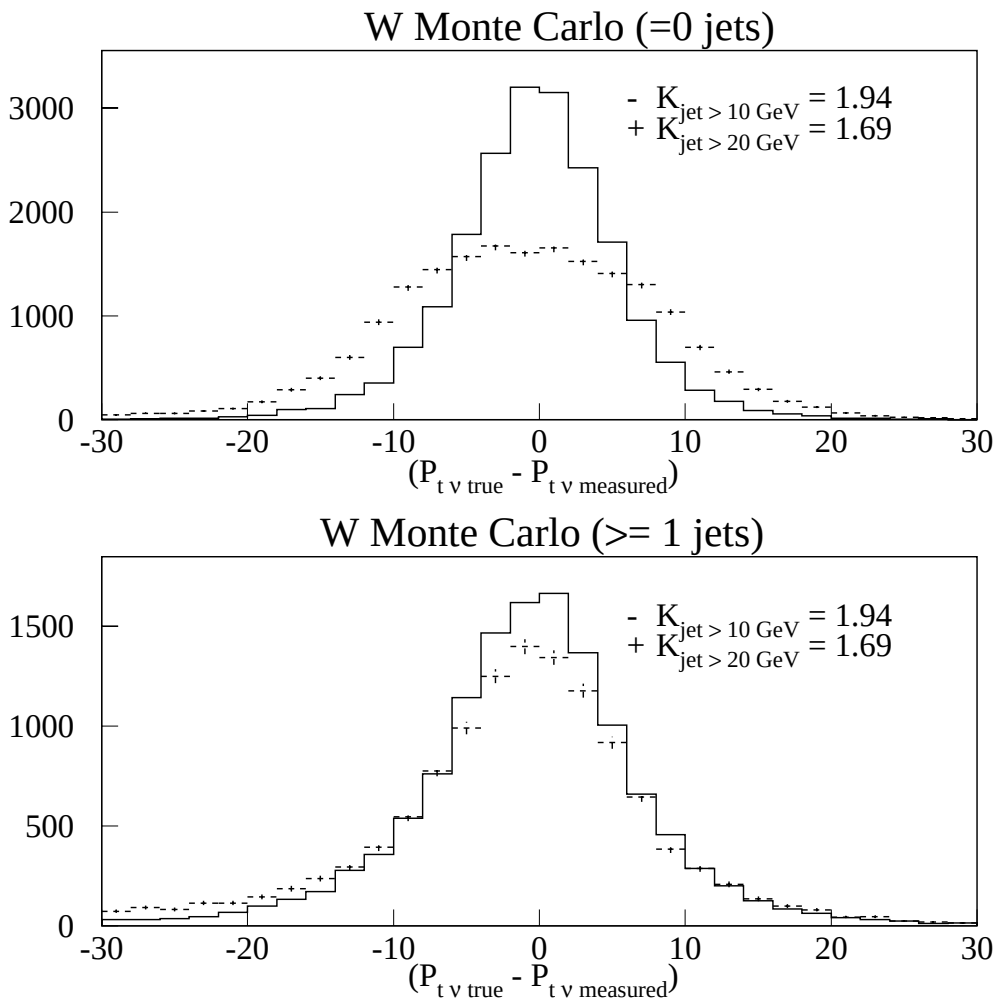

Figure A.14: The difference of true and measured neutrino transverse momentum for two different jet definitions (≥ 10 and $20\ GeV$). The upper plot is for 0 jet events and the lower plot is for events with at least one jet.

Appendix B

The $\not\!\!E_t$ Modeling for Monte Carlo

B.1 The $\not\!\!E_t$ Modeling

We use a corrected $\not\!\!E_t$ which corrects individually for electrons, jets, and unclustered energy (appendix A). The Monte Carlo must simulate each of these energies sufficiently in order to produce reliable acceptance numbers. The QFL detector simulation of electron response and jet response is sufficient for modeling the corrected $\not\!\!E_t$. The unclustered energy is all energy that is not part of a jet or an electron cluster. The sources of unclustered energy can be jets below 10 GeV in transverse energy, underlying event energy from the primary interaction, and extra-interaction energy from events that occur in the same crossing as the W. Our default modeling of $W+$ jets data does not include the last of these sources of unclustered energy. As described in appendix A the correction factor for unclustered energy is 2.0. Any extra energy which is not associated with the W event will be multiplied by this factor; therefore, the smearing introduced from this energy must be examined.

Our tests of the $\not\!\!E_t$ calculation have shown that the energy in minimum-bias events falls almost completely into the category of unclustered energy; therefore, energy associated with extra interactions will show up in the low-energy component of missing transverse energy.. We use our Z data to determine both the level at which we simulate this energy and the effect on the acceptances due to modeling of the unclustered energy.

In Figure B.1 we present the three components of the $\not\!\!E_t$ for both $Z + \geq 1$ jet data and Z Monte Carlo prediction. As seen in the plot the unclustered energy distribution is poorly reproduced by the Monte Carlo. If we select Z events which have no

extra vertices [1] the agreement between Monte Carlo and data improves (Figure B.2). The complement of this sample is shown in the the same figure. This improvement suggests that extra interactions in an event contribute significant energy to the unclustered (or low energy) component. We can try to understand the magnitude of the effect on our W $\not{E}_t$ measurement by reconstructing the E_T of the second Z leg using the central Z leg, the jets and the unclustered energy. This is the Z equivalent to reconstructing the W neutrino transverse energy. This test will not give a reliable estimate of the extra-interaction smearing but will yield a qualitative understanding of the extra-interaction energy. The Monte Carlo comparison to data is shown in figure B.3 and shows this distribution is more robust to the smearing introduced by extra interactions than is the corresponding $\not{E}_t$ plot shown in figure B.4.

[1] A vertex with a high class (12) designation is counted as an extra-interaction vertex. We do not reject events with lower class vertices so that our clean Z sample still contains some extra-interaction energy.

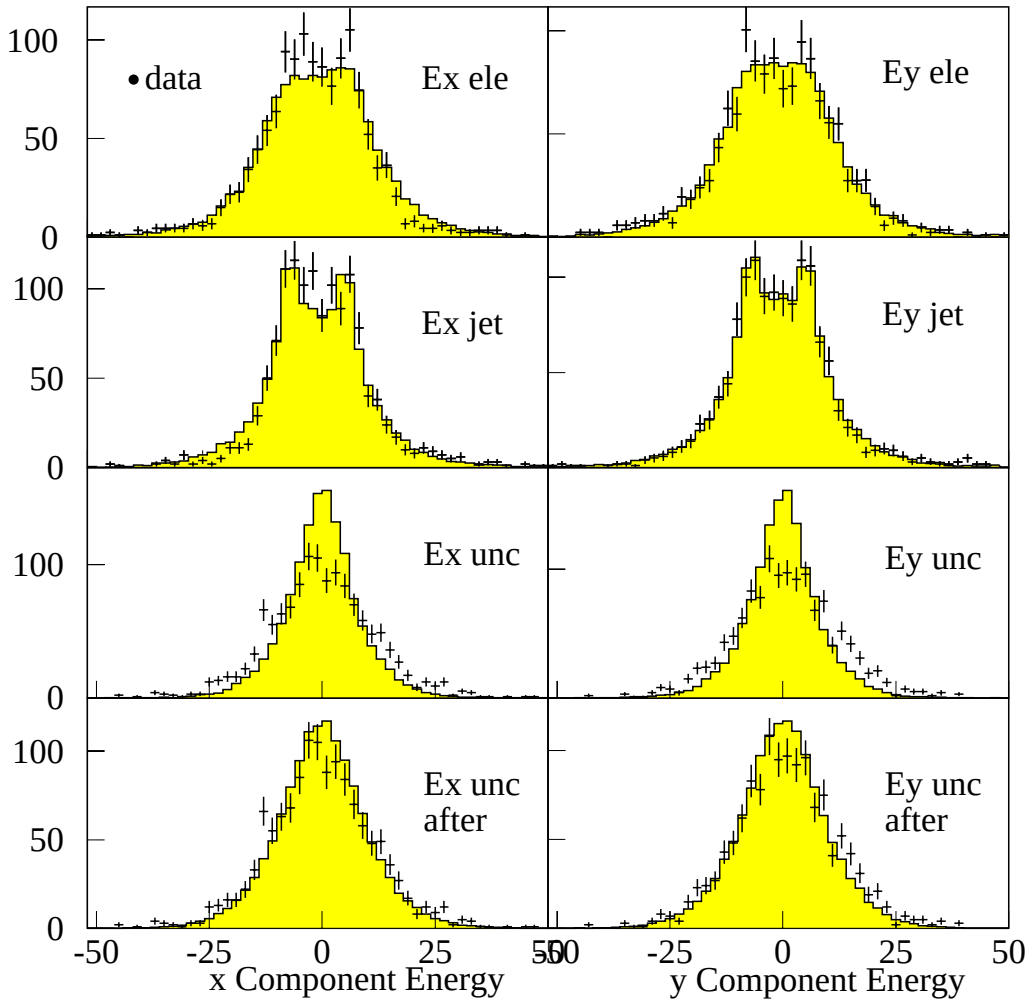

Figure B.1: The left side of the figure shows the x component of energy for electrons (top), jets (2nd from top), and unclustered energy (third from top). The right side is the y component of energy. The bottom plot is the unclustered energy again but with the addition of energy from extra interactions which does not contaminate (significantly) the other two types of energy. The electron energy (data) was corrected for extra interactions which promoted a zero jet event to the 1 jet channel.

To simulate extra-interaction energy we use our luminosity-weighted minimum-bias sample. This minimum-bias distribution does not represent the smearing due to an extra interaction that occurs in the same crossing as the W event because the effect of clustering the extra interaction from the W vertex must be determined. To

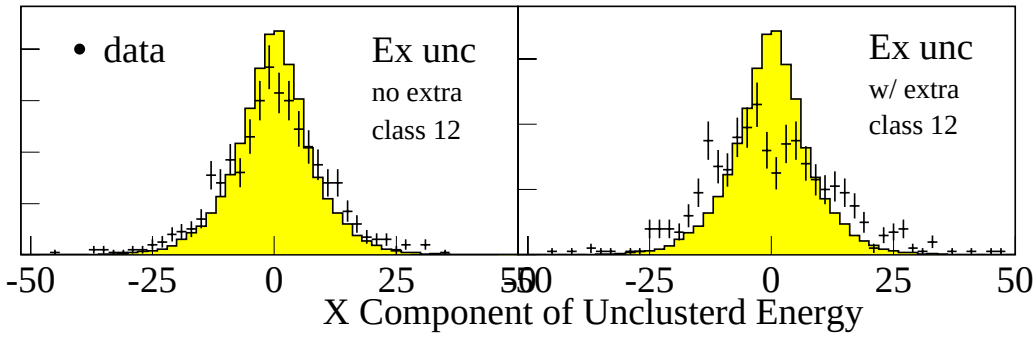

Figure B.2: Plot showing the Z data divided into events with no extra class 12 vertex (left) and events with at least 1 extra class 12 vertex (right).

demonstrate consider a minimum-bias event which is well measured and thus has no imbalance of transverse energy. If the $\not\!\!E_t$ were calculated from a random vertex rather than the true vertex we could create an imbalance of transverse energy. In our W data samples the boson vertex is used as the event vertex. We model the effect of extra interactions by mixing W Monte Carlo events with the luminosity-weighted minimum-bias data and cluster from the boson vertex just as we do in the data. This distribution is shown in figure B.5. When we include the effect of the extra interactions in our Z Monte Carlo the comparison to Z data improves (bottom of figure B.1 and figure B.4). The bottom of figure B.3 is the comparison between Monte Carlo and data of the reconstructed Z leg which also improves after the addition of the extra-interaction energy.

The change in the fraction of events with a reconstructed Z leg transverse energy above 30 GeV is about $-0.45\% \pm 0.05\%$ (figure B.6). Although the shift is small relative to the other systematics in this sample, we have not investigated the effect at every multiplicity with our Z data because we are limited by the statistics at the higher multiplicities. For this reason we include the modeling of extra interactions in our W + jets Monte Carlo samples. The change in the acceptances due to the modeling of extra interactions in our W+ jets are shown in table B.1.

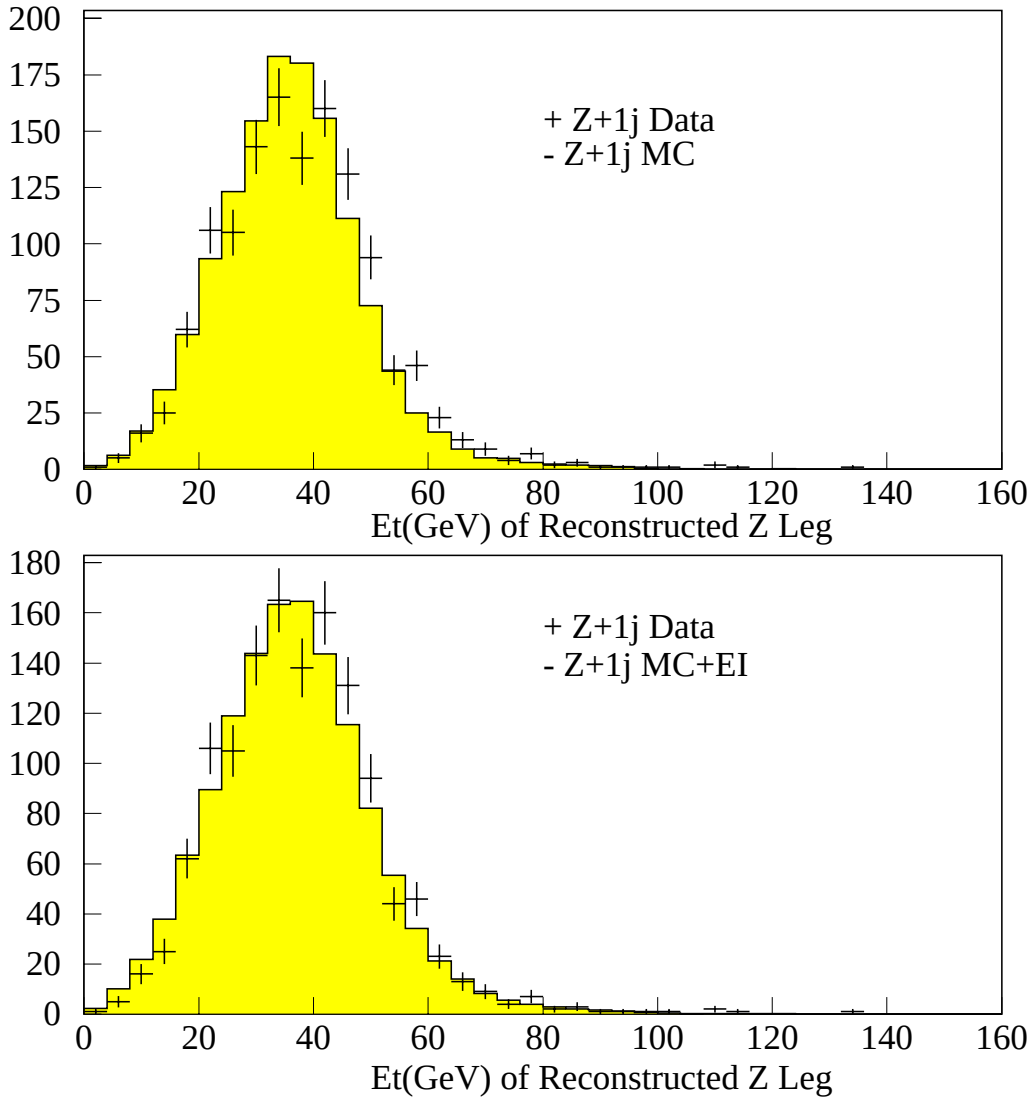

Figure B.3: Ignoring the energy in the second electron cluster we reconstruct the leg with the $\not\!\!E_t$ and first Z leg. The comparison is between Monte Carlo and data. The lower plot includes the simulation of extra-interaction energy in the Monte Carlo.

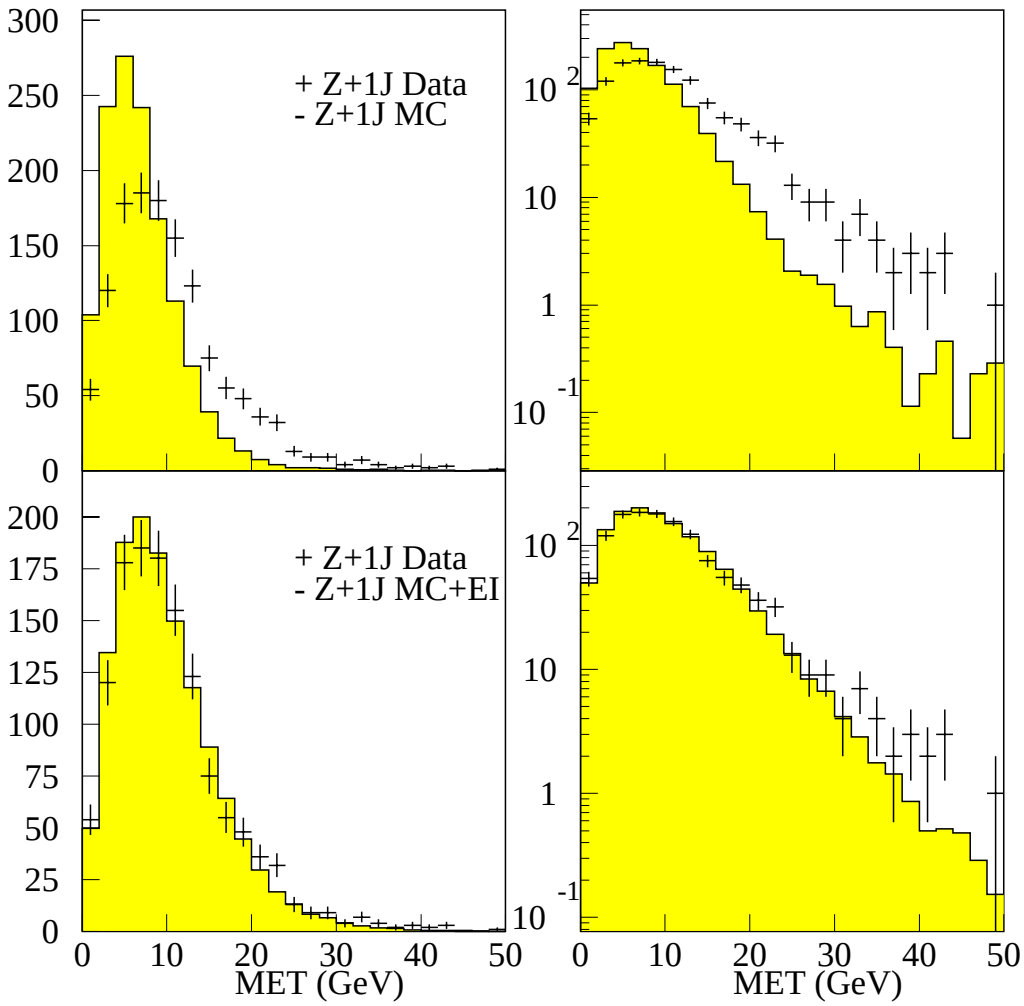

Figure B.4: $\not\!\!E_t$ in Z events. The shaded histogram is Monte Carlo $\not\!\!E_t$ for Z events. The crosses are for actual Z data. The lower plots includes the simulation of energy from extra interactions in the Monte Carlo. The plots on the right are the same as the left-side plots but on a log scale.

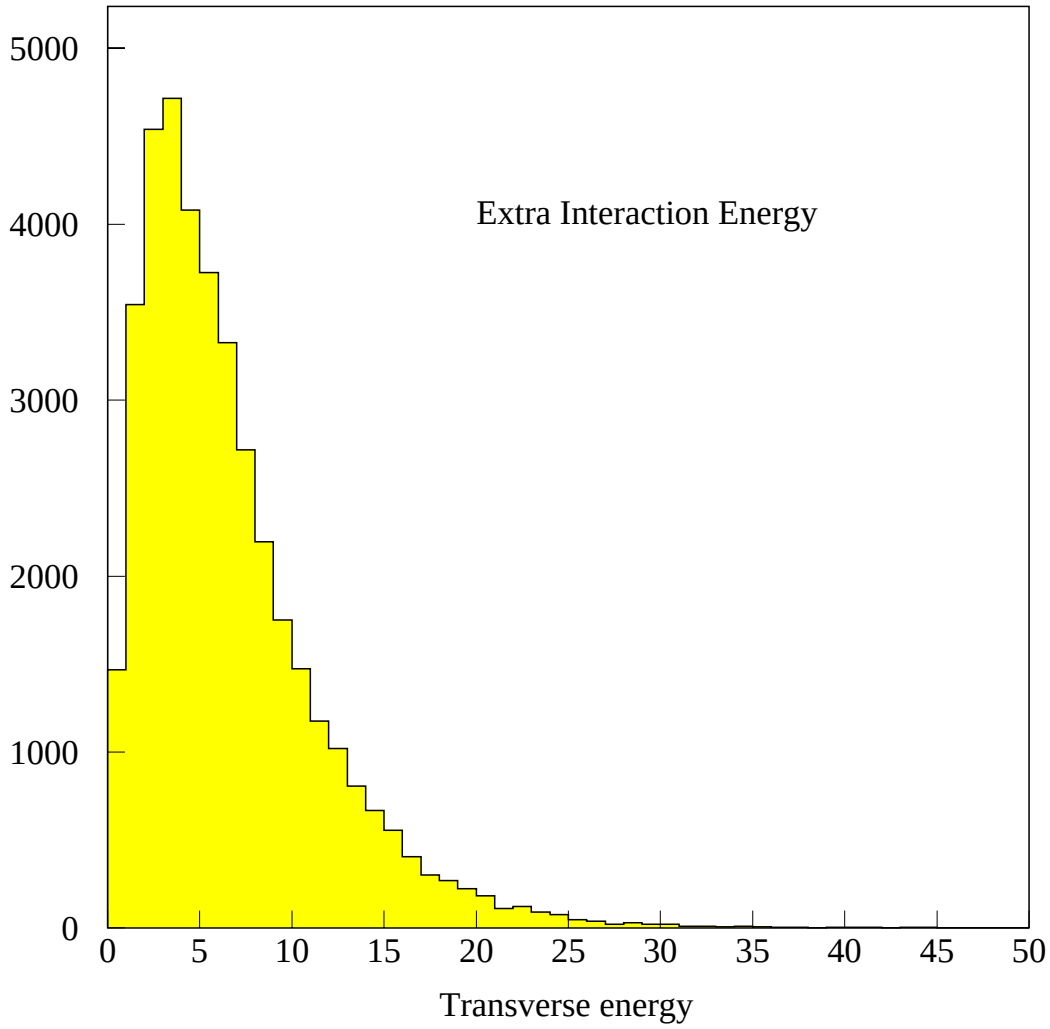

Figure B.5: The magnitude of the energy from interactions which occur in the same crossing as the W + jets event. The distribution was determined with our luminosity-weighted minimum-bias sample.

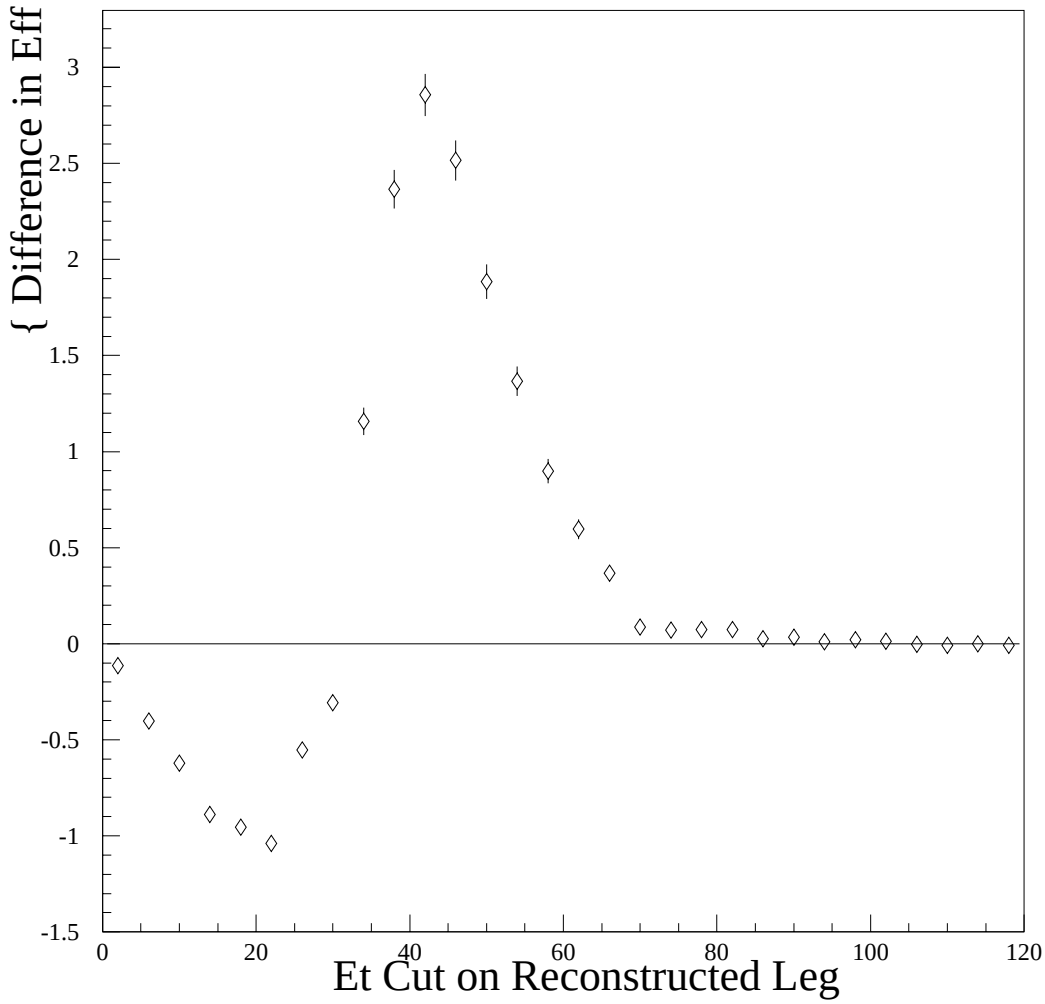

Figure B.6: The percentage change in the fraction of events above a particular transverse energy for the reconstructed Z leg with and without extra-interaction energy. A negative value indicates a loss of efficiency due to the extra energy.

Table B.1: Comparison of acceptances for $W+$ jets events with and without extra interactions.

Sample	No Extra Interactions	Extra Interactions
$W + 0$ jets	0.2347	0.2374
$W + 1$ jets	0.2402	0.2387
$W + 2$ jets	0.2412	0.2391
$W + 3$ jets	0.2737	0.2736
$W + 4$ jets	0.2747	0.2752

Appendix C

The P_{TW} Correction for the 0 Jets Monte Carlo

In order to produce a sample of 0 jet events for the acceptance calculation we use the VECBOS leading order 1 parton Monte Carlo with the parton P_T cut lowered to 1 GeV. It is known that the W boson P_T distribution is not well reproduced by this calculation. The comparison of measured boson P_T between data and fully simulated Monte Carlo is shown in figure C.1. The input P_T distribution must be corrected in order to obtain reliable acceptance numbers.

We used a simple unsmearing procedure on the measured W data P_T distribution in order obtain the input distribution for the Monte Carlo. We generated a grid of input distributions from a 2 parameter function($x^\alpha \cdot \exp(-x/\beta)$). The function was chosen by fitting the original P_T distribution of the Monte Carlo after the initial state radiation had been added to the VECBOS sample. The measured P_T distributions were then obtained by applying a matrix which mapped the true P_T distribution to the measured distribution. The smearing matrix was determined from a detector simulation (QFL) with the addition of the extra-interaction energy as described in appendix B. All W boson efficiencies were included in the smearing matrix. The minimum χ^2 yielded the final input distribution. When this input distribution replaces the Monte Carlo's default distribution we obtain the measured P_T distribution shown at the bottom of figure C.1 which is in much better agreement with the W + 0 jets data shown in the same figure. The correction yielded about a 2% shift in the acceptance calculation.

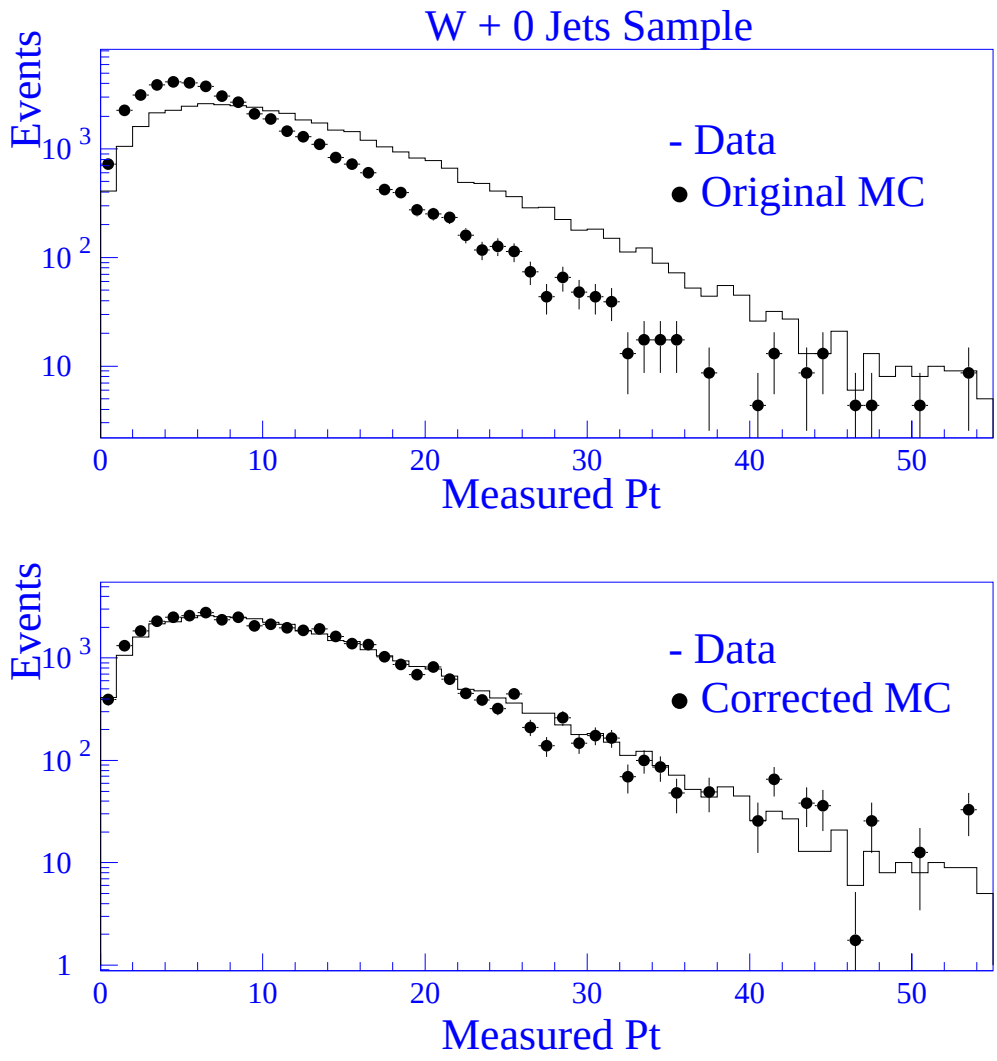

Figure C.1: The W data P_T distribution compared to our Monte Carlo "pseudo-0 jet" sample. The upper plot is the measured distribution (after QFL) for the original Monte Carlo. The lower plot includes a correction to the Monte Carlo after unfolding the data. The data are the same in both.

Appendix D

List of Cross Section Systematics

Our cross section measurements are scaled to a previous CDF inclusive W cross section. We include the systematic errors from this measurement but we must also include sytematic errors which change the ratio of the number of W events with n jets to the total number of W events. These are of course not included in the inclusive W measurement. The list below contains descriptions of those sytematic errors which change the relative cross sections.

Jet E_T Scale: The uncertainty on the jet energy is the single largest contribution to the uncertainty on the cross section measurements. There is a 5% uncertainty on the the jet energy at a jet E_T of 15 GeV. Since the slope of the jet E_T distribution is large at 15 GeV the change in the number of events above 15 GeV after shifting the jets energy by 5% is expected to be large.

To determine the change in the number of events, we vary the jet cone energy by 5% and then apply our standard jet corrections to the new raw jet cone energy. We then simply recount the number of jets above 15 GeV and the number of jets found in each event. This variation translates to about a 10% change in the number of events with ≥ 1 jet and about a 30% change in the number of events with ≥ 4 jets.

Detector η: To reflect the uncertainty due to the use of a detector η cut (≤ 2.4) in defining a jet we vary the jet detector η cut by half the jet cone size ($R/2. = 0.2$).

Underlying Event: The underlying event (UE) variation includes the uncertainty on the UE energy from the primary interaction and the uncertainty on the energy from extra interactions. We vary these corrections simultaneously by $\pm$ 50%.

The value was determined by repeating the study that produced the underlying event and extra interaction corrections. The method employed [21] was the random cone method which randomly checked calorimeter towers of minimum-bias events to see the energy contained in a cone of 0.4. The amount of estimated contamination depends on several parameters used in defining the cone energy such as the allowed η region for the cone and the calorimeter tower energy threshold.

Promotion: A promotion is a jet that is produced from an independent interaction in the same crossing as the W boson event. We measure the probability for promotion from minimum-bias data. We vary the probability by a factor 2.0 for the systematic. This factor was determined by using several independent methods of estimating the the promotion contamination.

QCD background: The systematic error on the QCD background calculations was determined using subsamples of the QCD background sample. The background calculation was tested directly by applying the calculation in subregions of the isolation-$\not\!\!E_t$ plane. In the subregions the observed events are dominated by QCD multijets which can be compared to the predictions given by extrapolation from the low $\not\!\!E_t$ region. We chose a flat variation of 30% on the background normalization which was determined by the ≥ 1 jet background sample. This is a somewhat conservative error estimate since we choose the largest variation to set the error for all jet multiplicities. The background calculation seems more robust at higher jet multiplicities; however, the statistical error also gets considerably large for the test regions so that using a conservative flat error estimate is warranted. A flat systematic will not cancel in the ratio calculation of the cross section because the QCD background fraction increases with the number of jets.

TOP contribution: We use the pythia top 170 sample to calculate our top fraction. The theoretical top cross section at a top mass of 175 GeV/c^2 determines

our baseline top fraction. The top cross section varies from 4.66 to 6.4 pb when the mass is shifted by $\pm$ 6.5 GeV/c^2. We use this variation as our normalization error.

Obliteration: We re-decayed Z's as W's (section 5.3) from our Z data sample to determine the probability of an electron from a $W \rightarrow e\nu$ decay overlapping with a jet in the W event. The analysis was repeated using W Monte Carlo to gain statistical accuracy in the high multiplicity samples and showed good agreement with the Z samples where statistics allowed comparison. The systematic for this calculation was obtained by varying the polarization of the W's and by varying the jet energy cut used to define an obliterated electron.

Acceptance: The kinematic and geometric acceptances were measured from VECBOS Monte Carlo. We changed the renormalization scale of our sample from $Q^2 =< p_t >^2$ to $Q^2 = M_W^2 + p_{tW}^2$ which yielded part of our acceptance systematic. The remaining systematic on the ratio of acceptances is the jet E_T scale uncertainty. The jet E_T scale uncertainty is not only reflected in the number of jets reconstructed but is also propagated into the $\not{E}_t$ calculation. The change in the acceptance due to the jet E_T scale was added in quadrature to the systematic from the renormalization scale.

Appendix E

CDF Author List

F. Abe,[14] H. Akimoto,[32] A. Akopian,[27] M. G. Albrow,[7] S. R. Amendolia,[23] D. Amidei,[17] J. Antos,[29] C. Anway-Wiese,[4] S. Aota,[32] G. Apollinari,[27] T. Asakawa,[32] W. Ashmanskas,[15] M. Atac,[7] F. Azfar,[22] P. Azzi-Bacchetta,[21] N. Bacchetta,[21] W. Badgett,[17] S. Bagdasarov,[27] M. W. Bailey,[19] J. Bao,[35] P. de Barbaro,[26] A. Barbaro-Galtieri,[15] V. E. Barnes,[25] B. A. Barnett,[13] E. Barzi,[8] G. Bauer,[16] T. Baumann,[9] F. Bedeschi,[23] S. Behrends,[3] S. Belforte,[23] G. Bellettini,[23] J. Bellinger,[34] D. Benjamin,[31] J. Benlloch,[16] J. Bensinger,[3] D. Benton,[22] A. Beretvas,[7] J. P. Berge,[7] J. Berryhill,[5] S. Bertolucci,[8] A. Bhatti,[27] K. Biery,[12] M. Binkley,[7] D. Bisello,[21] R. E. Blair,[1] C. Blocker,[3] A. Bodek,[26] W. Bokhari,[16] V. Bolognesi,[7] D. Bortoletto,[25] J. Boudreau,[24] L. Breccia,[2] C. Bromberg,[18] N. Bruner,[19] E. Buckley-Geer,[7] H. S. Budd,[26] K. Burkett,[17] G. Busetto,[21] A. Byon-Wagner,[7] K. L. Byrum,[1] J. Cammerata,[13] C. Campagnari,[7] M. Campbell,[17] A. Caner,[7] W. Carithers,[15] D. Carlsmith,[34] A. Castro,[21] D. Cauz,[23] Y. Cen,[26] F. Cervelli,[23] P. S. Chang,[29] P. T. Chang,[29] H. Y. Chao,[29] J. Chapman,[17] M.-T. Cheng,[29] G. Chiarelli,[23] T. Chikamatsu,[32] C. N. Chiou,[29] L. Christofek,[11] S. Cihangir,[7] A. G. Clark,[23] M. Cobal,[23] M. Contreras,[5] J. Conway,[28] J. Cooper,[7] M. Cordelli,[8] C. Couyoumtzelis,[23] D. Crane,[1] D. Cronin-Hennessy,[6] R. Culbertson,[5] J. D. Cunningham,[3] T. Daniels,[16] F. DeJongh,[7] S. Delchamps,[7]

S. Dell'Agnello,[23] M. Dell'Orso,[23] L. Demortier,[27] B. Denby,[23] M. Deninno,[2] P. F. Derwent,[17] T. Devlin,[28] J. R. Dittmann,[6] S. Donati,[23] J. Done,[30] T. Dorigo,[21] A. Dunn,[17] N. Eddy,[17] K. Einsweiler,[15] J. E. Elias,[7] R. Ely,[15] E. Engels, Jr.,[24] D. Errede,[11] S. Errede,[11] Q. Fan,[26] I. Fiori,[2] B. Flaugher,[7] G. W. Foster,[7] M. Franklin,[9] M. Frautschi,[31] J. Freeman,[7] J. Friedman,[16] H. Frisch,[5] T. A. Fuess,[1] Y. Fukui,[14] S. Funaki,[32] G. Gagliardi,[23] S. Galeotti,[23] M. Gallinaro,[21] M. Garcia-Sciveres,[15] A. F. Garfinkel,[25] C. Gay,[9] S. Geer,[7] D. W. Gerdes,[17] P. Giannetti,[23] N. Giokaris,[27] P. Giromini,[8] L. Gladney,[22] D. Glenzinski,[13] M. Gold,[19] J. Gonzalez,[22] A. Gordon,[9] A. T. Goshaw,[6] K. Goulianos,[27] H. Grassmann,[23] L. Groer,[28] C. Grosso-Pilcher,[5] G. Guillian,[17] R. S. Guo,[29] C. Haber,[15] E. Hafen,[16] S. R. Hahn,[7] R. Hamilton,[9] R. Handler,[34] R. M. Hans,[35] K. Hara,[32] A. D. Hardman,[25] B. Harral,[22] R. M. Harris,[7] S. A. Hauger,[6] J. Hauser,[4] C. Hawk,[28] E. Hayashi,[32] J. Heinrich,[22] K. D. Hoffman,[25] M. Hohlmann,[1,5] C. Holck,[22] R. Hollebeek,[22] L. Holloway,[11] A. Hölscher,[12] S. Hong,[17] G. Houk,[22] P. Hu,[24] B. T. Huffman,[24] R. Hughes,[26] J. Huston,[18] J. Huth,[9] J. Hylen,[7] H. Ikeda,[32] M. Incagli,[23] J. Incandela,[7] G. Introzzi,[23] J. Iwai,[32] Y. Iwata,[10] H. Jensen,[7] U. Joshi,[7] R. W. Kadel,[15] E. Kajfasz,[7a] T. Kamon,[30] T. Kaneko,[32] K. Karr,[33] H. Kasha,[35] Y. Kato,[20] T. A. Keaffaber,[25] L. Keeble,[8] K. Kelley,[16] R. D. Kennedy,[28] R. Kephart,[7] P. Kesten,[15] D. Kestenbaum,[9] R. M. Keup,[11] H. Keutelian,[7] F. Keyvan,[4] B. Kharadia,[11] B. J. Kim,[26] D. H. Kim,[7a] H. S. Kim,[12] S. B. Kim,[17] S. H. Kim,[32] Y. K. Kim,[15] L. Kirsch,[3] P. Koehn,[26] K. Kondo,[32] J. Konigsberg,[9] S. Kopp,[5]

K. Kordas,[12] W. Koska,[7] E. Kovacs,[7a] W. Kowald,[6] M. Krasberg,[17] J. Kroll,[7] M. Kruse,[25] T. Kuwabara,[32] S. E. Kuhlmann,[1] E. Kuns,[28] A. T. Laasanen,[25] N. Labanca,[23] S. Lammel,[7] J. I. Lamoureux,[3] T. LeCompte,[11] S. Leone,[23] J. D. Lewis,[7] P. Limon,[7] M. Lindgren,[4] T. M. Liss,[11] N. Lockyer,[22] O. Long,[22] C. Loomis,[28] M. Loreti,[21] J. Lu,[30] D. Lucchesi,[23] P. Lukens,[7] S. Lusin,[34] J. Lys,[15] K. Maeshima,[7] A. Maghakian,[27] P. Maksimovic,[16] M. Mangano,[23] J. Mansour,[18] M. Mariotti,[21] J. P. Marriner,[7] A. Martin,[11] J. A. J. Matthews,[19] R. Mattingly,[16] P. McIntyre,[30] P. Melese,[27] A. Menzione,[23] E. Meschi,[23] S. Metzler,[22] C. Miao,[17] G. Michail,[9] R. Miller,[18] H. Minato,[32] S. Miscetti,[8] M. Mishina,[14] H. Mitsushio,[32] T. Miyamoto,[32] S. Miyashita,[32] Y. Morita,[14] J. Mueller,[24] A. Mukherjee,[7] T. Muller,[4] P. Murat,[23] H. Nakada,[32] I. Nakano,[32] C. Nelson,[7] D. Neuberger,[4] C. Newman-Holmes,[7] M. Ninomiya,[32] L. Nodulman,[1] S. H. Oh,[6] K. E. Ohl,[35] T. Ohmoto,[10] T. Ohsugi,[10] R. Oishi,[32] M. Okabe,[32] T. Okusawa,[20] R. Oliver,[22] J. Olsen,[34] C. Pagliarone,[2] R. Paoletti,[23] V. Papadimitriou,[31] S. P. Pappas,[35] S. Park,[7] A. Parri,[8] J. Patrick,[7] G. Pauletta,[23] M. Paulini,[15] A. Perazzo,[23] L. Pescara,[21] M. D. Peters,[15] T. J. Phillips,[6] G. Piacentino,[2] M. Pillai,[26] K. T. Pitts,[7] R. Plunkett,[7] L. Pondrom,[34] J. Proudfoot,[1] F. Ptohos,[9] G. Punzi,[23] K. Ragan,[12] A. Ribon,[21] F. Rimondi,[2] L. Ristori,[23] W. J. Robertson,[6] T. Rodrigo,[7a] S. Rolli,[23] J. Romano,[5] L. Rosenson,[16] R. Roser,[11] W. K. Sakumoto,[26] D. Saltzberg,[5] A. Sansoni,[8] L. Santi,[23] H. Sato,[32] V. Scarpine,[30] P. Schlabach,[9] E. E. Schmidt,[7] M. P. Schmidt,[35] A. Scribano,[23] S. Segler,[7] S. Seidel,[19] Y. Seiya,[32] G. Sganos,[12]

A. Sgolacchia,[2] M. D. Shapiro,[15] N. M. Shaw,[25] Q. Shen,[25] P. F. Shepard,[24] M. Shimojima,[32] M. Shochet,[5] J. Siegrist,[15] A. Sill,[31] P. Sinervo,[12] P. Singh,[24] J. Skarha,[13] K. Sliwa,[33] F. D. Snider,[13] T. Song,[17] J. Spalding,[7] P. Sphicas,[16] F. Spinella,[23] M. Spiropulu,[9] L. Spiegel,[7] L. Stanco,[21] J. Steele,[34] A. Stefanini,[23] K. Strahl,[12] J. Strait,[7] R. Ströhmer,[9] D. Stuart,[7] G. Sullivan,[5] A. Soumarokov,[29] K. Sumorok,[16] J. Suzuki,[32] T. Takada,[32] T. Takahashi,[20] T. Takano,[32] K. Takikawa,[32] N. Tamura,[10] F. Tartarelli,[23] W. Taylor,[12] P. K. Teng,[29] Y. Teramoto,[20] S. Tether,[16] D. Theriot,[7] T. L. Thomas,[19] R. Thun,[17] M. Timko,[33] P. Tipton,[26] A. Titov,[27] S. Tkaczyk,[7] D. Toback,[5] K. Tollefson,[26] A. Tollestrup,[7] J. Tonnison,[25] J. F. de Troconiz,[9] S. Truitt,[17] J. Tseng,[13] N. Turini,[23] T. Uchida,[32] N. Uemura,[32] F. Ukegawa,[22] G. Unal,[22] S. C. van den Brink,[24] S. Vejcik, III,[17] G. Velev,[23] R. Vidal,[7] M. Vondracek,[11] D. Vucinic,[16] R. G. Wagner,[1] R. L. Wagner,[7] J. Wahl,[5] C. Wang,[6] C. H. Wang,[29] G. Wang,[23] J. Wang,[5] M. J. Wang,[29] Q. F. Wang,[27] A. Warburton,[12] T. Watts,[28] R. Webb,[30] C. Wei,[6] C. Wendt,[34] H. Wenzel,[15] W. C. Wester, III,[7] A. B. Wicklund,[1] E. Wicklund,[7] R. Wilkinson,[22] H. H. Williams,[22] P. Wilson,[5] B. L. Winer,[26] D. Wolinski,[17] J. Wolinski,[18] X. Wu,[23] J. Wyss,[21] A. Yagil,[7] W. Yao,[15] K. Yasuoka,[32] Y. Ye,[12] G. P. Yeh,[7] P. Yeh,[29] M. Yin,[6] J. Yoh,[7] C. Yosef,[18] T. Yoshida,[20] D. Yovanovitch,[7] I. Yu,[35] L. Yu,[19] J. C. Yun,[7] A. Zanetti,[23] F. Zetti,[23] L. Zhang,[34] W. Zhang,[22] and S. Zucchelli[2]

(CDF Collaboration)

[1] *Argonne National Laboratory, Argonne, Illinois 60439*

[2] *Istituto Nazionale di Fisica Nucleare, University of Bologna, I-40126 Bologna, Italy*

[3] *Brandeis University, Waltham, Massachusetts 02254*

[4] *University of California at Los Angeles, Los Angeles, California 90024*

[5] *University of Chicago, Chicago, Illinois 60637*

[6] *Duke University, Durham, North Carolina 27708*

[7] *Fermi National Accelerator Laboratory, Batavia, Illinois 60510*

[8] *Laboratori Nazionali di Frascati, Istituto Nazionale di Fisica Nucleare, I-00044 Frascati, Italy*

[9] *Harvard University, Cambridge, Massachusetts 02138*

[10] *Hiroshima University, Higashi-Hiroshima 724, Japan*

[11] *University of Illinois, Urbana, Illinois 61801*

[12] *Institute of Particle Physics, McGill University, Montreal H3A 2T8, and University of Toronto, Toronto M5S 1A7, Canada*

[13] *The Johns Hopkins University, Baltimore, Maryland 21218*

[14] *National Laboratory for High Energy Physics (KEK), Tsukuba, Ibaraki 305, Japan*

[15] *Lawrence Berkeley Laboratory, Berkeley, California 94720*

[16] *Massachusetts Institute of Technology, Cambridge, Massachusetts 02139*

[17] *University of Michigan, Ann Arbor, Michigan 48109*

[18] *Michigan State University, East Lansing, Michigan 48824*

[19] *University of New Mexico, Albuquerque, New Mexico 87131*

[20] *Osaka City University, Osaka 588, Japan*

[21] *Universita di Padova, Istituto Nazionale di Fisica Nucleare, Sezione di Padova, I-35131 Padova, Italy*

[22] *University of Pennsylvania, Philadelphia, Pennsylvania 19104*

[23] *Istituto Nazionale di Fisica Nucleare, University and Scuola Normale Superiore of Pisa, I-56100 Pisa, Italy*

[24] *University of Pittsburgh, Pittsburgh, Pennsylvania 15260*

[25] *Purdue University, West Lafayette, Indiana 47907*

[26] *University of Rochester, Rochester, New York 14627*

[27] *Rockefeller University, New York, New York 10021*

[28] *Rutgers University, Piscataway, New Jersey 08854*

[29] *Academia Sinica, Taipei, Taiwan 11529, Republic of China*

[30] *Texas A&M University, College Station, Texas 77843*

[31] *Texas Tech University, Lubbock, Texas 79409*

[32] *University of Tsukuba, Tsukuba, Ibaraki 305, Japan*

[33] *Tufts University, Medford, Massachusetts 02155*

[34] *University of Wisconsin, Madison, Wisconsin 53706*

[35] *Yale University, New Haven, Connecticut 06511*

Bibliography

[1] M.Augilar-Benitez *et al.*, Phys. Rev. D **50**, 1173 (1994).

[2] F. Abe *et al.*, *Observation of Top Quark Production in $\overline{p}p$ Collisions with the Collider Detector at Fermilab*, Phys. Rev. Lett. **74**, 2626 (1995).

[3] F. Abe *et al.*, Private Communication.

[4] L. H. Ryder, *Quantum Field Theory*, seventh ed. (Cambridge University Press, 1985), p. 81.

[5] D. H. Perkins, *Introduction to High Energy Physics*, 3rd ed. (Addison-Wesley, 1987), pp. 185–205.

[6] D. H. Perkins, *Introduction to High Energy Physics*, 3rd ed. (Addison-Wesley, 1987), p. 292.

[7] D. H. Perkins, *Introduction to High Energy Physics*, 3rd ed. (Addison-Wesley, 1987), p. 150.

[8] D. H. Perkins, *Introduction to High Energy Physics*, 3rd ed. (Addison-Wesley, 1987), p. 300.

[9] D. H. Perkins, *Introduction to High Energy Physics*, 3rd ed. (Addison-Wesley, 1987), p. 300.

[10] R. M. Barnett *et al.*, Phys. Rev. D **54**, 94 (1996).

[11] L. H. Ryder, *Quantum Field Theory*, seventh ed. (Cambridge University Press, 1985), p. 290.

[12] UA-1 Collaboration, *Experimental Observation of Isolated Transverse Energy Electrons with Associated Missing Energy at $\sqrt{s} = 540GeV$*, Phys. Lett. **B134**, 469 (1983).

[13] UA-2 Collaboration,*Observation of Single Isolated Electrons of High Transverse Momentum in Events with Missing Transverse Energy at the CERN $\overline{p}p$ Collider*, Phys. Lett. **B126**, 398 (1983).

[14] H. C. Ohanian, *Modern Physics*, 1st ed. (Prentice-Hall, 1987), p. 447.

[15] F. Abe *et al.*, Nucl. Instrum. Methods Phys. Res., Sect. A **74**, 1 (1988), collected articles.

[16] W. Robertson, Private Communication. (1996).

[17] F. Abe *et al.*, *Measurement of* $\sigma B(W \to e\nu\ )$ *and* $\sigma B(Z \to e^+e^-)$ *in* $\overline{p}p$ *Collisions at* $\sqrt{s}$*=1.8 TeV*, Phys. Rev. D **44**, 29 (1991), our selection cuts are the same as those in this reference except for (i) $0.5 < E/p < 2.0$ and (ii) $\chi^2_{strip} < 10$.

[18] F. Abe *et al.*, *Topology of Three-Jet Events in* $\overline{p}p$ *Collisions at* $\sqrt{s}$*=1.8 TeV*, Phys. Rev. D **45**, 1448 (1992).

[19] B. Flaugher, *New Jet Correction Function QDJSCO 2.0*, CDF Pub. **1513**, 1 (1991).

[20] N. Eddy, *New Relative Jet Corrections for Run 1A and Run 1B Data*, CDF Pub. **3534**, 1 (1996).

[21] J. Dittmann, *Studies of Multiple Interactions and Jet Corrections*, CDF Pub. **4001**, 1 (1997).

[22] Weiming Yao and Brenna Flaugher (CDF) derived this correction.

[23] W. Kowald, Private Communication. (1996).

[24] Rob Roser Private Communication.

[25] H.-U. Bengtsson, *Lund Montecarlo for Hadronic Processes-Pythia V 4.8*, CDF Pub. **0676**, (1988).

[26] S. Kopp and G. Sullivan, *Measurement of the Ratio* $\frac{\sigma(W \to e\nu\ )}{\sigma(Z \to e^+e^-)}$, CDF Pub. **1942**, (1992).

[27] C. Loomis, *Using Tauola, a Decay Library for Polarized* τ *Leptons, at CDF*, CDF Pub. **2796**, (1996).

[28] T. J. Phillips, *Correction for X-jets and Photons in* $W \to e\nu$ *and* $Z \to e^+e^- + n$ *Jet Datasets*, CDF Pub. **4084**, 1 (1997).

[29] W. Kowald, Private Communication. (1996).

[30] F.A. Berends, W.T. Giele, H. Kuijf, and B. Tausk, Nucl. Phys. B **357**, 32 (1991).

[31] G. Marchesini and B. Webber, Nucl. Phys. B **310**, 461 (1988).

[32] S. Hauger *et al.*, This Monte Carlo was originally written for the Z + Jets analysis.

[33] F. Abe *et al.*, *Properties of Jets in Z Boson Events from 1.8 TeV $\overline{p}p$ Collisions*, Phys. Rev. Lett. **77**, 448 (1996).

[34] B. Badgett and P. Derwent, *Event Z Vertex Cut Efficiency as a Luminosity Correction for Run 1A*, CDF Pub. **2703**, (1994).

[35] F. Abe *et al.*, *Measurement of $\sigma B(W \to e\nu)$ and $\sigma B(Z \to e^+e^-)$ in $\overline{p}p$ Collisions at $\sqrt{s}$=1.8 TeV*, Phys. Rev. Lett. **76**, 3070 (1996).

[36] F. Abe *et al.*, *Measurement of the ratio $\sigma B(W \to e\nu)/\sigma B(Z^0 \to e^+e^-)$ in $\overline{p}p$ collisions at $\sqrt{s} = 1.8$ TeV*, Phys. Rev. Lett. **73**, 220 (1994).

[37] F. Abe *et al.*, A Measurement of Jet Multiplicity in W Events in $\overline{p}p$ Collisions at $\sqrt{s} = 1800$ GeV, Phys. Rev. Lett. **70**, 4042 (1993).

[38] F. Abe *et al.*, W boson + Jet Angular Distribution in $\overline{p}p$ collisions at $\sqrt{s} = 1.8$ TeV, Phys. Rev. Lett. **73**, 2296 (1994).

[39] F. Abe *et al.*, Measurement of the W Boson Mass Phys. Rev. D **52**, 4784 (1995).

[40] K. Einsweiler, *The NNLO W and Z Cross Sections and Their Uncertainties*, CDF Pub. **3581**, 10 (1996).

[41] T. M. Joffe-Minor,*A Measurement of the Ratio of Production Cross Sections for W+ 1 Jet to W+ 0 Jet* , Thesis, (1997).

[42] S. Eno, *Lepton Removal for M_W Analysis*, CDF Pub. **2063**, (1993).

Biography

Daniel Patrick Cronin-Hennessy was born in Peoria, Illinois on May 12, 1966. He was raised in Louisville, Kentucky where he attended Our Mother of Sorrows elementary school. He graduated from high school at Adair County High in Columbia, Kentucky.

Daniel majored in physics at Boston College and received his Bachelor of Science degree in 1990. He began graduate school at Duke University where received a masters in 1993. He earned his PhD. in physics in 1997 at the age of 31.

Daniel is currently a member of the American Physical Society and the Duke Chapter of Sigma Xi. He lives happily with his wife Lisa in Durham, North Carolina and works at Duke University as a Post Doctorate Researcher.

Among his refereed publications are two papers which describe analyses of the hadronic production characteristics of W and Z bosons.